POLITECNICO DI MILANO
DEPARTMENT OF PHYSICS
DOCTORAL PROGRAMME IN PHYSICS

MICROMAGNETIC DEVICES FOR SINGLE-CELL MECHANOBIOLOGY

Doctoral Dissertation of:
MARCO MONTICELLI

Supervisor:
Prof. Riccardo Bertacco

Tutor:
Prof. Giacomo Claudio Ghiringhelli

The Chair of the Doctoral Program:
Prof.ssa Paola Taroni

June 2017 - XXIX cycle

Abstract

The emerging field of *mechanobiology* aims at investigating how cells sense and respond to extracellular or intracellular mechanical signals, highlighting the biophysical mechanisms which connect mechanical stimuli and fundamental cell functions. In this context, methods for the application of controlled and localized forces to single cells are required to properly mimic the behavior of the extracellular microenvironment. However, current techniques for mechanobiology studies still have several limitations, not properly allowing to apply localized, inhomogeneous and prolonged forces.
This thesis work deals with the development of two innovative micromagnetic devices for studies in mechanobiology.

The first tool, based on magnetic domain wall tweezers (DWTs), is suitable for the application of finely controlled and localized forces on target cells. Domain walls propagating in microfabricated ferromagnetic rings, acting as movable attracting poles, are exploited to trap and handle superparamagnetic beads in a cell culture environment. The device is tested with 1μm particles which are manipulated against the membrane of HeLa cells cultured on-chip, thus exerting highly localized forces. Local deformations of the cell membrane are observed and measured via confocal microscopy. Forces producing cell indentations are in the order of hundreds of pN, in good agreement with the prediction of an elastic model of the cell membrane. Noteworthy, an accurate quantification of forces is carried out via micromagnetic simulations, monitoring the particle position with respect to the attracting poles, which acts as a "calibrated spring".
In addition, it is shown that this technique allows for the manipulation of magnetic nanoparticles microinjected inside the HeLa cell cytoplasm, paving

the way to the application of mechanical stimuli to the nucleus and cellular subcompartments. To summarize, this work demonstrates that DWTs represents a versatile and non-invasive on-chip technology for mechanobiology studies on single cells, where the application of localized forces is required. Crucial for applications in biology, it is fully compatible with real-time optical monitoring of the cell activity upon quantitative and localized mechanical stimulation.

The second device developed in this thesis, is based on Fe-coated PDMS micropillars, which exert a periodic mechanical pinching on different points of the cell membrane, with a highly controllable intensity and time evolution. The application of uniform magnetic fields allows for the platform actuation, producing a controlled bending of the pillars and thus exposing the cells to mechanical stimuli. Due to the peculiar geometry of groups of magnetic pillars, when a rotating magnetic field is applied, each cell experiments a localized and biaxial periodic pinching. The time behavior of such stimuli is controlled by the field rotation, allowing for a tunable pinching frequency.
The applied forces, evaluated by micromagnetic simulations, are in the order of tens of nN and can be finely modulated by tuning the external field.
To assess the potential of this technique, it has been applied to the study of the mechanical and dynamic response of the cellular nucleus to the local pinching. In particular, it has been demonstrated how the application of forces on the cell at a pinching frequency of 0.1 Hz affects the nuclear morphology, deformability and H2B core histone turnover on chromatin. The extrapolation of the typical nuclear response time to the mechanical stimuli shows that, at the selected pinching frequency, nucleus-pillars coupling is not purely elastic but mediated by active cellular mechanisms. Indeed, an enhancement in actin dynamics during stimulation is observed, demonstrating that it plays a role in pillars-induced force transmission. Finally, translocation of MKL transcription cofactor from the nucleus to the cytoplasm is observed during stimulation, suggesting that local pinching affects genomic functions.

Preface

The present thesis reports most of the work carried out by the author, Marco Monticelli, from the beginning of his Ph.D. studies on May 1st, 2014. The principal supervisor has been Prof. R. Bertacco from "Politecnico di Milano" and the experimental activity was performed in four research centers:

- PoliFAB, Politecnico di Milano, Milan, Italy.
- Laboratory for Epitaxial Nanostructures on Silicon and for Spintronics (LNESS), Politecnico di Milano, Como, Italy.
- Istituto FIRC di Oncologia Molecolare (IFOM), Milan, Italy.
- Mechanobiology Institute (MBI), National University of Singapre, Singapre.

This Ph.D. work has resulted in the following publications and contributions.

Journal Papers

1. **M. Monticelli**, E. Albisetti, D. Petti, D. Conca, M. Falcone, P. Sharma and R. Bertacco "Towards an on-chip platform for controlled forces application via magnetic particles: a novel device for mechanobiology", *Journal of Applied Physics*, 2015, 117, 17B317.
2. R. Castagna, A. Bertucci, E. Prasetyanto, **M. Monticelli**, D. Conca, M. Massetti, P. Sharma, F. Damin, M. Chiari, L. De Cola, and R. Bertacco, "Reactive Microcontact Printing of DNA Probes on (DMA-NAS-MAPS) Copolymer-Coated Substrates for Efficient Hybridization Platform", *Langumir*, 2016, 32, 13, pp 3308-3313.

3. **M. Monticelli**, A. Torti, M. Cantoni, D. Petti, E. Albisetti, A. Manzin, E. Guerriero, R. Sordan, G. Gervasoni, M. Carminati, G. Ferrari, M. Sampietro and R. Bertacco, "On-Chip Magnetic Platform for Single-Particle Manipulation with Integrated Electrical Feedback", *Small*, 2016, 12, 7, pp 921-9.

4. P.P. Sharma, E. Albisetti, **M. Monticelli**, R. Bertacco and D. Petti, "Exchange Bias Tuning for Magnetoresistive Sensors by Inclusion of Non-Magnetic Impurities", *Sensors*, 2016,16, 7, p 1030.

5. **M. Monticelli**, D.V. Conca, E. Albisetti, A. Torti, P.P. Sharma, G. Kidiyoor, S. Barozzi, D. Parazzoli, P. Ciarletta, M. Lupi, D. Petti and R. Bertacco, "Magnetic domain wall tweezers: a new tool for mechanobiology studies on individual target cells", *Lab on a chip*, 2016, 7, 16, pp 2882-90.

6. P.P Sharma, E. Albisetti, M. Massetti, M. Scolari, C. La Torre, **M. Monticelli** et al, "Integrated platform for detecting pathogenic DNA via magnetic tunneling junction-based biosensors", *Sensors and Actuators B: Chemical*, 2017, 242, pp 280-287.

7. P.P. Sharma, G. Gervasoni, E. Albisetti, F. D'Ercoli, **M. Monticelli**, D. Moretti, N. Forte, A. Rocchi, G. Ferrari, P. Baldelli, M. Sampietro, F. Benfenati, R. Bertacco and D. Petti, "Towards a magnetoresistive platform for neural signal recording", 2017, doi: 10.1063/1.4973947.

Conference Proceedings

1. M. Carminati, G. Ferrari, S. Kwon, **M. Monticelli**, A. Torti, D. Petti, E. Albisetti, M. Cantoni, R. Bertacco and M. Sampietro, "Towards the Impedimetric Tracking of Single Magnetically Trailed Microparticles", *Proceeding IEEE 11th Multi-Conference on Systems, Signals & Devices*, 2014.

2. **M. Monticelli**, D. Petti, E. Albisetti, M. Cantoni, E. Guerriero, R. Sordan, M. Carminati, G. Ferrari, M. Sampietro and R. Bertacco, "Closed loop microfluidic platform based on domain wall magnetic conduits: a novel tool for biology and medicine", *Proceeding MRS*, 2014.

Conference Contributions

1. Talk "On-chip magnetic platform for single particle delivery and particle transit monitoring" at Intermag 2014, Dresden, Germany.

2. Talk "On-chip investigation of cellular functions via magnetic nanoparticles: a novel tool in mechanobiology" at EMRS-fall 2014, Varsaw, Poland.

3. Poster "On-chip platform for investigating cellular functions via magnetic particle" at Magnet conference 2015, Bologna, Italy.

4. Talk "Mechanobiology studies and investigation of cellular functions via magnetic particles and microfluidic channels" at FisMat 2015, Palermo, Italy.

5. Talk "On-chip application of localized forces on target cells via magnetic particles for mechanobiology studies" at AIM 2016, Bormio, Italy.

6. Talk "Magnetically actuated micropillars for mechanobiology studies" at Intermag 2017, Dublin, Ireland.

Marco Monticelli
PoliFAB - Department of Physics
Politecnico di Milano
June 2017

Contents

List of Figures

List of Tables

Chapter 1

Introduction

This experimental Ph.D. thesis deals with the development of innovative micromagnetic devices for studies on single cells. The purpose of this chapter is to introduce the framework in which they operate, i.e. the *mechanobiology*. Besides, the motivations behind the development of miniaturized technologies for single cell investigation and the relative state of the art are presented. Finally, the organization of this thesis for a better comprehension of the following chapters is described.

1.1 Mechanobiology

Mechanobiology is an emerging field which connects biology, physics and engineering to explore how mechanical stimuli or alterations in the mechanical properties of cells affect biological processes, such as cellular differentiation[1], migration[2], proliferation[3] or changes in gene expression[4].
The role played by mechanical stresses in tissues development has been known for more than a century. In 1892, Julius Wolff described bone remodeling, studying its shape, density and stiffness upon the application of a continuous mechanical load[5]. However, only in the last two decades mechanobiology has gained a central importance in the comprehension of *mechanotransduction* mechanisms, i.e. the molecular processes involved when cells sense and respond to mechanical stimuli[6].
Some reasons can be identified for explaining the late development of this

field. First, most of the biological studies which aimed to investigate the cell interaction with its environment were focused on cell responses to extracellular bio-chemical signals. For example, the intracellular biopathways activated when growth factors, hormones or cytokines bind receptor molecules on cell membrane are well established[7],[8],[9]. Instead, the effects of extracellular mechanical signals, such as shear or normal forces and stresses induced by substrates with different rigidity and geometry, are still partially unknown[10],[11].

In addition, innovative technologies are required to apply localized stimuli at the cellular or subcellular level and to precisely detect small bio-physical signals. For this reason, only recent advances in the development of miniaturized techniques[12],[13], have provided biologists with effective tools for such analysis.

Besides, a growing interest in the field has been brought by studies on infected and cancerous cells whose mechanical properties have revealed dramatic modifications compared to healthy cells[14]. For example, red bloods infected by Malaria parasite become stiffer and more cytoadherent[15],[16], while the stiffness of metastatic cells significantly decrease (until 70%), compared to benign ones[17].

To highlight the importance of extracellular mechanical signals on cells development and behavior, we consider the way Mesenchymal stem cells (MSCs) differentiate, adapting to different substrates or to external forces. MSCs cultured on soft substrates become neurogenic (like neural cells), on rigid substrates are osteogenic (like bone cells) and on substrate with intermediate stiffness myogenic (like muscle cell)[18]. Moreover, MSCs cultured on elongated micropatterns become osteogenic, while those cultured on squares are adipogenic (like fat cells)[19]. MSCs exposed to fluid shear stress also exhibit osteoblastic phenotype[20]. Another relevant effect is the mechanically induced alteration of gene expression. Jain et al.[4] have shown that fibroblasts cultured on fibronectin micropatterns with elongated geometry (1800 μm^2 1:5 rectangle) exhibit upregulation of genes associated to cell migration, cellular adhesion and actin cytoskeleton, while fibroblasts on constrained isotropic patterns (500 μm^2 circle) show an upregulation of genes connected to cell division and negative regulation of cell-matrix adhesion.

These two examples clearly show how the behavior of cells is strictly connected to the physical interaction with the surrounding environment.

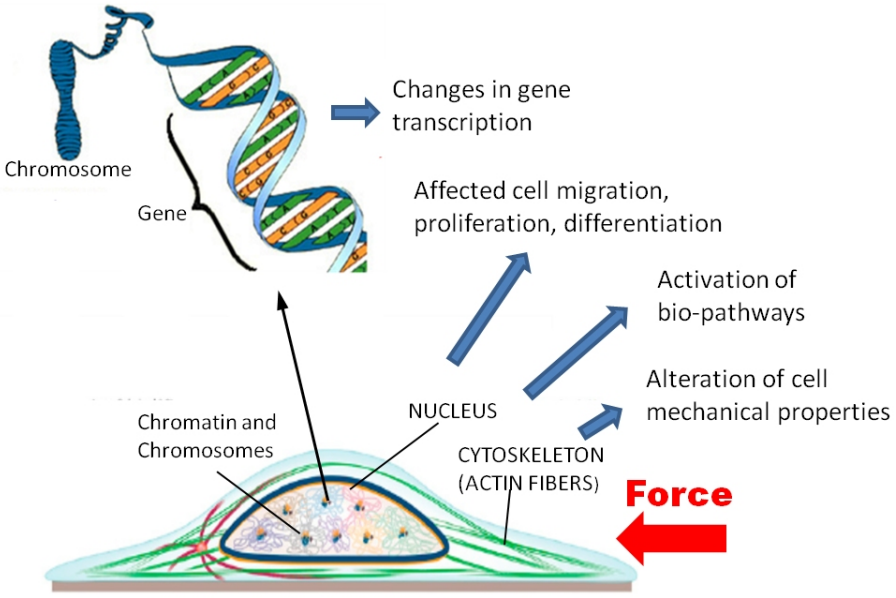

Figure 1.1: Sketch of the cellular responses induced by a mechanical stimulus applied on the cell membrane. Adapted from[21].

The application of forces induce several cell responses (see Fig.1.1): alteration of cell morphology and mechanical properties, activation of signaling pathways and consequent functional responses (e.g. migration, differentiation and gene trasncription).
Several studies have reported that physical properties of cells such as morphology, strength of focal adhesions, cytoskeletal organization and nuclear shape are affected by the exposure to mechanical stress. As an example, the shape of endothelial cells changes from polygonal to ellipsoidal upon the application of mechanical stimuli, orienting themselves along the force direction[20]. Moreover, in response to shear stress, human endothelial cells exhibit long actin stress fibers[11]. Futhermore, cells become more elongated increasing the substrate rigidity[22],[23] and finally the nuclear morphology adapts to the cell shape, becoming more rounded on soft substrates and more flattened on rigid ones[4].

Together with these changes in the physical properties of cells, various signaling pathways are sensitive to mechanical stimuli. For example *Armadillo*, which is a transcription coactivator, shuttles to the nucleus in drosophila embryos upon application of unilateral compression[24] and nuclear accumulation of cofactor Megakaryoblastic Leukemia Factor (MKL) is enhanced in cells with stretched shapes[25] and upon application of forces[26]. Another relevant example is represented by the cofactors YAP/TAZ, whose activity and nuclear translocation are affected by the cytoskeletal tension[27] and, thus, influenced by the mechanical signals that cells receive from the cellular environment[28]. YAP and TAZ have recently attracted a growing interest in the field, due to their overarching functions as mechanotransducers and mechanosensors[29].
The physical and chemical cellular responses to mechanical stimuli may not be mutually exclusive. This is confirmed by studies on nuclear translocation of various transcription factors, which are affected by the interaction with focal adhesions and cytoskeleton. As an example, MKL translocation is related to the state of actin polymerization; it binds to *G-actin* in the cytoplasm and only when mechanical stimuli induce actin polymerization, MKL shuttles to the nucleus[26].
Starting from this general overview on the physical and chemical alterations that occur in response to mechanical stimuli, we focus on mechanotransduction mechanisms involved when forces are transmitted from the plasma membrane to the nucleus. In the following section, a brief presentation of the state of the art in this sub-field is provided. It will be useful for better understanding the biological framework where the techniques developed in this thesis operate.

1.1.1 Cell-nucleus mechanics and mechanotransduction

The nucleus and chromatin, where the DNA is located, are physically coupled to the cell periphery via cytoskeleton, which determines the cell structure. Cytoskeleton is primarily composed by proteins such as actin, microtubules and intermediate filaments (see Fig.1.2). Actin, together with myosin and other cross-linking proteins, forms tensile filaments that originate at the focal

adhesions and are involved in force transmission to the nucleus[30]. Instead, microtubules are structured as tubular polymers and form networks around the nucleus[31]. Intermediate filaments protein, such as Vimentin, also play a relevant role in the transmission of forces[32]. These cytoskeletal components are physically connected to the cellular nucleus through trans membrane proteins (such as nesprin-1,-2,-3.-4) located on the outer nuclear membrane. Besides, these proteins interact with the inner nuclear membrane, to transfer the mechanical signals inside the nucleus[33],[34].
Mechanical stimuli arising from the extracellular matrix can propagate as stress waves through this physical link from focal adhesions to the nucleus[35]. Additionally, active forces from the cytoskeleton preserve the nuclear prestress, thus determining its morphology.
Perturbations of this physical cytoskeletal-link components alter propagation of mechanical signals and affects either the shape of the nucleus and functional responses, such as differentiation and transcription. For example, actin perturbation (by cytochalasin-D) and inhibition of myosin (by blebbistatin) results in decreased nuclear projected area. Instead, microtubules inhibition induces an increase of the nuclear area, suggesting that, whereas actomyosin fibers apply tensile load, microtubules exert a compressive stimulus on the nucleus[35][21]. Myosin inhibition also removes the nuclear shape modulation by substrate rigidity[31]. Finally, "knockdown" of nesprin-3, which is a linker between intermediate filaments and the nucleus, affects mechanotransduction in human endothelial cells[36].
In addition to the cytoskeletal-link (between focal adhesions and cellular nucleus), a physical link from nuclear membrane to the chromatin also exists. Several proteins, such as lamins and emerin, play a relevant role in this connection[37]. As an example, some studies have shown that proteins on the inner nuclear membrane, e.g. Lamin-B and Lamin-A/C, connect chromatin to nuclear periphery via interaction with Heterochromatin Protein-1 [38].
The aforementioned links allow the transmission of physical signals from cell periphery to chromatin, thereby providing permissivity to alter chromatin functions and structure in response to mechanical stimuli.
For example, subnuclear structures in endothelial, osteosarcoma and HeLa cells show dynamics that scales with the amplitude of the applied shear

stress[39]. Mechanical stimulation of cells via magnetic beads bound to plasma membrane, results in chromatin remodeling[25].

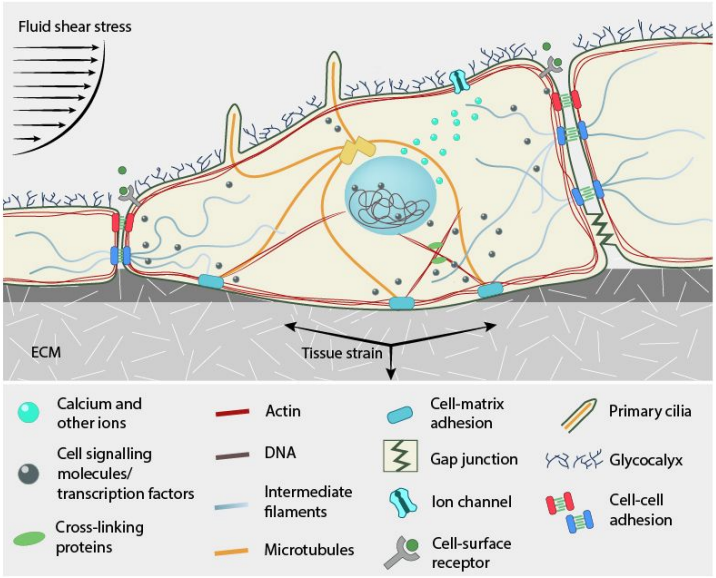

Figure 1.2: Sketch of the mechanotransduction links and cell components allowing the transmission of mechanical stimuli (e.g. fluid shear stress or tissue strain) from the focal adhesions to the nucleus. Adapted from[40].

Moreover, the perturbation of physical links from focal adhesions to the chromatin affects the dynamics of various chromatin binding proteins. For example, some studies reveal an enhancement of core histones (proteins in the chromatin) dynamics in embryonic stem cells compared to primary fibroblasts; this can be due to the weak physical links between cell periphery and chromatin in stem cells[41]. Finally, perturbation of focal adhesion proteins (e.g. actin) also results in enhanced dynamics of core histones[21].
Such aforementioned alterations in the dynamics of chromatin and histones are associated to nucleus structural changes required for regulating gene expression in response to mechanical stimuli.
Despite all these studies have highlighted some of the fundamental cell components and mechanisms involved in mechanotransuction, a full comprehension is still missing. In particular, the aforementioned studies provide a limited knowledge of the time evolution of such cell dynamics which are also

strongly affected by the way in which forces are applied on cells. Moreover, most of the exerted mechanical stimuli are uniform and constant, not properly reproducing the dynamic environment of the extracellular matrix, where cells are continuously exposed to forces variable in time and applied on several points of the cell membrane.
This is essentially limited by the techniques used to produce such stimuli, because tools for properly mimicking the active forces exerted by the cell environment are still at their infancy. In particular, there is a growing need for methods allowing for the application of forces quantitatively tunable in strength, direction and temporal behavior, as well as compatible with sophisticated optical techniques for biological investigation.
To better understand the technological framework where the devices developed in thesis work are inserted, the state of the art concerning the techniques used for mechanobiology studies on single cells is presented.

1.2 Technologies for mechanobiology studies

To apply mechanical stimuli at cellular and subcellular level, different techniques have been recently developed[12]. They can be divided in two main categories: passive and active methods.
The first group includes all the devices that can not be actuated. Cells are thus exposed to predefined and uniform mechanical stimuli, due to the geometry and rigidity of the substrates where they are cultured. Mechanobiology studies exploiting these techniques rely on the comparison of cell responses on substrates with different properties.
Instead, active technologies allow to apply external forces on cells, to investigate cell dynamics in response to such stimuli.
The first category include a variety of functional materials such as PDMS[42] or gels[43], properly micro- and nanostructured. A relevant example is provided by arrays of microposts[44],[45] where cells experiment constant elastic forces due to the pillars bending (see Fig.1.3a). Another strategy is represented by substrates where adhesion molecules (e.g. fribonectin) are micropatterned[46],[4], allowing to trigger the shape of cells and nuclei. Finally, polymeric microchannels with geometrical constrictions are used to in-

vestigate cellular and nuclear plasticity, as well as functional responses such as migration[47].
Although the aforementioned techniques are well established, the impossibility to control the applied forces in time, space and strength is a major limitation.
Concerning the active methods, a relevant example is provided by microfluidic devices that allow to apply fluid shear stress on cells, controlling the flux inside microchannels[48],[39]. Micromechanical stretching devices, e.g. microelectromechanical systems (MEMS)[49],[50], whose typical feature size matches the micrometrical dimensions of cells are also used.
A different approach is offered by atomic force microscopy (AFM)[51],[52] (*see* Fg.1.3b) and patch-clamp[53] (see Fig.1.3c) based technologies, which exploit nanometric and micrometric tips to exert controlled forces. Both allow the application of localized mechanical stimulation; however some drawbacks can be identified: patch clamps are invasive, as they may easily damage cells, while AFM systems cannot be easily integrated with high resolution microscopes for fluorescence-based biological analysis. Moreover, these techniques do not allow to easily implement more than one experiment at a time.
Another strategy is offered by micromanipulation techniques[54] based on the controlled and localized motion of micro and nanoparticles. They are becoming a fundamental tool for testing the mechanical properties of cells and nuclei[55]. Among these micromanipulation techniques, optical tweezers (see Fig.1.3d) represent a well established technology. The first demonstration of trapping and manipulation of microparticles, viruses and bacteria via optical tweezers was provided by Ashkin and coworkers in 1986 [56]. Despite this technology presents good versatility and spatial resolution, some drawbacks can be identified. Among these are, first of all, the damage to the biological entities due to laser-induced heating[58],[59] and, secondly, the inherent complexity and cost of the optical setup. In the past years, alternative methods have been developed to overcome these limitations. Electrophoresis[60] and dielectrophoresis[61] based techniques are widely used, but they are strictly dependent on particle polarizability and medium conductivity. Furthermore, they utilize electrical forces that may adversely affect cell viability due to current-induced heating and/or direct electric field interaction. In the same

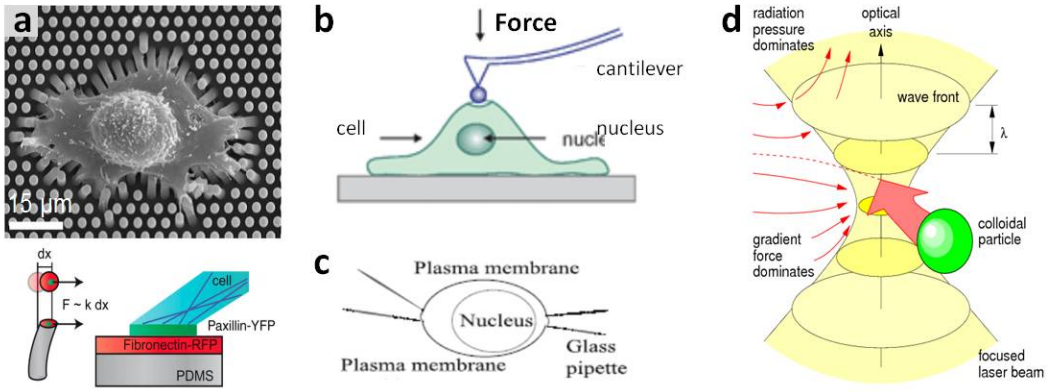

Figure 1.3: Overview of the miniaturized technologies for mechanobiology studies. **a** Micropatterned substrate in Polydimethylsiloxane (PDMS), adapted from[57]. **b** Atomic force microscopy based technique, adapted from[51]. **c** Cell stimulation by patch-clamp, from[53]. **d** Optical tweezers for dielectric particles manipulation, adapted from[56].

way, acoustic-based tweezers[62] induce unintentional heating due to power density requirements.
In this context, the use of *magnetic* technologies is very appealing because low frequency magnetic fields do not affect the cellular response, allowing to develop biocompatible devices. In the next section, a focus on magnetic techniques for mechanobiology studies is presented.

1.2.1 Magnetic techniques

Combining magnetic fields or field gradients with magnetic particles is possible to manipulate the latter to exert local stimuli on cells. These micromanipulators, called magnetic tweezers, have been widely used in mechanobiology[63]. The magnetic particles exploited for such studies are typically superparamagnetic beads with high saturation magnetization (see section 2.3). The intensity of the applied forces depends both on the beads size, geometry and composition, together with the magnetic field gradients intensity. As a matter of fact, to apply relevant forces on cells (at least tens pN[12]), the field gradient should not be lower than few mT/μm, on conventionally used 1 μm

particles with magnetic susceptibility ≈1. Moreover, such field has to be very confined coherently with the micro- or nanometric size of the particles to be manipulated. Different strategies can be adopted to achieve such requirements.

One possible approach is based on the use of micrometric tip electromagnets (see Fig.1.4a). This technique allows for the application of intense, tunable and localized forces on the cell membrane[55] or inside the cytoplasm[25]. However, some drawbacks can be identified. First, these magnetic tweezers allow to apply attractive forces only on particles previously bound to the plasma membrane or located inside the cell, without a real control on particles position. In addition, only few particles at a time can be manipulated preventing throughput in the analysis.

Another strategy relies on *on-chip* technologies, properly micro- or nanofabricated to produce confined and intense magnetic fields for particles manipulation[64] (see Chapter 4.1). Gunnarsson et al.[65] first proposed to combine uniform magnetic fields with ferromagnetic elements patterned on-chip (see Fig.1.4b), whose magnetization creates a confined stray field, employed to trap and manipulate particles with a micrometric resolution.

In this context, a magnetic handling technology called "Domain Wall Tweezers" (DWTs) has been proposed[66],[67],[68]. It is based on the displacement of magnetic domain walls (DWs) in ferromagnetic conduits (see Fig.1.4c), allowing the manipulation of magnetic micro and nanoparticles with resolution down to hundreds nm[69].

In this thesis work, the development of a device based on DWTs for mechanobiology studies is presented. It allows to trap and manipulate beads in a biological environment and inside the cell cytoplasm, exerting precisely localized forces up to several hundreds pN.

Furthermore, the use of magnetism to develop polymeric devices that can be actuated to apply stimuli on cells, has also attracted interest in the scientific community. This approach combine passive devices (e.g. substrates with a certain rigidity and geometry) with an active magnetic functionality, modulated by external magnetic fields. Magnetically actuated polymeric platforms are proposed as a method to stretch or compress tissues[70],[12] applying poorly localized but intense forces. However, the development of

similar devices on a scale of few micrometers for single cell mechanobiology studies is still a major issue.

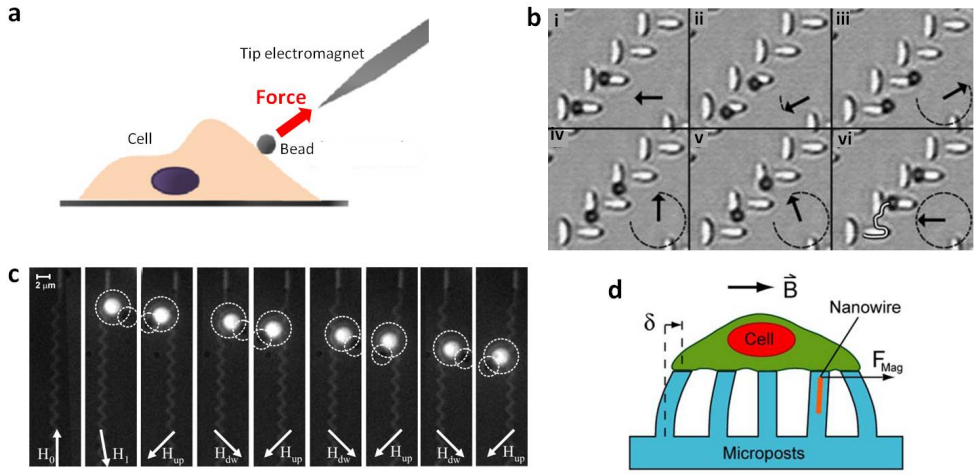

Figure 1.4: Magnetic technologies for mechanobiology studies. **a** Sketch of magnetic tweezers to exert forces on particles bound to the cell membrane. **b** Magnetic beads (2.8 μm) manipulated on a staircase pattern of Permalloy ellipses by the application of a rotating magnetic field (8 mT). The black arrow indicates the field direction in each frame. After a complete field revolution, beads are moved by one step in the pattern, as indicated by the white curve in (vi). Adapted from[65]. **c** Manipulation of a pair of magnetic beads by Domain wall tweezers on zig-zag shaped conduits. The fluorescent bead (2.8 μm diameter) is bound by chemical affinity between proteins, with a second bead (1 μm diameter). Adapted from[69]. **d** Magnetic micropost with a *Co* nanowire embedded in the polymeric pillars. The application of a magnetic force allow to stimulate cells on top. Adapted from[71].

Recently, some groups have developed technologies which are based on magnetic pillars, embedding magnetic particles inside a micropatterned polymeric substrate[72],[73]. In these works, the external field is provided by a tip electromagnet, allowing to actuate few pillars at a time with a reduced control on the pillars bending. In 2007 N. J. Sniadecki et al.[71] (see Fig.1.4d) have shown how magnetic microposts can be used to investigate certain cell behaviors. This technique relies on magnetic nanorods embedded in a soft-

substrate, actuated by a uniform magnetic field. However, the use of such device for sophisticated mechanobiological studies is limited, as it is affected by a low control on magnetic nanorods position inside the polymeric matrix, not allowing a precise modulation of the stimulus. Moreover, the mechanical stimulation is typically applied to a single point of the cell membrane. For these reasons, magnetic micropillars are still not widely used in mechanobiology. In this thesis work, a micromagnetic device based on magnetic pillars that overcome the aforementioned limitations is presented. It is a novel technology based on Fe-coated PDMS (Polydimethylsiloxane) micropillars properly patterned to exert compressive and tensile forces on different points of the cell membrane, mimicking those arising from the extracellular matrix. These magnetic pillars produce mechanical pinching on the cell membrane with forces in the order of tens nN that can be precisely tuned and controlled in time, upon the application of a uniform magnetic field.

1.3 Summary and outlook of the thesis

This thesis work is inserted in the scientific framework described in the previous sections and deals with the development of two innovative micromagnetic devices for mechanobiology: magnetic domain wall tweezers (DWTs) and magnetically actuated micropillars. The first one (see Chapter 4) is based on magnetic domain wall manipulators[66],[67], introduced in the previous section. It allows to finely manipulate magnetic particles in a biological environment and to exert localized and controlled forces on target cells (see Fig.1.5a). This technique has been tested studying the cell membrane deformation induced in a HeLa cell cultured on-chip. Besides, the possibility to manipulate microinjected nanoparticles inside the cell cytoplasm is demonstrated, paving the way to the applications of mechanical stimuli at a subcellular level (e.g. on the cell nucleus).
The second device is a novel technology, based on Fe-coated PDMS micropillars. They are magnetically actuated to exert controlled forces on cells cultured on top. The application of uniform magnetic fields produces a controlled bending of the pillars (see Fig.1.5b), exposing the cells to mechanical stimuli. Due to the peculiar geometry of these magnetic pillars (see Chapter 5

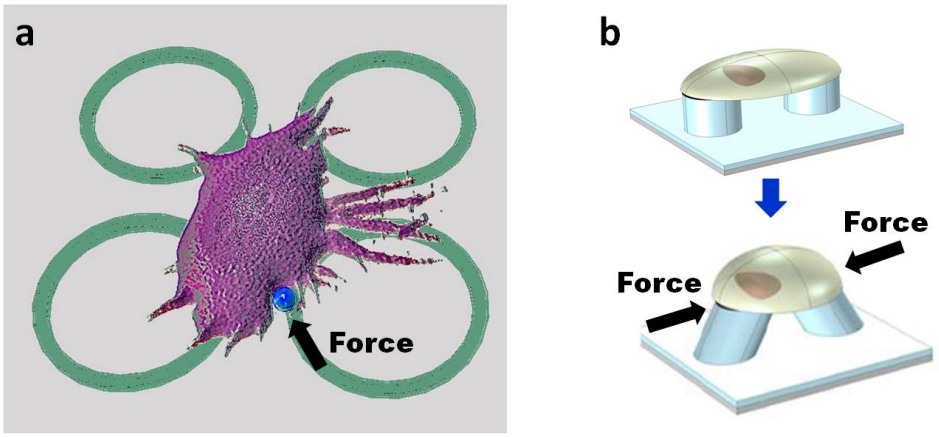

Figure 1.5: Sketch of the basic idea of the devices developed in this thesis work: magnetic domain wall tweezers (**a**) and magnetic micropillars (**b**).

for details), each cell can be continuously mechanically pinched in different points of the membrane when a rotating magnetic field is applied. It allows to produce a mechanical stimulation that mimic the one exerted by the extracellular matrix. Moreover, a fine tuning of the applied force and pinching frequency is achieved. This technology has been fully validated for sophisticated biological studies and used to investigate the cell nucleus dynamics.

The work presented here, started as a continuation of my Master's thesis in the "Nanotechnologies for Biology and Spintronics" (*NaBis*) group at the *L-NESS* center in Como, under the supervision of Prof. R. Bertacco. My Master project was on the development of a platform, based on magnetic Domain Wall manipulators, for on-chip controlled drug delivery. After graduating, I accepted a grant for a Ph.D in the same group, still under the supervision of Prof. R. Bertacco, to continue the work on the applications of magnetic micro-technologies to cell biology.
My work has been supported by *Centro europeo di nanomedicina* (CEN) via the project "Forces, mechanisms and pathways involved in the ATR-mediated control of nuclear plasticity in response to mechanical stress"(Rif. EP002) and by *Fondazione Cariplo* via "UMANA" (Project No. 2013-0735). During

my Ph.D, I worked in a multidisciplinary environment, in contact with biologists, physicists and engineers. The design, development and fabrication of the devices was performed at *Polifab*, the micro- and nanofabrication facility at "Politecnico di Milano". At the beginning of my Ph.D, *NaBis* group moved from *L-NESS* center to *Polifab*, where a new cleanroom was starting-up. This allowed me to proper optimize most of the fabrication processes described in this work, developed *ad-hoc* for the fabrication of the devices. The biological experiments on magnetic domain wall tweezers were carried out at *IFOM* ("Istituto FIRC di Oncologia Molecolare"), in collaboration with Prof. M. Foiani and Prof. D. Parazzoli.
Finally, the biological work on magnetic pillars was performed in collaboration with Prof. G.V. Shivashankar at "Mechanobiology Institute" in Singapore, where I spent 6 months.
Here an overview of each chapter is presented:

- **Chapter 1: Introduction**. This chapter provides a brief description of the scientific background and a summary of this thesis work.

- **Chapter 2: Theory**. The theoretical aspects needed to understand the working principle of micromagnetic devices are illustrated. Besides, a description of magnetic nanoparticles behavior and the approach to calculate magnetic forces exerted by Domain Walls are provided. Finally, principles of microfluidics, required for a better comprehension of the experimental work, are presented.

- **Chapter 3: Experimental methods**. This chapter shows the experimental techniques used in this work. The fabrication methods, the characterization techniques, and the experimental setups used for characterization and tests are presented here.

- **Chapter 4: Magnetic domain wall tweezers**. The implementation of a micro-manipulation technique based on magnetic domain wall tweezers for studies in the field of mechanobiology is presented here. The fine manipulation of magnetic particles in a biological environment is demonstrated, together with a precise quantification of the mechanical stimuli applied on target cells. This method is exploited to inves-

tigate cell membrane deformations, when localized forces are applied on HeLa cells cultured on-chip. Finally, the possibility to manipulate particles microinjected inside the cell membrane, to exert mechanical stimuli at a subcellular level, is also demonstrated.

- **Chapter 5: Magnetically actuated micropillars**. An innovative technology based on magnetically actuated polymeric micropillars is presented. This magnetic pillars allow for the application of multiple and localized stimuli on individual cells in a unique fashion, mimicking the forces exerted by the extracellular matrix. In the first part of this chapter, the characterization of this technique is illustrated, measuring the magnetically induced pillars deflections and quantifying the forces applied on cells. In the second part, the biological validation is described and relevant results on cell and nucleus dynamics are presented.

- **Chapter 6: Conclusions and Perspectives**. This section summarizes the main results of this thesis and outlines the future perspectives.

Chapter 2

Theory

This chapter presents the theoretical background needed to understand the working principle of the micromagnetic devices developed in this thesis work. In the first part, the behavior of magnetic materials, when their dimensions scale down to the micrometric range, is described. In particular, the physical phenomena that determine the properties of a ferromagnetic body are introduced, highlighting the mechanisms that lead to the formation of magnetic domains and domain walls (DWs).
The second part deals with the physical behavior of the magnetic particles and illustrates the principle of particles manipulation by DWTs. Finally, basic concepts of microfluidics are introduced for a better comprehension of the experimental work.

2.1 Micromagnetism

The behavior of a magnetic object is described by the relation between the magnetization vector and the magnetic field: **M(H)**. A precise evaluation of this parameter is not a simple matter, as many physical phenomena contribute to determine the magnetic configuration of a certain magnetic body. Four energetic terms have to be considered: *exchange interaction, magnetostatic energy, magnetic anisotropy* and *Zeeman Energy.*
Considering the problem from a thermodynamic point of view, the equilibrium configuration of **M** arises from the minimization of the Free Energy

functional. The main difficulty of this kind of approach is that each contribution (in particular anisotropy and exchange) depends on the atomic structure of materials, consequently the energy minimization has to be calculated in an infinite dimensional space, taking into account the spatial coordinates of each atom.
To overcome this limitation, a theory named *micromagnetism* was developed. It relies on the idea that a magnetic material can be divided into small volume elements ΔV, where the magnetization ($\mathbf{M}$) is considered uniform. These volume elements are small compared to the characteristic length of variation of the magnetization, but large enough to apply statistics and thermodynamics rules.
In the micromagnetic theory, the free energy is expressed according to the *continuum approximation*, i.e. $\mathbf{M(r)}$ is considered a smoothly varying function. Moreover, the relaxation time for reaching the thermal equilibrium in each volume element (ΔV) is assumed to be sensibly shorter than the relaxation time for the entire system.
In the following sections, the physical mechanisms responsible of the magnetization in a magnetic object are described.

2.1.1 Exchange interaction

Exchange energy is a quantum mechanic effect related to the interaction between magnetic spins. It promotes parallel (in ferromagnetic materials) or anti-parallel (in antiferromagnets) orientations of spins along interatomic distances. It is usually expressed by the *Heisenberg Hamiltonian*:

$$H_{exchange} = -\sum_{i=j=1}^{N} J_{ij}\mathbf{S}_i \cdot \mathbf{S}_j \tag{2.1}$$

where $\mathbf{S}_i$ is the spin angular-momentum operator of the ion located at the i-th site of a lattice, and J_{ij} measures the strength of the exchange coupling between the moments i and j. The exchange energy is a short-range term and it decreases rapidly with increasing the distance between atoms, so that it can be calculated taking into account only the interactions between the nearest neighbors.

Replacing the quantum operators with classical vectors and considering a small angle between neighboring spins, the exchange contribution can be written as follows:

$$E_{exchange} = \int_V \frac{A}{2}[(\nabla m_x)^2 + (\nabla m_y)^2 + (\nabla m_z)^2]dV \tag{2.2}$$

where m is defined as the ratio between M and the saturation magnetization M_S and A (measured in J/m) is the so-called exchange constant, which allows to evaluate the strength of the exchange interaction. For a cubic lattice A is defined as:

$$A = \frac{2JS^2c}{a} \tag{2.3}$$

where a is the distance between nearest neighbors and c is a parameter which depends on the atomic structure of the magnetic material[74]. From the exchange energy contribution, the most important length scale in micromagnetism, i.e. the exchange length l_{ex}:

$$l_{ex} = \sqrt{\frac{A}{\mu_0 M_s^2}} \tag{2.4}$$

It describes the length over which **M** rotates and it is calculated considering only exchange and magnetostatic energy, while neglecting anisotropy. This parameter allows to distinguish "small" bodies which are uniformly magnetized in a single domain state and "large" materials where non-uniform magnetic configurations (multi-domains) occur. Furthermore, in the micromagnetic approach, the magnetic body has to be divided in volume elements smaller than l_{ex}, in order to consider a uniform magnetization inside each one.

2.1.2 Magnetic anisotropy energy

Many magnetic materials are magnetically anisotropic. A relevant case is the magnetocrystalline anisotropy that arises as a result of the coupling between the spin and orbital motion of electrons in the crystal lattice. This produces stable directions of spontaneous magnetization, or easy axes, along which the magnetization preferably aligns. If **M** is not aligned along such directions,

an energetic cost has to be paid by the system and it is taken into account in the total free energy.
This term represents the work required to align **M** along a different direction from an easy one. Considering an uniform value of the magnetization in each small volume partition, in case of uniaxial anisotropy, is possible to write the anisotropy energy density $e_{AN}(\mathbf{m})$ as a series of trigonometric functions:

$$e_{AN} = K_0 + K_1 sin^2\theta + K_2 sin^4\theta \tag{2.5}$$

where θ is the angle between the anisotropy axis and **M**. K_0, K_1, K_2 are measured in J·m^{-3}. Values of K_1 range from ≈1 kJm^{-3} to ≈50 MJm^{-3}. Moreover, K_1 depends on the temperature and it tends to zero at the Curie temperature.
As mentioned above, this expression is valid only for an uniaxial anisotropy. There are different expressions of the anisotropy energy for different symmetries (related to the lattice geometry) that can be found in literature[74].

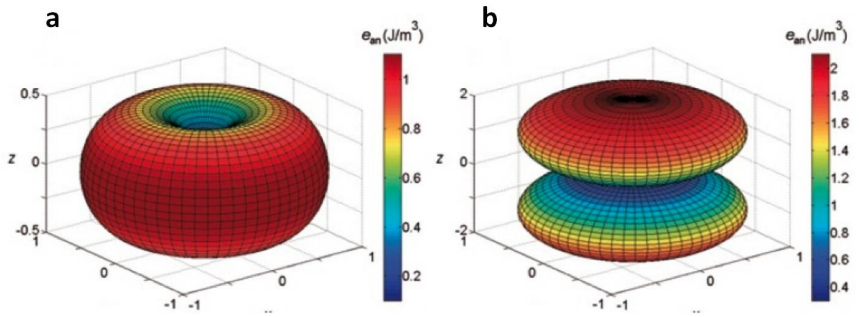

Figure 2.1: Uniaxial anisotropies represented by energy surfaces. The length of the plotted radial coordinate is proportional to the energy density for that direction. The anisotropy constants are chosen to illustrate different cases at similar energy scales. **a** Easy perpendicular direction ($K_1 > 1$) and **b** Easy plane ($K_1 < 1$).

K_1 can be either larger or smaller than zero. In the first scenario, a preferred (easy) axis for magnetization occurs, in the second one a preferred (easy) plane (see Fig. 2.1). A relevant field, expressing the strength of the

magnetic anisotropy, is the *anisotropy field* defined as follows:

$$H_{AN} = \frac{2K_1}{\mu_0 M_S} \tag{2.6}$$

H_{AN} is the field required to saturate the magnetization along the hard-axis. In a three dimensional picture, easy directions are associated with the minima of the anisotropic energy function, whereas maxima and saddle points are related to hard-axis and medium-axis.

2.1.3 Magnetostatic and Zeeman Energy

The *Magnetostatic Energy* is defined as the mechanical work spent for bringing together the magnetic moments that form the body from infinity to their final position, within the macroscopic material. It is essentially the dipole-dipole interaction energy of the system. Compared to exchange, it is a long range contribution.
Considering a magnetic body in a certain region of space, the magnetostatic energy can be expressed as:

$$U = E_{magstat} = -\frac{1}{2}\mu_0 \int_\Omega \mathbf{M} \cdot \mathbf{H}_d d\Omega \tag{2.7}$$

where the integration is performed over the entire magnetic material. $\mathbf{H}_d$ represents the *demagnetizing field*, i.e. the field produced by the magnetic body due to its magnetization. For a magnetic material with a second order surface, $\mathbf{H}_d$ can be written as:

$$\mathbf{H}_d = -N\mathbf{M} \tag{2.8}$$

where N is the demagnetizing tensor, strongly affected by the shape of the material, and $\mathbf{M}$ the magnetization of the object.
The magnetostatic energy is at the origin of the *shape anisotropy*. For a peculiar shape of the body, which is analytically expressed by N, the magnetostatic energy is minimized when the magnetization tends to stay parallel to the direction of elongation of the body. In a thin film, $\mathbf{M}$ lies in the plane, while in a stripe it tends to align with the major axis. This term plays a

fundamental role in the determination of the magnetic configurations of the devices developed in this thesis work.

Applying an external magnetic field, a torque is exerted on each magnetic moment. The energy term that describes this phenomenon is called *Zeeman energy* and it is expressed as follows:

$$E_{Zeeman} = -\mu_0 \int_V \mathbf{H}_e \cdot \mathbf{M} dV \tag{2.9}$$

where $\mathbf{H}_e$ is the external magnetic field.

2.2 Magnetic domains

Considering all the aforementioned energy contributions of the exchange coupling, demagnetization, anisotropy and Zeeman terms, the total free energy (E_{TOT}) of a magnetic system can be written as[75]:

$$\begin{aligned} E_{TOT} = \int_V \Bigg\{ \frac{A}{2} \Big[\Big(\nabla m_x\Big)^2 + \Big(\nabla m_y\Big)^2 + \Big(\nabla m_z\Big)^2 \Big] \\ + e_{AN} - \frac{1}{2}\mu_0 \mathbf{M} \cdot \mathbf{H}_d - \mu_0 \mathbf{M} \cdot \mathbf{H}_e \Bigg\} dV \end{aligned} \tag{2.10}$$

where $\mathbf{M}$ is the magnetization and $m = M/M_s$. $\mathbf{H}_d$ and $\mathbf{H}_e$ are respectively the demagnetizing field and the external magnetic field. As mentioned before, the local minima of this energy expression correspond to the metastable states of $\mathbf{M}$, i.e. the equilibrium configurations of a certain magnetic body. Landau and Lifschitz in 1935 showed theoretically that the existence of domains is a consequence of E_{TOT} functional minimization[76]. Indeed, domains formation arises from the combination of the terms that appear in E_{TOT}.
The exchange coupling promotes magnetization states where $\mathbf{M}$ is aligned within the entire volume. The absolute orientation of $\mathbf{M}$ is not relevant in this contribution but each configuration with a non uniform magnetization produces an energetic cost. Instead, magnetocrystalline anisotropy favors the alignment of $\mathbf{M}$ along easy axis or easy planes within the magnetic object. For this reason, an energetic penalty is paid if $\mathbf{M}$ is not oriented accordingly

with easy directions. Moreover, the magnetostatic energy promotes micromagnetic configurations in which **M** follows close paths within the magnetic body, in order to reduce the stray field outside. This fact can be in competition with the requirement for minimizing the exchange and the anisotropic energy contributions. A quantity to evaluate the relative weight between magnetocrystalline and shape anisotropy is the following:

$$k_{M-A} = \frac{H_{AN}}{M_S} = \frac{2K_1}{\mu_0 {M_S}^2} \tag{2.11}$$

For soft materials, (where $k_{M-A} \ll 1$) the magnetic behavior is dominated by shape anisotropy or magnetostatic energy. On the contrary, in hard materials ($k_{M-A} \gg 1$) magnetocrystalline anisotropy leads.
The break-up of magnetization in domains which ensures a flux closure configuration at the specimen boundaries, is mainly due to the minimization of the dipolar energy. On the contrary, a multi-domains configuration presents a large number of *domain walls* (region between two neighboring domains) that imply an energetic cost due to exchange and anisotropy.
For example, figure 2.2 illustrates three different configurations for the domain structure within a magnetic material.

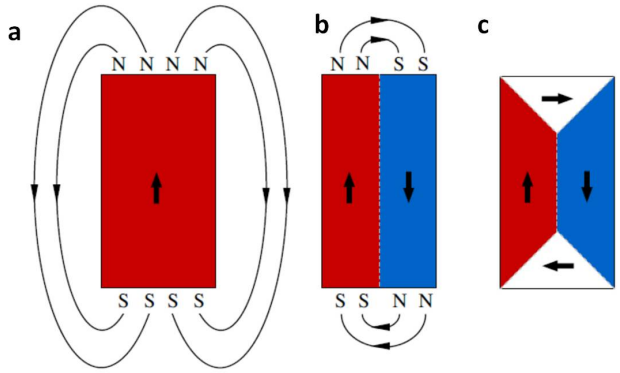

Figure 2.2: Magnetic domains structures: from **a** to **c** the magnetostatic energy decreases due to domains formation. Adapted from[76].

A mono-domain state (**a**) has no domain walls, but the magnetostatic energy of the system is large. This energetic term is lowered by the creation of

antiparallel domains (**b**). A closure domain structure (**c**) further decreases the demagnetizing energy, even though introduces several domain walls.

2.2.1 Domain walls

Magnetic domains are separated by domain walls (DWs), i.e. interface regions where the magnetization changes gradually from one direction to another.

For creating domains, work has to be done against the exchange torque, which tends to align spins. Without considering the presence of DWs, the cost of exchange energy would be extremely large and multi-domains configurations, where **M** changes abruptly from one direction to another, would be always energetically unfavored.

The anisotropy tries to promote a thin wall (where fewer spins are not aligned with the easy axis) whereas the exchange acts in favour of a thick wall (a gradual variation of the angle between neighboring spins reduces the exchange energy). According to the way spins rotate across the wall, two classes of domain walls can be found: Bloch and Néel DWs (see Fig.2.3).

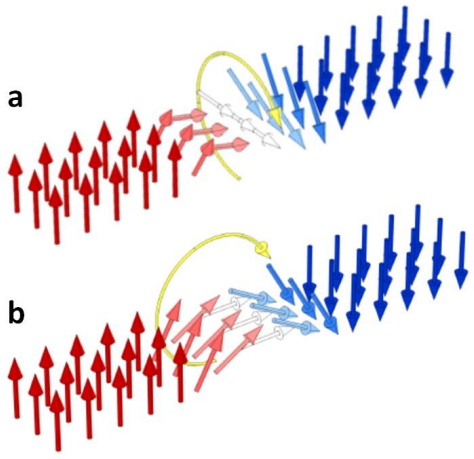

Figure 2.3: Two types of domain walls, Bloch wall (**a**) and Neel wall (**b**).

In a Bloch wall, the spins rotate in the domain wall plane. In a Néel wall the spins twist in a plane perpendicular to the domain wall plane. The for-

mer one is favored in bulk materials. Néel walls are instead promoted in thin films, mainly because they avoid the dipolar energy cost related to spins directed perpendicular to the plane.

Néel domain walls in thin film materials

As discussed in the previous sections, in thin films, the micromagnetic configuration is not only determined by the intrinsic magnetic properties, but the shape of materials plays also a relevant role. In particular, it is preponderant in soft magnetic material where the magnetocrystalline anisotropy is negligible and the equilibrium state is essentially related to the material geometry. Hence, the magnetic configuration and the magnetization reversal can be engineered by choosing the appropriate morphology and controlling the external field.
Indeed, in elongated structures, as conduits or stripes, **M** is oriented along the major axis for shape anisotropy. In multi-domains configurations, domain walls (DWs) are nucleated. Two different spin configurations can be found in thin film conduits, which are variants of Néel walls: transverse and vortex DWs, illustrated in figure 2.4a. In a transverse DW, spins continuously rotate in the plane of the structure, from one domain to the adjacent one. Instead, a vortex DW results in a configuration where magnetic moments rotate in a clockwise or anticlockwise direction around the vortex core, where the magnetization points perpendicular to the film plane. The free energy of the two micromagnetic states varies with the dimensions of the magnetic conduits. The phase diagram between transverse and vortex configurations was calculated by McMichael et al.[77].
They took into account only the magnetostatic and exchange energy terms for a patterned stripe of Permalloy of thickness t and width w, obtaining the following relation: $wt = const \cdot \delta^2$.
This result, expressed as function of the dimensionless variables t/δ and w/δ, where $\delta = l_{ex}/2$, is illustrated in Fig.2.4b. For relatively narrow and thin conduits, transverse DWs are energetically favored; instead the vortex walls are promoted in wider and thicker stripes.

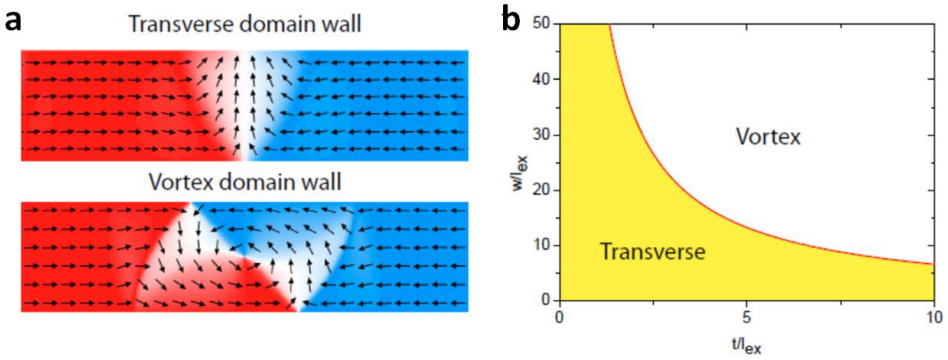

Figure 2.4: **a** Transverse and vortex spin-structures in infinitely long $Ni_{80}Fe_{20}$ stripes. DWs separate two domains (blue and red arrows) where **M** is oriented in opposite directions. **b** Phase diagram of a Néel wall (transverse and vortex spin structures) in a thin $Ni_{80}Fe_{20}$ stripe. δ, in this case, is equal to $l_{ex}/2$. Adapted from[77].

Magnetization dynamics

In this section, the physical mechanisms that govern the magnetization dynamics are described. As discussed in the previous sections, a particular magnetic configuration is a consequence of the total energy minimization. The energetic terms do not depend only on the intrinsic magnetic properties of the materials but also on their morphology and on the applied magnetic fields. For example, an external field can affect the energetic landscape, inducing changes in the magnetic configuration, which moves towards a new equilibrium. During this transition, the magnetization dynamics is described by the Landau-Lifshitz-Gilbert equation[75]:

.

$$\frac{\partial \mathbf{M}}{\partial t} = \gamma \mathbf{M} \times \mathbf{H}_{eff} - \alpha\gamma \mathbf{M} \times \frac{\partial \mathbf{M}}{\partial t} \tag{2.12}$$

where γ is the electron gyromagnetic ratio, α is the phenomenological damping coefficient and H_{eff} is the effective magnetic field. This is a fictitious field that takes into account all the energetic terms: the demagnetizing and external fields, but also the exchange interaction and the anisotropy.
The effective field exerts a torque on the magnetization vector. The first term

describes a pure gyroscopic effect. If **M** is not at the equilibrium, it will start to continuously precede around the field without reaching the equilibrium. The second term, phenomenologically introduced, takes into account the dissipative effects, i.e. the damping of the precessional motion which brings the system into the new state of equilibrium, where the magnetization is locally parallel to the effective field. Similarly to the viscous forces, the damping term is proportional to the temporal variation of the quantity of interest, in this case of the magnetization.
Of particular interest for this thesis work is the dynamic behavior of DWs. As discussed before, the material shape affects the magnetic configuration and the energetic-landscape. By using different geometries, well-defined attractive potentials can be engineered; they act as stable positions for DWs. Intuitively, the energy minima correspond to configurations where thin walls are promoted, since in first approximation the DW energy decreases with its dimension. Therefore, the DW nucleation is energetically favored in constrictions and narrow conduits.
A geometrical constriction, that acts as a *pinning site*, produces an attractive potential well for the DW. A prototypal example of such pinning sites are corners in microstructures[69].
When an external magnetic field is applied to the system, the DW experiments a change in the potential landscape. If the field intensity results in an energetic contribution large enough to overcome the potential arising from local pinning site, the domain wall propagates to a new equilibrium position. The propagation process of a transverse DW along a conduit has been studied in details by Walker[78] and Lee[79].
In this thesis work, controlled propagation of DWs in ring conduits is exploited to manipulate magnetic particles, which are described in the next section. Instead, the principle of DWT manipulation is explained in section 2.3.4.

2.3 Magnetic particles

In this section, the magnetic particles used in this work and their interaction with magnetic fields are described.

The behavior of a magnetic object is highlighted by its volume magnetic susceptibility (χ), which describes the magnetic response, in terms of magnetization, to an external field: $\mathbf{M} = \chi\mathbf{H}$. Considering a magnetic material, the total flux density $\mathbf{B}$ is:

$$B = \mu_0(\mathbf{M} + \mathbf{H}) = \mu_0(1 + \chi)\mathbf{H} = \mu_0\mu_r\mathbf{H} \tag{2.13}$$

where μ_0 is the permeability constant in vacuum and μ_r the relative permeability of the object. Depending on the response of the magnetic material to an applied field, different magnetic behaviors can be identified, such as diamagnetism (μ_r <1), paramagnetism (μ_r >1) and ferromagnetism ($\mu_r \gg$1). Reducing the dimensions of a magnetic material below a certain size, as in the case of nanoparticles, a different magnetic effect arises. It is called *superparamagnetism.*

2.3.1 Superparamagnetism

A superparamagnetic particle behaves as a macrospin (where spins are aligned as in a ferromagnet) whose total magnetic moment fluctuates over time, so that the net average magnetic moment is zero for long enough observation windows.
If we consider a small magnetic particle of volume V with a uniaxial anisotropy, two different magnetization states can occur, i.e. parallel or antiparallel to the easy-axis. These two states are separated by an energetic barrier which is proportional to K_1 (the anisotropy constant of the material) and to the particles volume. If the activation energy (K_1V) for flipping the magnetization from parallel to antiparallel is smaller than the thermal energy $\mathrm{k}_B T$, where k_B is the Boltzmann constant, thermal fluctuations allow a continuous magnetization reversal. The average time between two thermally activated transitions τ is provided by:

$$\tau = \tau_0 exp\left(\frac{k_1 V}{k_B T}\right) \tag{2.14}$$

where τ_0 ranges between $\approx 10^{-9}$ s and $\approx 10^{-11}$ s for single particles, and T is the absolute temperature. The energy barrier ($\mathrm{K_1V}$) decreases with the

particle size and, conversely, an enhancement of the flipping rate occurs. Superparamagnetism is a size-effect which depends either on the observation time t and on the temperature T. Magnetic particles are blocked, i.e. ferromagnetic, for an observation time much smaller than τ. Above the blocking temperature, defined as the temperature at which τ is equal to t, the particles are in a superparamagnetic state.
At room temperature, the maximum dimension of a superparamagnetic particle is strongly affected by the magnitude of anisotropy constant. For example, Fe_30_4 particles typically used in magnetic beads are superparamagnetic at room temperature up to ≈25 nm in diameter[80].
A superparamagnetic nanoparticle presents large saturation magnetization M_S, similar to ferromagnets, together with a negligible hysteresis and no remanence as a paramagnet. These properties make them suitable for several biological applications where formation of clusters should be avoided.

2.3.2 Superparamagnetic particles

A magnetic nanoparticle is usually composed by a superparamagnetic core surrounded by a non-magnetic coating (see Fig.2.5a). The latter is required to allow functionalizations with biomolecules of interest[81].

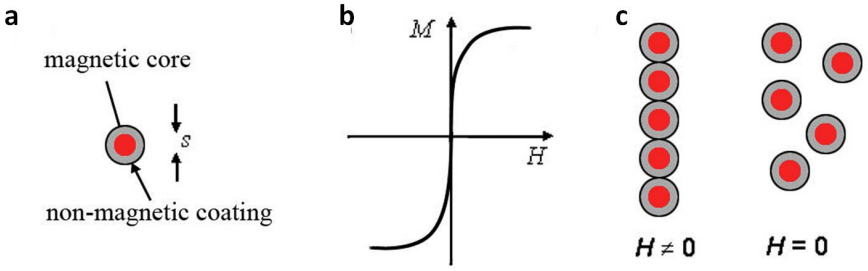

Figure 2.5: Scheme of a magnetic nanoparticle with a inner spherical core with a diameter s. **b** Magnetization cycle. **c** Cluster of nanoparticles in presence of an external magnetic field H. When the field is removed, the cluster is divided into individual particles. Adapted from[82].

Typically, particles have a size that ranges between 5 and 50 nm in diameter. Magnetic cores made of Iron oxides such as maghemite (Fe_2O_3) or magnetite (Fe_3O_4) are widely used for biological experiments, due to their reduced toxicity[83].
The magnetization curve of these particles is free of hysteresis, as illustrated in Fig.2.5b and this has important consequences for their applications. For example, they can be isolated from a solution by a large magnetic field gradient and re-suspended again when the field is removed (Fig.2.5b). However, relatively small magnetic moments make the application of relevant forces extremely challenging. Furthermore, the Brownian motion (see section 2.4.3) associated to the thermal agitation is higher as the nanoparticle size decreases; consequently, the manipulation of single superparamagnetic nanoparticles is complex.
In order to preserve the superparamagnetic properties, but achieving a larger magnetic moment and volume, bigger magnetic beads (0.1 to 5 μm in diameter) are used.

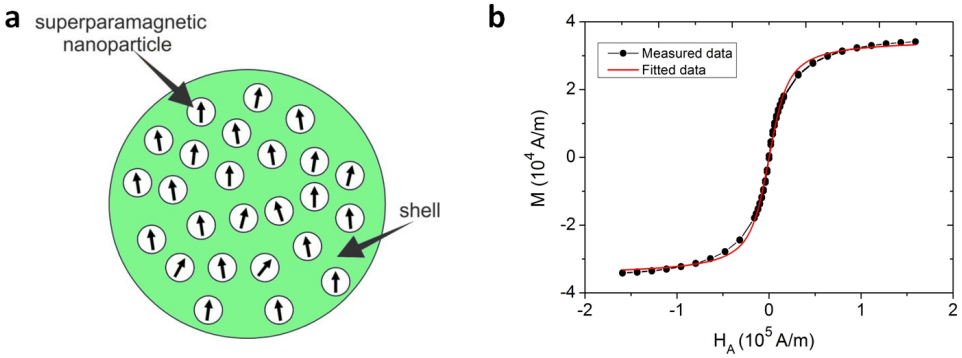

Figure 2.6: **a** Sketch of a superparamagnetic bead composed by magnetic nanoparticles in a non-magnetic shell/matrix. **b** Magnetization (M) of a 1μm *MyOne Dynabead* as function of the applied magnetic field (H_A) measured (black line) by VSM. Particles are diluted in H_2O to 50 μg/ml. The value of **M** for a single bead is extrapolated by the total magnetic moment. The experimental data are fitted with a Langevin function (red line).

They are fabricated embedding several magnetic nanoparticles, non interacting, in a non-magnetic shell. A sketch of a magnetic bead made by superparamagnetic particles cores in a polymeric matrix is shown in Fig.2.6a.
The magnetic response of such superparamagnetic particles is described by the Langevin function ($L(x) = coth(x) - 1/x$), as:

$$M(H) = M_S\left(coth\left(\frac{3\chi_0 \cdot H}{M_S}\right) - \frac{M_S}{3\chi_0 \cdot H}\right) \tag{2.15}$$

where M_S is the saturation magnetization and χ_0 is the linear magnetic susceptibility coefficient describing the linear dependence between **M** and **H** for small values of **H**. The typical magnetization curve of a superparamagnetic bead is illustrated in Fig.2.6b.
In this thesis work, two different superparamagnetic beads are used (see Chapter 4). Commercial *MyOne-Dynabeads* (Invitrogen) superparamagnetic particles functionalized with $COOH^-$ are exploited for studying the cellular membrane deformation. They are 1 μm in diameter, with a magnetization of saturation $M_S = 35 \times 10^3$ A m^{-1} and magnetic susceptibility in the linear range $\chi_0 = 1.46$. The values of χ_0 and M_S are measured by Vibrating Sample Magnetometry (VSM). Their magnetic response as function of the external magnetic field is illustrated in Fig.2.6a.
For the experiments of particles manipulation inside the cell membrane, we used commercial *nanomag-CLD* (micromod) superparamagnetic beads with a polymeric matrix in dextran. They are 500 nm in diameter, functionalized with $COOH^-$ and *Cy5*, a fluorescent marker in the far-red.

2.3.3 Magnetic force on beads

The evaluation of the force exerted on a body in a magnetic field is not a trivial problem. To precisely determine the most general expression for such force, the Maxwell *stress tensor* has to be calculated, as discussed by Landau and Lifshitz in Ref.[84]. Here, we report this treatment using the same notation of the authors in the c.g.s. system.
According to this approach, the force acting on a finite volume can be reduced to the forces applied to the surfaces of that volume[85]. Noteworthy, the force acting on a volume element dV corresponds to the change in its

momentum per unit of time. This change has to be equal to the amount of momentum "entering" the volume through its surface, again per unit of time. As a consequence, the i-th component of the force (F_i) acting on a body can be written as follows:

$$F_i = \int_V f_i dV = \int \int_S \sigma_{ik} ds_k \tag{2.16}$$

where the integration on the right term is on the surface of the volume V. f_i is the i-th component of the force density, σ_{ik} is the stress tensor and ds_k is the surface element. The i-th force component on a surface element is $\sigma_{ik} ds_k = \sigma_{ik} n_k ds$ ($\mathbf{n}$ is a unit vector pointing outwards the surface of the volume element along the normal direction). Starting from Eq.2.16, is possible to derive the following result[84]: $f_i = \partial \sigma_{ik} / \partial x_k$, where x_k is the k-th spatial component. In this way, the force can be directly calculated from the derivative of the stress tensor.
The general expression of σ_{ik} for a body in a magnetic field can be written as follows[84]:

$$\sigma_{ik} = -p_0(\rho, T)\delta_{ik} - \frac{H^2}{8\pi}\left[\mu - \rho\left(\frac{\partial \mu}{\partial \rho}\right)\right]\delta_{ik} + \frac{\mu H_i H_k}{4\pi} \tag{2.17}$$

where p_0 is the pressure on the object in absence of magnetic field (at a fixed temperature and density), ρ is the density of the body and T is the temperature. $\mathbf{H}$ is the total field acting on the body and μ is the magnetic permeability ($\mathbf{B} = \mu\mathbf{H} = (1 + \chi(H))\mathbf{H}$). From Eq.2.17 is possible to calculate the force density, as previously discussed.
Considering that $\nabla \cdot \mathbf{B} = 0$ and $\nabla \times \mathbf{H} = \mathbf{j}$, the force density can be written as follows (see Ref.[84] for the derivation):

$$\mathbf{f} = -\nabla p_0(\rho, T) + \frac{1}{8\pi}\nabla\left[H^2 \rho\left(\frac{\partial \mu}{\partial \rho}\right)\right] - \frac{H^2}{8\pi}\nabla\mu + \frac{\mu}{c}(\mathbf{j} \times \mathbf{H}) \tag{2.18}$$

In absence of conduction currents ($\mathbf{j}$=0, as in the case of a particle attracted by a DW), the last term is zero. Furthermore, the first term (p_0) is not related to the magnetic properties of the body and does not play a role in the evaluation of the magnetic force. Finally, $\rho\left(\frac{\partial \mu}{\partial \rho}\right) \approx \mu - 1 \approx \chi(H)$, is valid in most cases[84]. Integrating on the whole volume and reverting to the

S.I., where $\mu = \mu_0(1 + \chi(H))$, the magnetic force $\mathbf{F}_M$ acting on a magnetic body can be written as follows:

$$\mathbf{F}_M = \frac{\mu_0}{2} \int_V [\nabla(\chi(H)H^2) - H^2 \nabla\chi(H)]dV \tag{2.19}$$

Note that, the second term is also negligible if the magnetic susceptibility is nearly uniform all over the magnetic body, as happens for superparamagnetic particles when low external magnetic fields are applied ($\chi(H) = \chi_0$), resulting in the notorious expression:

$$\mathbf{F}_M = \frac{\mu_0 \chi_0}{2} \int_V \nabla H^2 dV \tag{2.20}$$

Several works [86],[87] rely on this equation for the calculation of the force acting on a superparamagnetic bead. However, if the magnetic susceptibility is not uniform, the second term in Eq.2.19 is not negligible and it has to be taken into account.
In the calculation of the force exerted on superparamagnetic beads by DWTs (see Chapter 4), this term is also considered, as the beads experiment the non-homogeneous stray field produced by DWs. For typical values of the total field acting on a particle, the correction introduced by this term is around 10% of the total force. Considering $\mathbf{M}= \chi(H)\mathbf{H}$, Eq.2.19 can be written as follows:

$$\mathbf{F}_M = \frac{\mu_0}{2} \int_V \left[\nabla(\mathbf{M} \cdot \mathbf{H}) - H^2 \nabla\left(\frac{\mathbf{M}}{\mathbf{H}}\right) \right] dV \tag{2.21}$$

where $\mathbf{M}$ is the magnetization of the magnetic object and $\mathbf{H}$ is the total magnetic field acting on that object. In chapter 4, the Magnetization is calculated according with the magnetic susceptibility of the beads, measured by Vibrating sample magnetometry (see Fig.2.6b). The total field, instead, takes into account the applied field, the stray field exerted by DWs and the dipolar interaction with the other particles (if clusters of beads are formed).

2.3.4 Working principle of Domain Wall Tweezers

As discussed in section 2.2.1 the DWs can be nucleated and propagated in magnetic microstructures. In thin films conduits, Néel walls produce a highly

inhomogeneous stray field gradient ($\nabla \mathbf{H}_d$), up to 100 mT/μm[69], which attracts (see Eq.2.21) superparamagnetic particles in suspension. This stray field is spatially localized, thanks to the very reduced dimension of the DW. Hence, the DW acts as movable attracting pole, allowing for particle manipulation (see Fig.2.7).

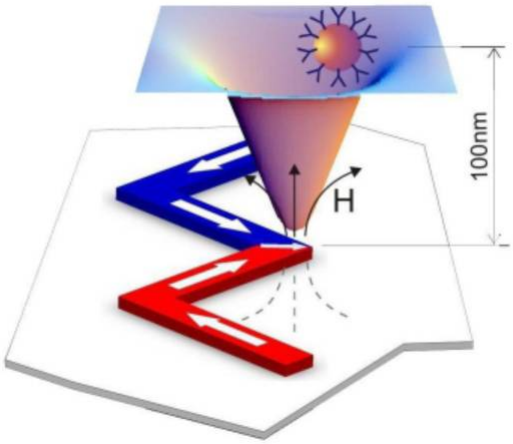

Figure 2.7: Sketch of a Permalloy nanostrip with a domain wall at a corner and the corresponding potential energy surface for a magnetic bead carrying antibodies on a plane at a distance 100 nm from the $Ni_{80}Fe_{20}$ structure. Adapted from[69].

The total field, comprising the stray field produced by the DW and the external magnetic field ($\mathbf{H}_d$+$\mathbf{H}_e$), induces a magnetic moment in the particle. An attracting force is thus exerted by the DW, due to the intense gradient of $\mathbf{H}_d$ (see Eq.2.21), which traps the magnetized particle. The minimum of the potential energy at a fixed height, typically imposed by the physical surface of the chip where particles are manipulated, is located in the proximity of the DW, where the gradient is maximized. In addition, when the DW is displaced applying an external field, the particle also moves, following the motion of the attractive potential produced by the DW. Therefore, a superparamagnetic particle can be trapped and manipulated by DW motion. This technology has been patented by the *NaBis* group in collaboration with nanoGUNE research center[88].

It allows a maximum transport speed of 15μm/s[88] which is affected by several parameters, such as particles and conduits geometry and magnetic properties, together with the viscosity of the fluid where particles are diluted. Different geometries can be used to control the DWs propagation in thin films and to exert intense stray fields for particles manipulation. An example is provided by zig-zag shaped conduits, where DWs are displaced from corner to corner and particles are handled accordingly, in a step-by-step motion[89]. Also square-shaped nanostructures are used[69], again exploiting the corners as pinning sites for DWs. Curved geometries[67],[68] offer an additional advantage: DW position inside the conduit is precisely determined only by the direction of the external magnetic field and no pinning sites are required to control DWs propagation (see Chapter 4). This allows a continuous motion of the particles that can be manipulated with a spatial resolution down to 100 nm[69]. In this thesis work, ring-shaped conduits in $Ni_{80}Fe_{20}$ are used (see Chapter 4) to implement domain wall tweezers.

2.4 Microfluidics

This section introduces some basic concepts of microfluidics, used in the experimental evaluation of the force exerted by DWTs (see chapter 4), which relies on the comparison between the hydrodynamic force and the magnetic one in a microfluidic channel.

2.4.1 Reynolds number and laminar flow

In fluid-mechanics, a fluid is called *Newtonian* when its viscosity does not depend on the mechanical stress applied on it. The properties of these fluids are completely described by their density and viscosity.
Considering the motion of a Newtonian fluid, it is possible to distinguish between two different regimes: the *laminar flow*, where the fluid moves in parallel layers without lateral mixing, and the *turbulent flow* characterized by rapid variations of pressure and speed in space and time, with the formation of eddies and vortexes.

In the laminar regime, the friction dominates and the fluid molecules respond uniformly to external forces. Instead, in the turbulent flow the inertial effects are relevant and cause the liquid to protract its motion, leading to a chaotic behavior.
It is impossible to identify an absolute rule for distinguishing between fluids displaying turbulent or laminar flow[90]. In fact, the flow is not determined only by the fluid properties but also by the forces acting on it.
A parameter that can be used to distinguish between the two regimes is the so-called *viscous critical force* (F_{cr}), defined as:

$$F_{cr} = \eta^2/\rho \tag{2.22}$$

where ρ and η are respectively the fluid density and viscosity; F_{cr} has the dimension of a force. If the ratio between the force applied on the fluid and the viscous critical force is much larger than 1, the inertial forces, proportional to the density, dominates the fluid dynamics. In these conditions, the fluid flow is turbulent, otherwise it is laminar. Note that, if sufficiently low forces are applied, the fluid is always in laminar regime, regardless its density and viscosity.
Another and better known parameter to identify the flow regime is the *Reynolds number* (Re), a dimensionless quantity, defined as the ratio between inertial and viscous forces within the fluid[91]:

$$Re = \frac{\rho\langle v\rangle L}{\eta} \tag{2.23}$$

where $\langle v\rangle$ is the average fluid velocity (with respect to the system), L is the characteristic length of the system and η is the dynamic viscosity[90].
Differently from the viscous critical force, the Reynolds number is not dependent only on ρ and η, but also on properties of the whole system, such as the fluid velocity and the system geometry. It can be inferred by the definition that for high Reynolds number the inertial term prevails, resulting in a turbulent flow. Instead, the transition to laminar flow occurs for Re ranging between 1000 and 4000. The transition value is not precisely determined, since the behavior of fluids depends also on shape and roughness of the surfaces on which the fluid is flowing (not taken into account by Re). For

this reason, the Reynolds number provides only a general indication and it is not effective to describe the fluid motion when the value is closed to the transition one.

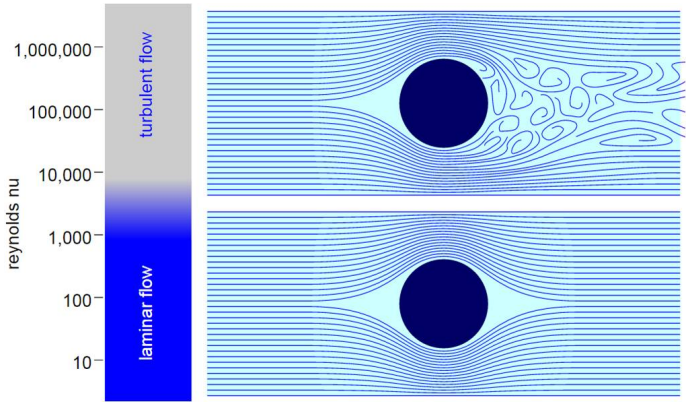

Figure 2.8: Sketch showing how laminar and turbulent flow occurs at different Reynolds number.

The Reynolds number in the experimental conditions of this thesis work, i.e. micrometric distances and maximum velocities in the order of few cm/s, ranges from 0.1 to 1, well below to the transition value. This is a notorious result: the flow of a Newtonian fluid is always laminar in the "microworld". This result is also consistent with numerical simulations presented in chapter 4.

2.4.2 Stokes flow

Fluid flux is precisely described by the *Navier-Stokes equations*, which are extremely complex and, up to date, there is no proof of existence and smoothness of general solutions. However, in some particular cases such equations can be simplified.
In this section, some interesting results arising from Navier-Stokes equations are presented. A rigorous derivation of the following expressions are found in Ref.[91].
For small Reynolds numbers ($Re \ll 1000$), inertial terms can be neglected[91]. Assuming also that the fluids are incompressible, Stokes derived the drag

force acting on a spherical body of radius R_b, moving at a speed $\mathbf{u}$ in a fluid flowing with a certain velocity $\mathbf{v}$:

$$\mathbf{F}_{drag} = 6\pi\eta R_b(\mathbf{v} - \mathbf{u}) = \xi(\mathbf{v} - \mathbf{u}) \tag{2.24}$$

where ξ is a drag constant, which highlights the linear dependence between the velocity of the body and the drag force.
In the experimental work, this equation is used to evaluate the hydrodynamic force exerted on a magnetic particle, trapped by DWTs.
Another relevant example is the so-called *Poiseille flow*. It is a solution of Navier-Stokes equations for a fluid moving in a rigid pipe, when a pressure difference is applied at the extremities of the conduit. The analytical solution is possible only for simple geometries; an interesting case is the infinite parallel plates channel, where the width largely exceeds the height. According to no-slip boundary condition, which imposes a null fluid velocity in contact with the walls, the solution is:

$$\mathbf{v}_x(z) = \frac{\Delta p}{2\eta L}(h - z)z \tag{2.25}$$

where h is the distance between the parallel plates and Δp is the pressure difference between two channel sections at a distance L. The fluid velocity has a parabolic profile, with the maximum value in the middle of the channel. In the experimental work, beads are trapped close to the channel wall, far from the center. Hence, the fluid velocity experimented by the particles is lower than the average velocity inside the channel and a correction factor (K) has to be included in Eq.2.24.
Furthermore, a second coefficient (λ) is used to take into account the so called *wall effect*. The presence of a wall prevents the fluid from flowing along the trajectories it would follow in a bulk sample, increasing the friction exerted on the bead and, consequently, the drag force. This correction factor can be calculated numerically as follows[92]:

$$\lambda_{||}(z) = \left[1 - \frac{9}{16}\frac{R}{z} + \frac{1}{8}\left(\frac{R}{z}\right)^3 - \frac{45}{256}\left(\frac{R}{z}\right)^4 - \frac{1}{16}\left(\frac{R}{z}\right)^5\right]^{-1} \tag{2.26}$$

Where the subscript $||$ indicates a motion parallel to the wall, R is the radius of the bead and z the distance between the center of the bead and the wall.

During the experiments, beads are trapped on the surface, resulting in $z = R$; λ is maximum in this case, equals to 3.08.
The expression of the drag force which included λ and K is reported in Eq.4.4.

2.4.3 Diffusion and brownian motion

Particles in a fluid experience either the drift due to the fluid flow and the diffusion arising from the random collisions with fluid molecules. The drift can be determined by the Stokes equation, described in the previous section. Instead, the diffusion is due to the thermal agitation of fluid molecules which hit the particle, resulting in a random-walk called *Browninan motion*. This is a stochastic phenomenon, where the mean square displacement of a particle $\langle r^2 \rangle$ is calculated as:

$$\langle r^2 \rangle = 2nDt \tag{2.27}$$

n the dimensionality of the system and D is the *diffusion coefficient*, which depends both on the fluid properties and on the diffusing object geometry. From Eq.2.27, an expression for the diffusion length (l_{diff}), i.e. the average distance travel by a particle in a time t, can be obtained:

$$l_{diff} = \sqrt{Dt} \tag{2.28}$$

Furthermore, although drag and diffusion describe two different macroscopic phenomena, they are both originated by collisions between fluid molecules and dissolved particles. Einstein found a relation between them, for a system at the thermal equilibrium. This notorius equation provides a microscopic expression for the diffusion constant[93]:

$$D = \frac{k_B T}{\xi} \tag{2.29}$$

where ξ is the drag coefficient (see Eq.2.24) which also depends on the properties of the fluid and the particle geometry. Combining the Stokes equation with Eq.2.28 and Eq.2.29, the diffusion length of a spherical particle results:

$$l_{diff} = \sqrt{\frac{k_B T}{6\pi\eta R_B} t} \tag{2.30}$$

where R_B is the particle radius, and η the fluid viscosity. From the calculation of the diffusion length, is possible to appreciate how Brownian motion significantly affect the particles position, in absence of external forces. For example, 1 μm particles travel an average distance of 663 nm in 1 s and l_{diff} increases for smaller particles. For 100 nm beads the diffusion length becomes $\approx$ 2 μm after 1 s, twenty times larger than the particle size.

Chapter 3

Experimental Methods

This chapter presents an overview of the experimental techniques for the microfabrication and characterization of the devices developed in this thesis, together with a description of the experimental setups used for the biological studies.

3.1 Optical litography

Optical lithography or photolithography is a widespread method for microfabrications which combines high throughput and good spatial resolution ($\approx$1 μm). This technique relies on transferring a certain geometry patterned on a template (i.e. the mask) to a sample, exploiting the change in solubility of a suitable polymer, called photoresist, when it is exposed to UV light.
First, the photoresist is cast over the whole substrate, then the mask is placed upon the sample which is exposed to UV light. The pattern on the mask is defined by the contrast between the area which is transparent to UV light and the zones which are not. As a consequence, after UV irradiation, the resist presents soluble and non-soluble zones. In the next step, called *development*, the sample is treated with a suitable solvent (the developer) which removes the soluble zones without affecting the non-soluble ones, thus reproducing the mask geometry on the sample.
Finally, the pattern is effectively transferred by either etching away (sub-

tractive process) or covering with additional material (additive process) the zones which are unprotected by the resist.
A lithographic process can be divided in 6 steps (see Fig.3.1): (a) Sample cleaning, (b) Photoresist spin-coating, (c) Sample exposure to UV light, (d) Resist development, (e) Additive or subtractive process, (f) Photoresist removal (*lift-off* procedure).

3.1.1 Pohotolithographic process

In this section all the steps involved in the optical lithography are described.

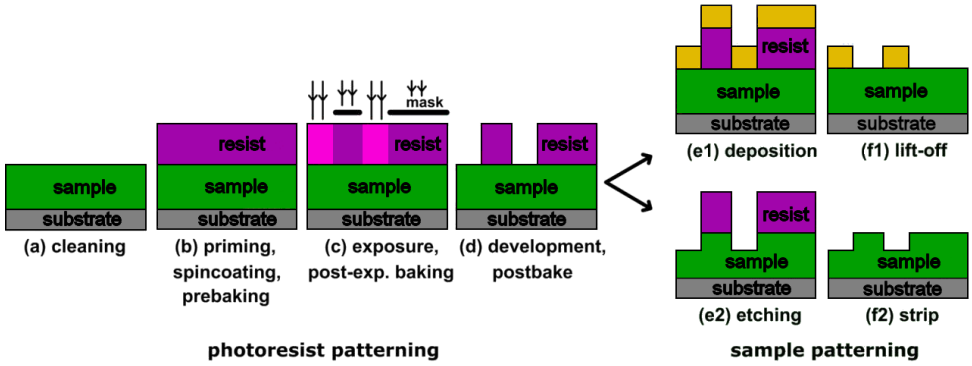

Figure 3.1: Main steps of a photolithographic process with positive resist.

Sample cleaning. Contaminations on the sample surface can partially prevent the photoresist adhesion and negatively affect the quality of the pattern. In case the sample is already cleaned, a pre-heating of the same at T= 120-140 ^{o}C for 2 minutes is enough for allowing the desorption of water from the surface. If the surface is contaminated by organic impurities, the standard cleaning procedure relies on an ultrasonic bath in acetone and a subsequent isopropyl alcohol rinsing. Otherwise, if the sample is heavily contaminated, a *Piranha* solution is used for the cleaning. *Piranha* is a mixture of Sulfuric acid (H_2SO_4) and hydrogen peroxide (H_2O_2) in a ratio of 5:1, used to remove all the organic residuals.

Photoresist spin-coating. For the fabrication of the devices presented in this thesis work *AZ5214E* photoresist (Microchemicals-USA) is used. It is deposited on the samples via spin coating. In this step, the resist is dispensed on the substrate by a pipette, then the sample is rotated at 5000 rpm for 60 s. The centrifuge spreads the resist, producing a uniform, thin (1.2 μm) layer. After the spin-coating, a soft baking at 110^{o}C for 90 s is performed. This allows the complete evaporation of the solvent containing the polymer and the enhancement of resist adhesion on the sample surface.

Exposition. Exposure to UV radiation alters the photoresist chemical properties, resulting in a different solubility of the exposed and non-exposed area. The micrometric image on the mask, obtained by patterning with Cr a transparent quartz substrate, is transferred on the sample because the metal (Cr) protects the underlying resist from the UV light. The mask is precisely aligned with the substrate by a *mask-aligner*; the machine used in this work is the *Karl Suss Mask Aligner MA6* (see Fig.3.2a), both in the contact and proximity modes, allowing for the exposure of wafers up to 6" in diameter. The UV radiation is provided by the I-line (at 365 nm) of a mercury lamp with an intensity around 4.5 mW/cm^2.
The resist employed (AZ5214E) is positive; this means that the irradiation provokes a breaking of the polymeric chains, enhancing the solubility of the photoresist in the exposed area and consequently favors its removal during the development step. The maximum resolution achievable, measured as the linear size of the smallest object that can be transferred from the mask, is 1.5 μm, operating in *hard* contact. This parameter is affected by the mask quality, by the light confinement and by the photoresist properties and contrast. In a high contrast resist, the difference in solubility between non-exposed and exposed area is increased, because it is less sensitive to the scattered radiation from the irradiated zones. This results in the formation of vertical profiles and well defined edges after developing. The UV light provides the resist with the energy required to break the polymeric chains; AZ5214E photoresist becomes soluble with an optimal dose of 120 mJ/cm^2.

Development. An appropriate solvent, called *developer*, is used to remove the soluble part of resist, without affecting the non-soluble zones. In case of positive resist, the exposed area is dissolved, while the zones protected by the mask during exposure remains on the substrate. For a negative resist, the mechanism is the opposite (non-exposed area is more soluble). The photoresist is developed in AZ726MIF (microchemicals-USA) for 30 s and subsequently rinsed in water.
After the development, two different strategy can be used to define a pattern on the sample: removal or addition of material on the zones unprotected by the photoresist. They are respectively subtractive or additive processes. Finally, the resist is completely removed from the sample by *lift-off* procedure.

Subtractive process: etching. Ion beam or reactive ion etching techniques, described in section 3.4, allow the removal of the sample material by collision with accelerated ions. In this case, the resist function is the protection of the underlying part of the sample from ions bombardment. Finally, the residual photoresist is removed (*lift-off* procedure) using acetone or different solutions (e.g. AZ100 remover, microchemicals-USA).

Additive process: deposition. The photoresist-covered areas are protected from the deposition of new material. After the deposition, *lift-off* procedure removes also the overlying material, leaving the deposited material only in the zones which were not protected by the resist.

3.1.2 Inverse Lithography

In order to facilitate the photoresist removal at the end of the lithographic process, openings in the newly deposited material are highly advantageous, because the remover (e.g. acetone) can more easily reach the resist layer causing its detachment from the sample. As shown in Fig.3.1(e), positive lithography brings to an uninterrupted deposited layer whereas, using a negative resist or an inverted positive resist, a suitable cracked profile favoring the resist removal is obtained. For this reason we used the second option. Fig.3.2b displays the steps of an inverse lithography process.

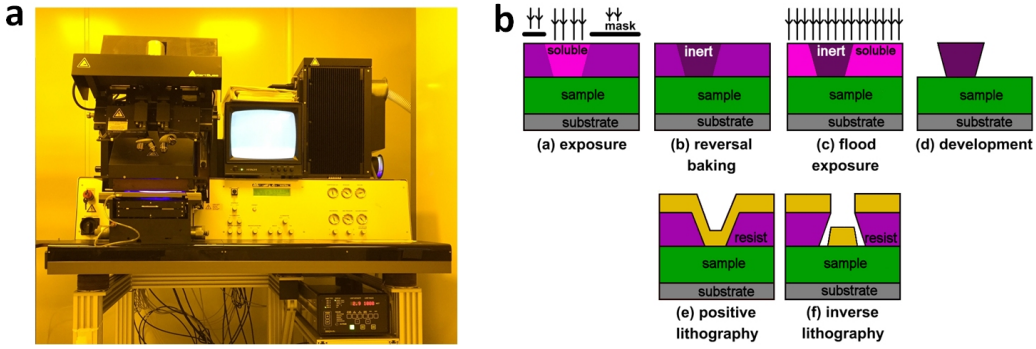

Figure 3.2: **a** Karl Suss MA6 mask aligner. **b** Inverse lithography process steps. In (e) and (f) overcut and undercut effects on the deposition, respectively. The undercut profile allows an easier photoresist removal during the *lift-off* process.

After the UV exposure (a), an extra backing, the so-called post exposure bake, is performed. Hence, the photoresist is affected by cross-linking of the polymeric chains in the exposed area. In this way, the exposed area is non-soluble and insensitive to further light exposure (b); Before the development, the sample is exposed without mask in the so-called *flood exposure* step (c). As a consequence, all the resist which was not exposed in the first step becomes soluble, whereas the rest, which is cross-linked, is non soluble (d). This procedure allows to obtain the inversion of the mask image and an *undercut* profile (d), which provides the slits required in the *lift-off*.

The additive processes performed in this thesis relies on two different deposition techniques: electron beam evaporation and magnetron sputtering (see the next sections).

3.2 Electron beam evaporation

The most widely used deposition method in this thesis work is electron beam evaporation. It allows the deposition of different metals but also dielectric

and insulating materials.
The evaporation principle is the following: in a high-vacuum chamber, a focused electron beam heats the material above the melting temperature, so as to reach a high enough vapor pressure. In this way, atoms in gaseous phase travel from a crucible, containing the material, to the sample surface where they precipitate into solid form. Atoms follow an almost linear trajectory, since in high vacuum they do not undergo collisions. In fact, the mean free path (i.e. the average distance traveled by atoms between two collisions) at a pressure lower than $5*10^{-6}$ mbar is larger than the typical length of a deposition chamber.
The evaporation process presents some limitations imposed by the photoresist: for example, the temperatures has not to exceed 200 ^{o}C in order to preserve the thermal stability of the resist. Crucibles, filled with the material to be evaporated, are made in graphite or other refractory compounds. The deposition rate, once the target-substrate distance and the material are fixed, just depends on the electron beam power.

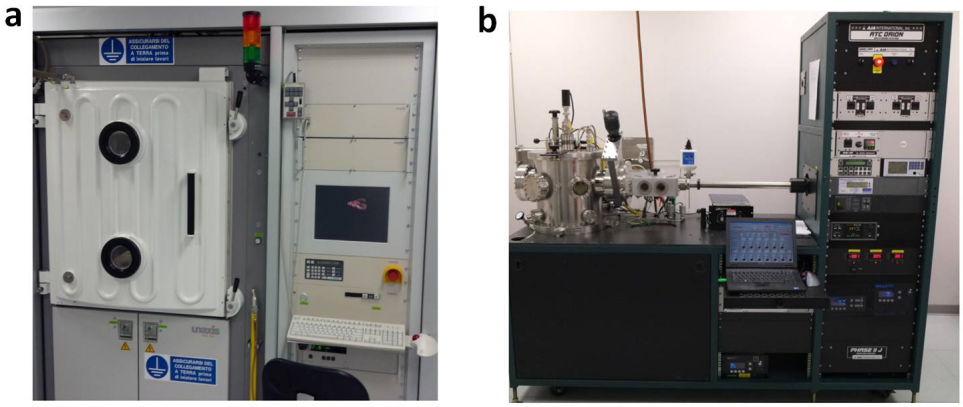

Figure 3.3: **a** *Evatec BAK 640* electron beam evaporator and **b** *AJA Orion 8* magnetron sputtering.

In *Polifab* lab, the machine employed is a *Evatec BAK 640* evaporator (see Fig.3.3a), equipped with a 6 pocket rotating crucible. The deposition rates are monitored with a quartz microbalance, which allows real-time measurement of the evaporated film thickness. Below, the parameters used for the

evaporation of different materials are listed.

Material	Base pressure	Rate	E-beam power
$Ni_{80}Fe_{20}$	$2*10^{-6}$ mbar	0.1nm/s	7% of the full scale
Fe	$2*10^{-6}$ mbar	0.2nm/s	9% of the full scale
Cr	$2*10^{-6}$ mbar	0.1nm/s	6% of the full scale
SiO_2	$2*10^{-6}$ mbar	0.3nm/s	5% of the full scale

Table 3.1: Parameters used in electron beam evaporation processes and relative deposition rates.

3.3 Magnetron sputtering

To deposit insulating layers (SiO_2 and Si_3N_4) with a better film quality compared to e-beam evaporation, magnetron sputtering is preferable. It is a physical vapor deposition method which ensures a good film adhesion to the substrate, allowing a high control on the composition, uniformity and thickness of deposited materials. Furthermore, even materials with very high melting points and low vapor pressure are easily sputtered while evaporation of these materials is problematic or impossible.
In a high vacuum chamber, first a gaseous plasma is initiated, then plasma ions are accelerated towards the material to be deposited (the so-called target), which is eroded by ions via momentum transfer. This causes the ejection of the material from a target, in the form of neutral atoms, clusters of atoms or molecules. When these particles are ejected, they essentially move following a straight path (apart from the interaction with the reactive gases in the chamber) until they come in contact with the substrate, such as a Si wafer, that is finally covered by a thin layer of the sputtered material.
To initiate the plasma, an inert gas (usually Ar) is introduced inside the high vacuum chamber and a negative bias voltage is applied to the target. Free electrons and Ar^+ ions are accelerated by the electric field and ionize by collisions with other Ar atoms, producing additional Ar^+ ions and free electrons. This is a cascade process with positive feedback that ignites the plasma. Finally, Ar^+ ions move towards the negatively biased target, hitting

the surface and thus inducing the ejection of source material and the release of more free electrons.
In magnetron sputtering, permanent magnets are placed behind the target, in order to allow the confinement of free electrons directly on top of the target surface. This provides a double advantage: first, the substrate is prevented by free-electrons bombardment, thus avoiding overheating and structural damages; second, free electrons follow circular trajectories around the lines of the magnetic field and the probability of ionizing neutral *Ar* atoms is enhanced by several orders of magnitude. The large amount of available ions significantly increases the efficiency of target erosion and, consequently, the deposition rate.
The machine used for the deposition of SiO_2 is *AJA Orion 8* system, available at Polifab. It is equipped with 10 confocal magnetron sputtering sources, which also allow for co-depositions. In order to deposit insulating thin films, a radio-frequency source is used, to prevent the formation of a charged layer on the top of the target which would affect the sputtering process.
The parameters used for SiO_2 sputtering are the following:

Material	**Deposition pressure**	**Rate**	**Power density**
SiO_2	2.2 mTorr	1.25 nm/min	9.87 W/cm^2

Table 3.2: Parameters used for SiO_2 deposition by magnetron sputtering.

3.3.1 Reactive sputtering

The deposition of Si_3N_4 is performed by reactive sputtering. With this technique, the deposited material is obtained by a chemical reaction between the atoms ejected by the target and a reactive gas (e.g. O_2 or N_2) introduced inside the vacuum chamber. The film composition is controlled by the relative pressures of inert (Ar) and reactive gases.
A customized machine (based on 3" TORUS UHV Source, Kurt J. Lesker) is used. In this system, a silicon target is eroded by Ar^+ plasma, allowing the ejection of Si atoms which interact with the reactive gas, N_2, giving rise to the deposition of a Si_xN_y compound with stoichiometry close to Si_3N_4.

The base pressure in the vacuum chamber is $\approx 10^{-6}$ Torr and the vacuum is provided by a turbomolecular pump.
Then, Ar (0.8 sccm) and N_2 (3.2 sccm) are inserted together in the deposition chamber with a gas injection system which allows to control the gases fluxes so as to obtain to the desired stoichiometry. The plasma strike and the deposition conditions are manually controlled, by acting on a gate valve, which allows to regulate the pressure inside the chamber. Si_3N_4 is deposited at 5.5 mTorr, using a radio-frequency (RF) source at 150 W. With these parameters, the deposition rate is $\approx$1 nm/min.

3.4 Etching techniques

Two subtractive processes (see Fig.3.1) are used to remove material from the areas of the sample unprotected by the resist: ion beam etching and reactive ion etching.

3.4.1 Ion Beam Etching

Ion beam etching (IBE) is a physical dry etching technique where ions (e.g. Ar^+) are accelerated towards the sample in a vacuum chamber. Similar to what happens to the sputtering targets, the material on the sample is removed by energy transfer between the accelerated ions and the sample surface.
Ions are generated from inert gas through a discharge current. A filament run by current, which is the cathode, emits electrons (by thermoionic effect). These electrons, accelerated towards the anode applying a voltage difference between the electrodes (discharge voltage), hit and ionize the atoms of the inert gas giving rise to positive ions and free electrons. These free electrons contribute to maintain the plasma, while the ions are accelerated toward the sample by a grid set at a negative potential (accelerator voltage).
In this thesis work, a modified Kenosistec VS80 system is used for Si and SiO_2 etching. The machine is equipped with a Kaufman *KDC 160* Ion Source, producing a neutralized Ar beam with 6" diameter. During the etching process, the sample holder is kept in rotation for insuring the uniformity of the

etching rate on the whole surface. Moreover, the sample holder can be tilt with respect to the incident beam to avoid the redeposition of material during the etching.
The etching rate depends on different parameters such as etching pressure (p_e), Ar^+ flux, accelerating voltage (V_A), beam current (I_B) and the composition of the materials to be etched.
The optimized parameters for Si and SiO_2 etching are listed in the following table.

Material	$\mathbf{p}_E$	**Etch Rate**	**Ar flux**	$\mathbf{V}_A$	$\mathbf{I}_B$
SiO_2	3*10^{-4} mbar	3.75 nm/min	8 sccm	200 V	50 mA
Si	3*10^{-4} mbar	4.8 nm/min	8 sccm	200 V	50 mA

Table 3.3: Parameters used in the ion beam etching processes.

3.4.2 Reactive Ion etching

Reactive ion etching (RIE) is a dry etching technique, which exploits a chemical reactive plasma to etch material from a sample upon the application of RF field. Reactive ions of different species are accelerated towards the sample, allowing to combine a physical etching (similar to IBE) with a selective erosion arising from the chemical interaction between the ions in the plasma and the surface to be etched.
In this thesis work, a *Oxford Plasmalab 100* RIE, which is an inductively coupled plasma etcher, is used according to the following working principle: the etching process occurs in a vacuum chamber provided with inlets where reactive gases enter and are ignited to create the etching plasma. This ignition is induced and maintained by radio frequency coils in the so-called *Inductively coupled system* (ICP), placed on the chamber sides; ICP operates at 2 MHz with RF power up to 2000 W. The substrate holder is also RF biased at 13.56 MHz with power (RIE power) up to 1000 W, allowing for the acceleration of positive ions towards the sample. The chuck is connected to a cooling system (set to 3^oC) to regulate the wafer temperature.
Due to the directional motion of reactive ions, RIE produces very anisotropic

etching profiles, with larger etching rates compared to IBE. For this reason, RIE is suitable for etching processes, when several micrometers of material have to be removed. RIE is also a selective method, allowing for the etching of a target material, with much smaller etching rate for the other layers in the stack. Indeed, various materials can be used as a mask to protect the area on the sample not to be etched.
Depending on the etched material, different gases can be employed. In this thesis work, RIE is performed with carbon-fluorine gases and it is used to pattern Si-molds for the fabrication of Magnetic pillars (see Chapter 5).
Two different RIE processes have been optimized to etch Si. The first one is based on a mixture two gases: SF_6 and O_2[94]. SF_6 allows for the Si etching, while O_2 works as a passivating gas required to protect the side-walls of the etched area to achieve vertical profiles[95]. The etching parameters for SF_6/O_2 process are listed in the following table:

SF_6	**O_2**	**ICP Power**	**RIE power**	**p_E**	**Etch rate**
80 sccm	20 sccm	1000 W	50 W	30 mTorr	140 nm/min

Table 3.4: Parameters used in the SF_6/O_2 RIE process.

Instead, the second one is the so-called BOSCH process where two gases are sequentially alternated inside the chamber to achieve Si-etching and side walls passivation. The gases employed in this process are SF_6 (for etching) and C_4F_8 (for passivation)[96]. Due to the time ($\approx$ 5 s) required to pump-away the reactive species inside the chamber, when the gas injection of one of the two gases is turned-off, intermediate pumping steps are added to avoid mixture of SF_6 and C_4F_8 in the vacuum chamber that can negatively affect the etching profiles and rate. A summary of the steps and parameters involved in a single BOSCH-like cycle is listed in table 3.5.
Note that, this sequence has to be repeated n-times depending on the target etching thickness. This second process allows for a higher etching rate to 250 nm/min (165 nm/cycle), despite an increasing complexity of the parameters to be optimized. Vertical and anisotropic etching profiles are obtained using both the two processes.
Typically, hard masks are used to protect the non-etched zones, made of Cr

Step	Gas	ICP Power	RIE power	p_E	time
Etch	SF_6 80 sccm	1000 W	50 W	10 mTorr	10 s
Pump 1	no	0 W	0 W	0 mTorr	10 s
Passivation	C_4F_8 12 sccm	1000 W	50 W	10 mTorr	10 s
Pump 2	no	0 W	0 W	0 mTorr	10 s

Table 3.5: Parameters used in a single cycle of a RIE-BOSCH process.

(20 nm), deposited by e-beam evaporation after patterning by optical lithography. At the end of the RIE process, Cr is chemically removed from the *Si*-molds by Chromium-etchant (provided by *sigma Aldrich*).

3.5 PDMS preparation

Magnetic pillars (see Chapter 5) and microfluidic channels on DWTs devices (see Chapter 4) are made in Polydimethilsiloxane (PDMS). It is a flexible and transparent polymer completely biocompatible. PDMS is prepared using the *Sylgard 184 Silicone Elastomer Kit*, according to the following protocol:

- The elastomer and its curing agent are mixed in a ratio of 10:1 for 2 minutes.
- The mixture is placed in a vacuum chamber to remove the bubbles arising from the mixing.
- The compound is then carefully poured on the mold. The formation of new bubbles has to be avoided, as they would otherwise produce defects in the solidified sample.
- The PDMS is heated for 2 hours at 85^{o}C.
- Once the PDMS is cured and cooled at room temperature, it is peeled-out from the mold.

After the "peeling" procedure, microfluidic channels described in section 4.3.2 are bonded on the top of DWTs chips, using an oxigen plasma in a Plasma

Asher Machine (*PVA TEPLA200*). In such machinery, the RF plasma allows to assist and control surface chemical reactions, making both PDMS and chip surfaces hydrophilic. The two samples are inserted in the vacuum chamber and exposed to O_2 plasma at 1 mbar and 60 W for 1 min. After this treatment, PDMS is directly placed in contact with the chip surface allowing for the bonding. This process has to be performed within 1 min, since the surface modification is temporary. Additionally, the entire device is heated at 85^{o}C for 30 min in order to increase the bond strength.

3.6 Vibrating sample magnetometry

Magnetic properties of the magnetic devices developed in this thesis work are characterized by Vibrating Sample Magnetometry (VSM), which measures the magnetic moment of a sample exposed to a uniform magnetizing field[97]. The sample is placed between two poles of an electromagnet and a pair of pick-up coils (see Fig.3.4), on a sample holder that vibrate transversely thanks to an electromechanical actuator.
This measurement relies on Faraday's law of induction; VSM detects the voltage induced in the detection coils by the time-varying magnetic flux, created by the stray field originating from the vibrating sample:

$$\nabla \times \mathbf{E} = -\frac{\partial \mathbf{B}}{dt} \tag{3.1}$$

where $\mathbf{E}$ and $\mathbf{B}$ are respectively the electric field and the magnetic flux density. When a magnetic material is exposed to the homogeneous field $\mathbf{H}_0$ generated by the magnetic poles, it is magnetized with a certain value of $\mathbf{M}$ and the magnetic flux density near the sample is $\mathbf{B} = \mu_0(\mathbf{H}_0 + \mathbf{M})$. Applying a constant magnetic field $\mathbf{H}_0$, Faraday's law can be written as:

$$\nabla \times \mathbf{E} = -\mu_0 \frac{\partial \mathbf{M}}{\partial t} \tag{3.2}$$

It results in an electromotive force (U_{em}), generated in the pick-up coils, proportional to the magnetization of the sample and depending on the relative orientation between the magnetic moment and the coils:

$$U_{em} = \oint \mathbf{E} \cdot d\mathbf{l} = \int\int_S -\mu_0 \frac{\partial \mathbf{M}}{\partial t} \cdot d\mathbf{s} \tag{3.3}$$

where $d\mathbf{s} = \mathbf{n}ds$ and n is the normal to the surface S. In this way, the magnetic moment of the sample along the field direction is measured, as it is proportional to the induced current. A transimpedance and a lock-in amplifier are employed for the amplification of the signal and the reduction of the electrical noise.

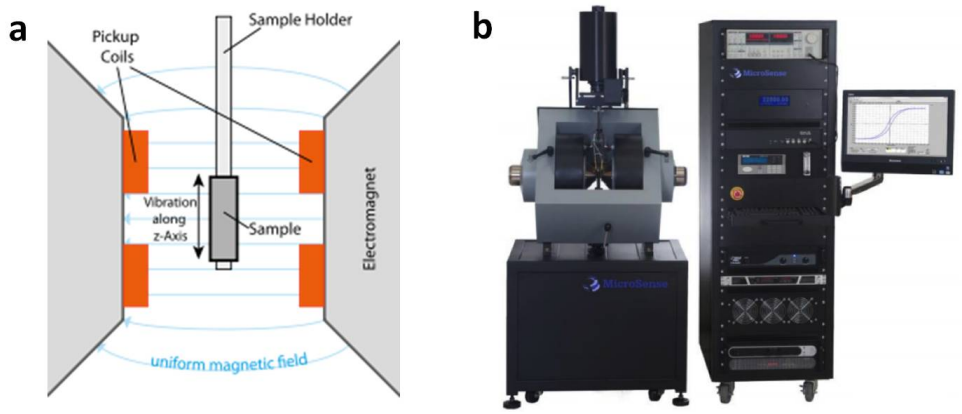

Figure 3.4: **a** Sketch of the Vibrating Sample Magnetometer working principle. **b** Microsense EZ9 Vibrating Sample Magnetometer available at *Polifab*.

A measurement of a magnetic sample consists of the following steps:

- Sample vibration is turned on.
- The VSM software sets a constant magnitude of the uniform magnetic field applied by the poles.
- The signal measured from the probe is averaged and translated into a value for the magnetic moment of the sample.
- The software sets a new constant magnetic field value.
- Measurements are repeated for different values of **H** and **M**vs**H** is plotted.

In this thesis work, the VSM Microsense EZ9 (see Fig.3.4b) is used. It measures magnetic moments down to 1 μemu and is employed for studying the magnetic properties of bulk samples, thin films, liquids or powders. It allows

measurements as a function of magnetic field, temperature, currents and electric fields and it is possible to perform automated complex preparation sequences (e.g. magnetic field cooling for spintronic devices based on antiferromagnets). A magnetic field up to 2.25 T can be applied and automatic sample rotation is also provided. The magnetometer is fully controlled by a dedicated software.

3.7 Experimental setups

In this section, the setups used for the biological experiments described in Chapter 4 and 5 are presented. The first one allows for the manipulation of magnetic micro- and nanoparticles by DWTs in a cell culture environment, while the second is used for actuating magnetic pillars during the biological studies.

3.7.1 Setup for magnetic DWTs experiments

The experimental setup for the experiments with DWTs performed at IFOM is illustrated in Fig.3.5.
The particles manipulation and the effects of the mechanical stimulation on cells are monitored under a Leica TCS SP5 confocal laser scanning microscope. It is based on an upright DM6000CFS microscope and equipped with a HCX Apo L20x/1.0 NA W water immersion objective.
The DWTs chip with the cells cultured on top is placed on a Petri dish, located in a custom microscope chamber (see Fig.3.5) to maintain the temperature at 37 ^{o}C and wet atmosphere. A PID thermostat, connected to a thermo-couple, is employed to monitor the temperature, while a warm air flux, with controlled temperature and humidity, allows for the chamber conditioning.
The external magnetic field needed to manipulate the magnetic particles is applied using two Neodymium Iron Boron ($Nd_2Fe_{14}B$) permanent magnets underneath the microscope stage. The field direction is set by a stepper motor which allows the fine control of magnets rotation (see Fig.3.5), thus producing a uniform magnetic field mainly parallel to the chip surface, with

a maximum absolute value of 50 mT. This field is applied simultaneously on the entire chip. The stepper motors are powered through proper drivers and they are controlled by an Arduino-uno microcontroller. Arduino can be easily interfaced with a labview software to achieve an efficient and remote control of the whole system.

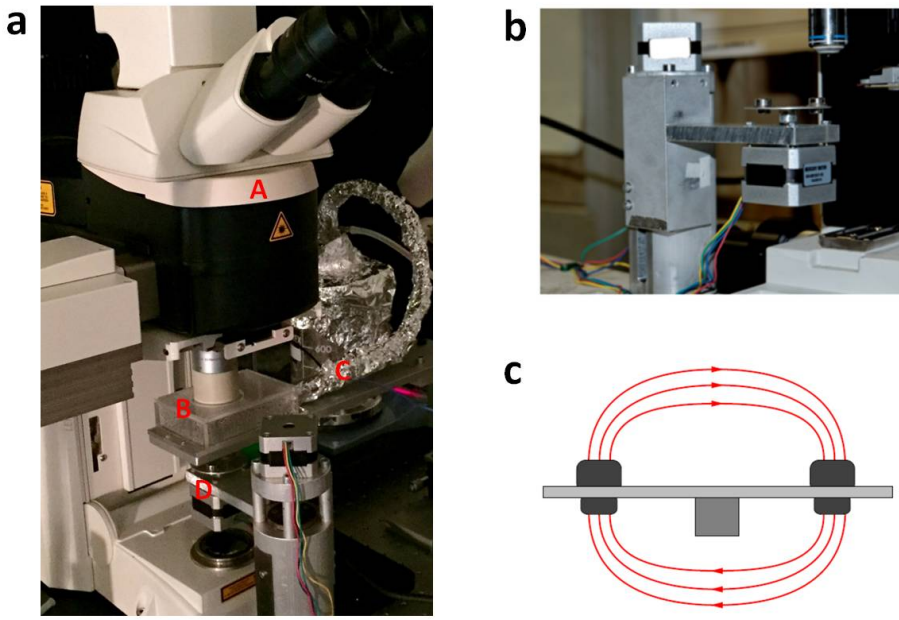

Figure 3.5: **a** Setup for DWTs experiments, showing the fluorescence microscope (A), the custom microscope chamber (B), the air flux system to preserve temperature and humidity (C) and two permanent magnets controlled by a stepper motor to provide the external magnetic field (D). **b** Stepper motor system which allows to control the magnetic field rotation. **c** Sketch of the magnetic field lines of force from the permanent magnets.

For the experimental evaluation of the magnetic forces exerted by DWTs (see section 4.3.2), a fine regulation of the magnetic field is required. To this scope a four-pole electromagnet is used to apply a uniform field up to 50 mT in the sample plane. The experiment is monitored via an optical microscope (*Nikon ECLIPSE*) equipped with a 60x immersion objective and an EMCCD camera (see Fig.4.4).

3.7.2 Setup for Magnetic pillars experiments

Experiments on magnetic pillars are performed with the setup illustrated in Fig.3.6.

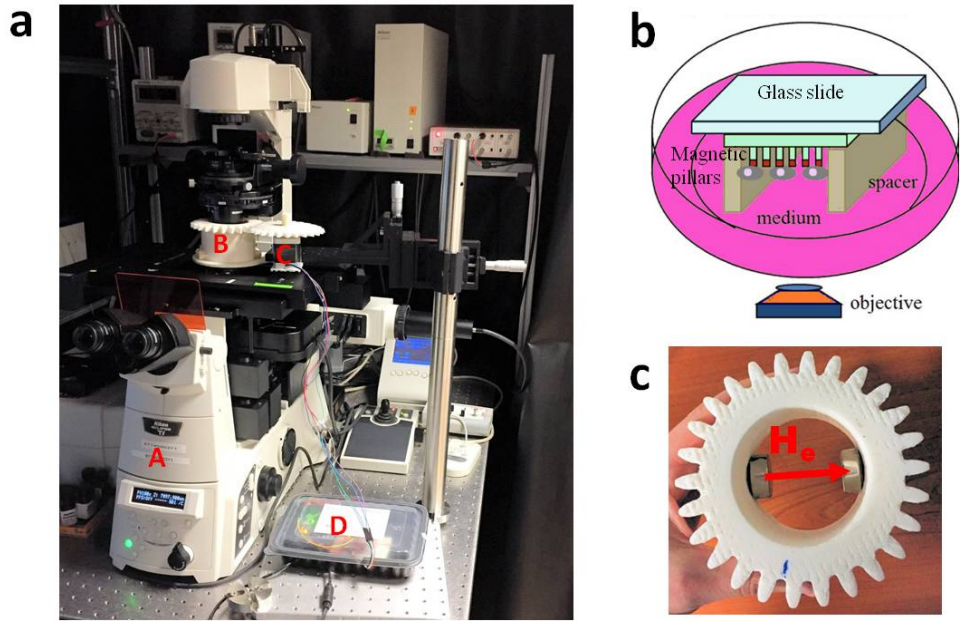

Figure 3.6: **a** Setup for magnetic pillars experiments showing the fluorescence microscope (A), the 3D-printed holder for the permanent magnets, a stepper motor (C) for allowing the field rotation, controlled by an Arduino-UNO (D) microcontroller. **b** Petri dish containing the device and the cultured cells; the chip is turned upside-down on two spacers for performing imaging with an inverted microscope. **c** Magnets holder which allows the application of a rotating magnetic field.

Before imaging, the chip is inverted in a Petri dish, on two *parafilm* spacers to avoid contact between the plated cells and the bottom of the dish. It allows cell imaging on an inverted confocal microscope. A CO_2 free medium (Gibco; Life Technologies) is also used during the experiments to prevent changes in pH that could negatively affect the biological responses. The dish is then placed under a NikonA1R Confocal microscope, equipped with 20x and 40x objectives.

The external magnetic field for magnetic pillars actuation is applied with two permanents magnets in $Nd_2Fe_{14}B$ which exert a quasi uniform field of 50 mT over the chip; magnets are placed on a rotating 3D-printed support (see Fig.3.6b), isolated both from the microscope and the sample stage, to prevent de-focusing or vibration on the device. The Magnetic field rotation is provided by a stepper motor, powered through proper drivers, and controlled by an *Arduino-UNO* microcontroller.
For the characterization of pillars deflection (see Chapter 5), a fine regulation of the magnetic field is required. At this purpose, a custom two-poles electromagnet is exploited to apply a uniform magnetic field up to 150 mT and confined along the sample plane. The experiment is monitored under an optical microscope (*Nikon ECLIPSE*) equipped with a 60x immersion objective and an EMCCD camera.

Chapter 4

Magnetic domain wall tweezers

Micromanipulation techniques based on the controlled and localized motion of micro and nanoparticles at the cellular and subcellular scale, are becoming fundamental tools for testing the mechanical properties of cells and cell subcompartments. In this context, magnetic manipulators[98],[99],[100] are very appealing because they are suitable to operate in any biological environment and they are non-invasive for cells and biomolecules, as the local energy dissipation is negligible if low frequency magnetic fields are applied. This chapter presents a platform based on magnetic Domain Wall tweezers (DWTs), suitable for mechanobiology studies. DWs propagating in ferromagnetic rings are exploited to finely manipulate superparamagnetic beads in a cellular environment. The particles are pushed against the cellular membrane of HeLa cells cultured on-chip, thus exerting highly localized and controllable forces, properly quantified either by simulations and experiments. Local deformations of the HeLa cell membrane are observed and measured via confocal microscopy. The forces exerted by DWTs, which produce cell indentations, are fully coherent with an elastic model of the cell membrane. Finally, it is shown that DWTs allow for the the manipulation of magnetic nanoparticles microinjected inside the HeLa cell cytoplasm. The biological validation of this technique was performed in collaboration with *IFOM* center, while the elastic model of the cell membrane was developed in collaboration with Prof. P. Ciarletta, from the *Dipartimento di Matematica* at *Politecnico di Milano*. These results have been published in *Lab-on-a-*

chip[101] and *Journal of Applied physics*[102] journals[1].

4.1 Review of the literature

Manipulation of magnetic particles has found a large amount of applications in the biomedical field, ranging from magnetic separation[103], drug delivery[104], cell microrheology[105] and mechanobiology[106]. A large variety of non-toxic magnetic beads is available nowadays, suited for studies on living cells[107]. In this context, magnetic tweezers allow the control of magnetic beads and particles motion thanks to the application of magnetic fields or field gradients. In order to confine the magnetic field to achieve efficient particles manipulation, different strategies can be adopted. One of the most widespread method is represented by micrometric tip coils[64][108]. They allow to exert forces on particles previously trapped on a surface, but are not suitable for manipulation and displacement over large distances. Moreover, the actuation is restricted to a single particle or a cluster of particles in close proximity to the tip coil, preventing parallelization. Furthermore, the presence of the tip introduces additional issues for the optical monitoring of biological properties. Despite these limitations, such magnetic tweezers are still one of the most widespread methods in biology as intense, tunable and localized magnetic forces can be applied[25]. To achieve a more reliable trapping and manipulation of particles, different on-chip technology has been developed in the last decade[87],[109]. Most of them relies on current lines[82],[110] properly patterned on a substrate, where controlled currents produce confined magnetic fields allowing for particles manipulation. However, the application of intense forces is limited to few pN[111], as large currents can create overheating with a consequent cell damage.
To overcome these limitations, micromanipulators based on the combination

[1]Sections of this chapter including figures and text have been previously published in the following articles: *M. Monticelli et al.* "Magnetic domain wall tweezers: a new tool for mechanobiology studies on individual target cells", *Lab on a chip*, 2016, 7, 16, pp 2882-90 and *M. Monticelli et al.* "Towards an on-chip platform for controlled forces application via magnetic particles: a novel device for mechanobiology", *Journal of Applied Physics*, 2015, 117, 17B317. Reproduced with permission.

of uniform magnetic fields with ferromagnetic micro- or nanostructures patterned on-chip have been developed. They produce confined stray field gradients allowing for trapping and manipulating superparamagnetic particles with micrometric spatial resolution[65],[112]. A further improvement can be obtained using Domain walls manipulators[66],[89],[68], which exploits magnetic DWs nucleated in properly designed ferromagnetic conduits to trap and manipulate particles with higher resolution (down to 100 nm) and applying forces up to hundreds pN[66]. This technique was first developed by *NaBis* group in 2009 [88], in cooperation with P. Vavassori from CIC-Nanogune (Donostia-Spain), and relevant implementations have been performed afterwards, as the demonstration of the possibility to simultaneously detect and manipulate particles on the same magnetic conduit[113] and manipulating a batch of particles all over a two dimensional space[114]. Concerning the biological applications, the possibility of handling particles coated with proteins has been shown[66]. Furthermore, suspensions of yeast cells decorated with magnetic beads have been trapped and manipulated[67].
In this chapter, I report on the first demonstration of particles manipulation by DWTs in a cell culture environment, leading to the application of controllable forces of several hundreds pN on the membrane of a HeLa cell cultured on-chip (see Fig.4.1a).
A versatile and non-invasive on-chip technology for mechanobiology studies on single cells has been developed. Noteworthy, it is fully compatible with real-time optical monitoring of the cell activity upon quantitative and localized mechanical stimulation.

4.2 Device fabrication

DWTs platform developed in this work is based on magnetic rings (see Fig.4.1b) made of Permalloy ($Ni_{80}Fe_{20}$). They are 2 μm wide, have a radius of 10 μm and are 40 nm or 150 nm thick. Reversed image optical lithography with AZ5214E resist is performed on a Si or SiO_2 substrate (1.5 x 1.5 cm^2) in order to pattern the ring-shaped structure. Then, ion beam etching is used to etch the substrate in the rings, thus obtaining planar samples after $Ni_{80}Fe_{20}$ deposition in the etched ring-shaped structures. E-beam evaporation and

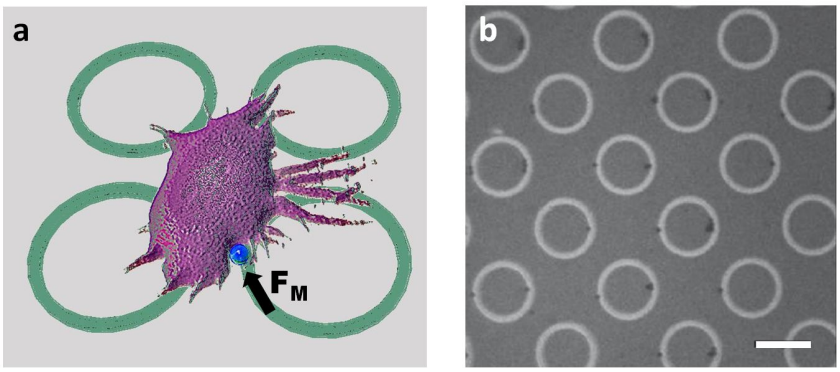

Figure 4.1: **a** Sketch of a zoomed-in view of the chip surface illustrates the device working principle: a superparamagnetic bead (blue) bound to a magnetic DW in the conduit exerts a magnetic force ($\mathbf{F_m}$) on the cell membrane of a HeLa cell cultured on the chip surface. **b** Optical microscopy images of rings ferromagnetic Permalloy conduits with 1 μm particles attracted by DWs. Scale bar: 20 μm.

the subsequent lift-off allow us to finally obtain 150 nm thick $Ni_{80}Fe_{20}$ rings. The magnetic conduits are then uniformly covered by a capping layer made of Si_3N_4 (50 nm) and SiO2 (50 nm), in order to ensure biocompatibility and protect them from damage due to contact with the cell culture medium. Si_3N_4 films are grown by reactive RF magnetron sputtering, while SiO_2 is grown by RF magnetron sputtering under pure Ar pressure.
To perform an experimental evaluation of the magnetic force (see section 4.3.2), some of the DWTs devices are equipped with a PDMS microfluidic channel, fabricated by soft-lithography from a SU-8 mold and sealed on top of the chip. The channel, bonded on the chip by means of an O_2 plasma treatment, is 2 cm long, 450 μm wide, and 32.5 μm thick.

4.3 Evaluation of magnetic force exerted by DWTs

In order to employ DWTs technology for exerting controlled mechanical stimuli on target cells, a quantification of the applied forces is required. First, the

magnetic force acting on superparamagnetic particles is simulated. We show that, considering all the forces experimented by each bead, the mechanical stimulus applied to cells is essentially given by to the magnetic force, as the other contributions are negligible. Finally, an experimental method to evaluate the magnetic force exerted by DWs is presented, to demonstrate that simulated forces are coherent with real values.

4.3.1 Simulations

Simulations to quantify the magnetic force applied by the domain wall magnetic tweezers are performed using OOMMF (Object Oriented Micro Magnetic Framework)[115]. The micromagnetic configuration of the rings and the related magnetic stray field are calculated using the following parameters for $Ni_{80}Fe_{20}$: saturation magnetization M_s = 680 x 10^3 A·m^{-1}, exchange stiffness A = 1.3 x 10^{-11} J·m^{-1}, damping coefficient τ = 0.01 and null magneto-crystalline anisotropy. A 25 x 25 x 20 nm^3 unit cell has been used for simulating the micromagnetic configuration of the rings. Although the exchange length of Permalloy is 5.2 nm, this represents a reasonable compromise ensuring reduced computational times. As a matter of fact, we checked that, using a cubic unit cells with a side length of 5 nm, not major modifications are introduced in the simulated stray field. The magnetic force is calculated from the stray field produced by the DW in the conduit, according to the following equation (see section 2.3.3):

$$\mathbf{F_M} = \frac{\mu_0}{2} \int_V [(\mathbf{M} \cdot \mathbf{H}) - \mathbf{H^2}(\mathbf{M}/\mathbf{H})] dV \tag{4.1}$$

where $\mathbf{M}$ is the magnetization of the superparamagnetic bead and $\mathbf{H}$ is the total field ($\mathbf{H} = \mathbf{H_d} + \mathbf{H_e}$), calculated using OOMMF, the sum of the stray field generated by the ferromagnetic conduit ($\mathbf{H_d}$) and the external magnetic field ($\mathbf{H_e}$).

The integration is performed numerically (with software *Matlab*) over the whole bead volume (V). To improve the reliability of the force estimate, we used the Langevin expression for the magnetic susceptibility, so that the local magnetization within the bead is given by:

$$M(H) = M_S \left(coth\left(\frac{3\chi_0 \cdot H}{M_S} \right) - \frac{M_S}{3\chi_0 \cdot H} \right) \tag{4.2}$$

where M_S is the saturation magnetization and χ_0 is the linear magnetic susceptibility coefficient describing the linear dependence between **M** and **H** for small values of **H**.

As discussed in Ref.[69],[67], two opposite Neel DWs are nucleated in the ring, thus producing a magnetic stray field ($\mathbf{H}_d$) whose gradient allows the attraction and manipulation of particles in suspension, upon the application of $\mathbf{H}_e$. The magnetic configuration of a portion of the ring has been simulated and it is shown in Fig.4.2a, for $\mathbf{H_e}$ = 30 mT applied along the x-direction.

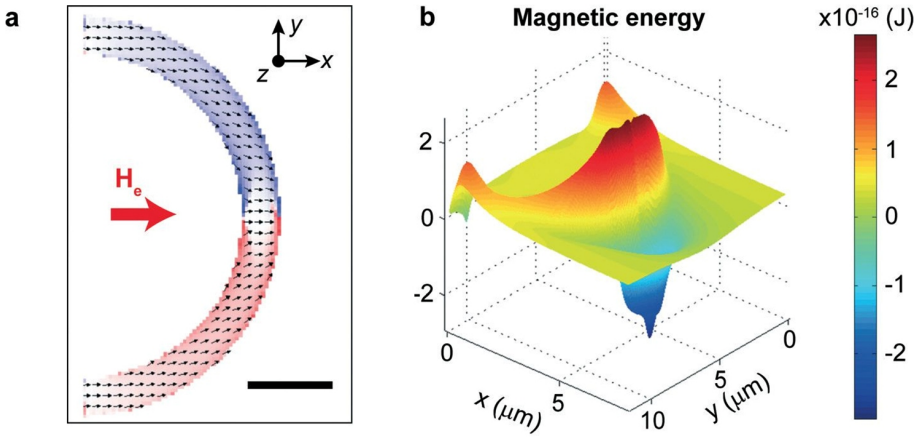

Figure 4.2: **a** Micromagnetic configuration (simulated using OOMMF) of a portion of the nanometric ring ($Ni_{80}Fe_{20}$ thickness = 150 nm), where a transverse DW is nucleated by applying an external magnetic field ($\mathbf{H}_e$) of 30 mT directed along the x-axis. The arrows represent the local magnetization direction, while the red-white-blue scale refers to the y-component of the magnetization. Scale bar: 5 μm. **b** Magnetic energy well of a superparamagnetic bead (1 μm diameter, $\chi_0 = 1.46$, $M_s = 35$ x 10^3 A·m^{-1}) attracted by the DW 100 nm above the ring-shaped nano-conduit (150 nm $Ni_{80}Fe_{20}$ thickness), when an external magnetic field of 30 mT is applied.

The arrows represent the orientation of **M** in the magnetic conduit, showing that the DW magnetization is locally perpendicular to the ring in the region of the DW. The associated magnetic charges produce a confined stray field $\mathbf{H}_d$ which traps superparamagnetic beads in suspension. This fact can be clearly

seen in Fig.4.2b, where the simulated magnetic energy ($U_m = -\mu_0(\mathbf{m} \cdot \mathbf{H})$) of a 1 μm bead is shown as a function of the position in the xy-plane. Here, the bottom of the particle is placed at a distance of 100 nm from the magnetic structure top surface, corresponding to the capping layer thickness. The potential well minimum is located above the DW, slightly displaced to the outer edge of the conduit[113]. Noteworthy, by rotating $\mathbf{H}_e$ around the chip plane, the Neel DW is moved along the ring in a continuous way, thus allowing the manipulation of the particles attracted above the nanostructures.
The total mechanical force exerted on a particle is evaluated. It is essentially given by the magnetic force $\mathbf{F}_m$ on the beads, calculated according to Eq.4.1, as the latter is much higher than the other contributions acting on the magnetic beads: viscous friction, gravity, buoyancy and Brownian motion.
The viscous friction on particles in a fluid is described by the Stokes equation (see Eq.4.4). For a typical manipulation velocity $v = 10$ μm·s^{-1}[69], it is equal to 85 fN and can be neglected if compared to $\mathbf{F}_M$, which is in the order of hundreds of pN[67],[89]. Even the gravity and buoyancy forces are much less intense ($\approx$10 fN) than $\mathbf{F}_m$. Finally, the Brownian motion plays a negligible role when beads are trapped by DWTs because the thermal energy ($k_{BT} = 4.14$ x 10^{-21} J) is much lower than the depth of energy well ($U_m = 10^{-16}$ J, see Fig.4.2b)[113].
Fig.4.3a and Fig.4.3b display the simulated magnetic force maps on the x-y plane, for the radial ($\mathbf{F}_r$, Fig.4.3a) and tangential ($\mathbf{F}_t$, Fig.4.3b) components with respect to the magnetic ring, when a horizontal $\mathbf{H}_e = 30$ mT is applied.
The maximum values of the radial and tangential magnetic forces are respectively $\mathbf{F}_{rMAX} = 625$ pN and $\mathbf{F}_{tMAX} = 215$ pN. $\mathbf{F}_{rMAX}$ is higher than $\mathbf{F}_{tMAX}$ but the radial component is less confined than the tangential one, due to the peculiar micromagnetic configuration of the DW. The out-of-plane component of the force is even larger, up to 1 nN, but it is not shown because here we focus on the manipulation of beads at the chip surface, so as to exert mainly in-plane forces to cells cultured on the chip. Note that, the reported simulated forces are relative to a $Ni_{80}Fe_{20}$ rings thickness of 150 nm, the one used in the devices for cell stimulation (see section 4.4). Crucial for applications, the magnetic force can be tuned by varying the intensity of $\mathbf{H}_e$ (see

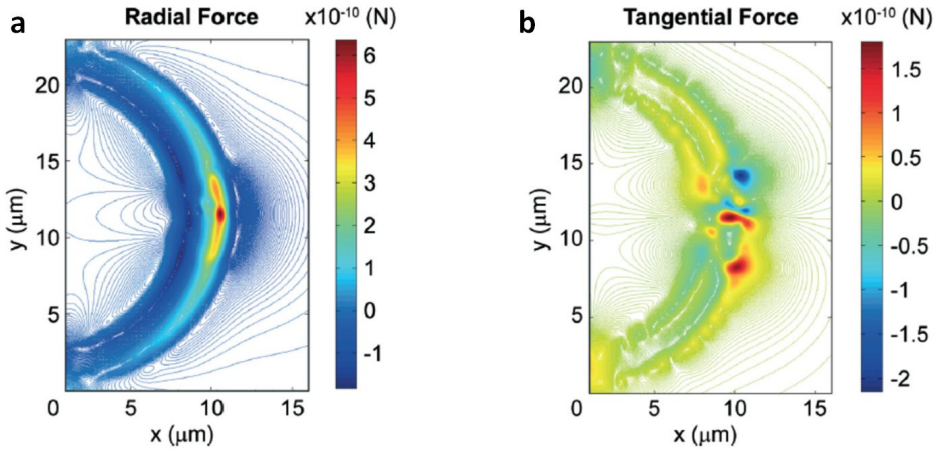

Figure 4.3: **a** Contour plot of the simulated radial component of the magnetic force in the xy plane, exerted on a 1 μm magnetic bead with the bottom surface located 100 nm above the nanostructure. **b** Same as in **a**, for the force tangent to the ring ($Ni_{80}Fe_{20}$ thickness = 150 nm).

Section 4.3.2), which affects the bead magnetization and consequently $\mathbf{F}_m$ (see the first term in Eq.4.1).
Moreover, varying the bead concentration in solution, it is also possible to promote the formation of bead clusters to increase the intensity of the applied mechanical stimuli (see section 4.4.4). At this purpouse, a physical model including the dipolar interaction between beads is developed. As a matter of fact, the magnetization of each bead is affected by $\mathbf{H}_e$, $\mathbf{H}_d$ and also by the magnetic stray field from the other particles in the cluster. In this way, the total field seen by each particle can be written as follows:

$$\mathbf{H_i} = \mathbf{H_e} + \mathbf{H_d} + \sum_{j \neq i} \frac{1}{4\pi} \left(\frac{3 r_{ij} (\mathbf{m_j} \cdot r_{ij})}{r_{ij}^5} - \frac{\mathbf{m_j}}{r_{ij}^3} \right) \tag{4.3}$$

where $\mathbf{m}_j$ is the magnetic moment of the j-th particle in the cluster and r_{ij} is the distance between the geometrical centres of beads i and j. The dipolar field is considered uniform all over the bead volume of i and, due to the fact that each $\mathbf{m}_i(\mathbf{H}_i)$ depends on magnetization ($\mathbf{m}_j$), an iterative method to calculate the equilibrium magnetic configuration of the cluster has been developed. The $\mathbf{H}_i$ field and the magnetic moment of each particle are thus

evaluated in a self-consistent way. Finally, the total force is calculated by integrating Eq.4.1 over the whole cluster, with **M** and **H** given by Eq.4.2 and Eq.4.3, respectively.

4.3.2 Experimental evaluation of the magnetic force

Before showing the results concerning the application of mechanical stimuli on cells membrane, an experimental method to evaluate the magnetic force exerted by DWTs is presented, to demonstrate the coherency with the simulated values. It relies on the comparison between the hydrodynamic and the magnetic forces exerted on a bead trapped by DWTs in a microfluidic channel.

To test the device, commercial *MyOne*-Dynabeads, (Invitrogen, 1 μm diameter, magnetization of saturation M_S = 35 x 10^3 A·m^{-1} and magnetic susceptibility in the linear range χ_0 = 1.46) superparamagnetic particles, functionalized with a carboxylic group ($COOH^-$) are used. They are diluted in a H_2O environment (η=0.89 x 10^{-3}Pa·s) to reach a final concentration of 1 μg/ml. The external field is provided by a four-pole electromagnet able to apply a uniform field up to 50 mT along the sample plane. The experiment is monitored under an optical microscope (*Nikon ECLIPSE*) equipped with a 60x immersion objective and an EMCCD camera (see Fig.4.4a). In order

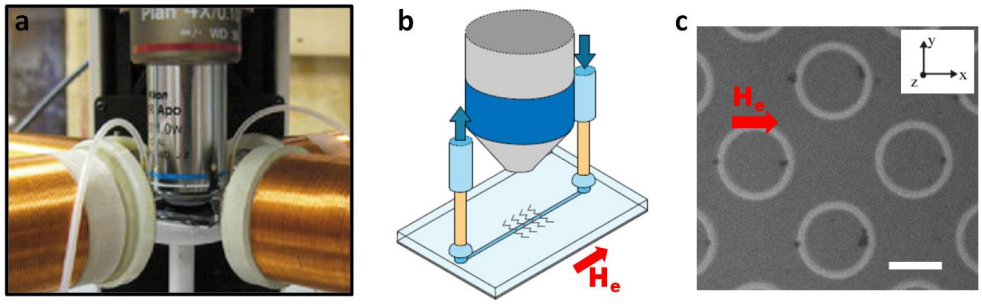

Figure 4.4: **a** Image of the measurement setup for force analysis. **b** Sketch of the chip equipped with a microfluidic channel, when $\mathbf{H}_e$ along the channel direction is applied. **c** Optical image of the device showing 1 μ beads trapped by DWs, when an external field $\mathbf{H}_e$ is applied. Scale bar: 20 μm.

to control the flow of the liquid inside the channel and its velocity, a syringe pump system is employed.

During the experiments, first, magnetic particles are conveyed in the microfluidic cell and trapped by the magnetic stray field arising from the $Ni_{80}Fe_{20}$ structures when an external field is applied in the channel direction (see Fig.4.4b,c). Then, the fluid velocity is set by the syringe pump. When the dragging force exerted on the beads by the liquid is higher than the maximum of magnetic force component along the channel direction (x-component, see Fig.4.4c), all the beads are flushed away from the top of the structures. In this way, the x-component of $\mathbf{F}_M$ is estimated by measuring the minimum hydrodynamic force exerted by the liquid on the particles causing their detachment from the conduit. This dragging force is described by the Stokes equation:

$$\mathbf{F}_D = 6\lambda\pi\eta r k\mathbf{v} \tag{4.4}$$

where v is the average fluid velocity in the channel, η the medium viscosity, and r the bead radius. k is a parameter which depends on the velocity profile of the fluid. λ is a correction coefficient which takes into account the vicinity of the wall[116] (see section 2.4.2). As a matter of fact, for a given fluid velocity, a higher dragging force is experimented by beads trapped in proximity to the surface compared to the case in which they are positioned in the middle of the channel. According to Eq. 2.26, λ is approximately equal to 3 when beads are in contact with the chip surface.

The x-component of the magnetic force exerted by magnetic tweezers on 1 μm beads, like those used in this experiment for the quantification of the forces, is simulated according to the procedure described in the previous section (see Fig.4.2 and Fig.4.3). For the magnetic rings used in the experiments (with a $Ni_{80}Fe_{20}$ thickness of 40 nm), the force is calculated as function of $\mathbf{H}_e$ from 5 to 40 mT (see Fig.4.5c 'Simulations'). The maximum value of simulated $\mathbf{F}_x$ ranges from 118 to 503 pN. As expected, $\mathbf{F}_M$ can be tuned modulating the external magnetic field.

To demonstrate that the simulated magnetic forces are consistent with the real forces exerted by DWTs, we measured the minimum flow rate of the liquid (precisely set by the syringe pump) which caused detachment of all the beads, when $\mathbf{F}_D$ counterbalances $\mathbf{F}_M$.

The experiments are carried out sweeping the liquid flow rate from 40 to 300 μl/min. In these conditions, a threshold flow rate for which all the beads are flushed away can be measured with an error of 5 μl/min. This provides a quantification of the maximum magnetic force exerted along the x-direction. Note that, isolate detaching events occur also for lower values of the flux due to Brownian motion and fabrication defects, but these are related to the statistical nature of the phenomenon and are not statistically meaningful.
Starting From the experimental evaluation of the detaching flow rate, the average velocity of the fluid in the channel is v=ϕ/A (ϕ is the flux, A the section area of the microfluidic channel) and the force experimented by beads can be calculated using the Stokes equation (Eq.4.4), considering the fluid velocity profiles inside the channel reported in Fig.4.5a and 4.5b.

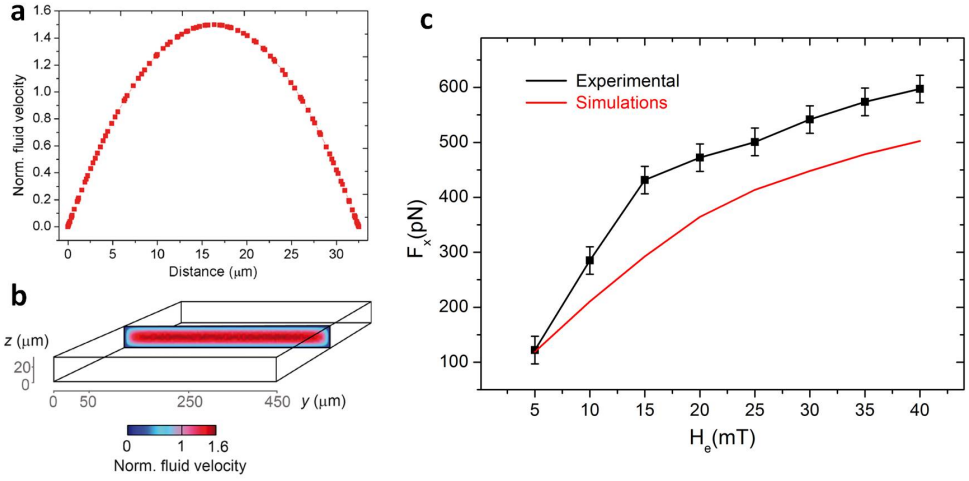

Figure 4.5: **a** Velocity of the fluid in the microfluidic channel, as function of the distance from the chip surface, normalized to the average fluid velocity. **b** Sketch of the velocity profile within the channel. **c** Magnetic force along the x-direction (along the channel) in ring shaped structures, simulated by OOMMF (red-line) and evaluated from experiments (black-line) as a function of the external magnetic field.

It is worth noting that the liquid velocity, in the laminar regime, presents a maximum in the middle of the channel and decreases to zero close to the

channel boundaries (see the normalized velocity as a function of the distance from the chip surface, Fig.4.5a, and the velocity profile in the channel section, Fig.4.5b). Therefore, considering only the velocity profile, the hydrodynamic force experimented by the bead trapped on the chip surface is lower compared to the hydrodynamic force exerted in the middle of the channel. This effect is partially compensated by the wall effect, which is included in Eq.4.4 through the λ coefficient[116]. The value of the force is calculated from the velocity profile, after integration over the bead surface, placed at 100 nm from the channel bottom (to take into account the capping layer thickness). According to the velocity profile, it is also possible to write the dragging force directly from the Stokes equation with k=0.085. This parameter does not depend on the average velocity of the fluid in the microfluidic cell, but only on the channel geometry. The detaching force along the x-direction $\mathbf{F}_x$ is calculated for different values of the external magnetic field ranging from 5 mT to 40 mT. A detaching flow rate ranging from 45 to 230 μl/min is measured, corresponding to forces from 120$\pm$25 pN to 595$\pm$25pN, as illustrated in Fig.4.5c. The experimental uncertainty in the force estimation is ascribed to the error in the detaching flow rate measurements and to some non-idealities in the channel geometry due to fabrication imperfections. It is worth to notice that the values of the forces found experimentally are in good agreement with the simulations. The discrepancy between the experimental and theoretical results can be explained by considering that chemical non-specific interactions between particles and surface occur, leading to a detaching flow slightly larger than the one required to overcome the magnetic force acting on the particles. Moreover, an additional error is introduced by approximations in the model employed for evaluating λ and k.

Apart from that, the experimental results illustrated in Fig.4.5c confirms the simulation finding, i.e., that it is possible to finely tune the magnetic force varying the value of $\mathbf{H}_e$, together with a nice agreement between the absolute values of simulation and experiment. Finally, note that this experimental analysis and the relative values of the simulated forces are carried out for $Ni_{80}Fe_{20}$ rings with a thickness of 40 nm, while during the biological experiments thicker rings are used (150 nm), in order to increase the force applied on cells.

4.4 DWTs for cell membrane stimulation

After the calculation of the forces and the experimental confirmation that such forces can be tuned with $\mathbf{H}_e$, the platform has been used for the application of mechanical stimuli on HeLa cells cultured on chip. First, the description of the experimental procedure and cell culture protocol are provided, then the results concerning the study of cell membrane deformation are presented.

4.4.1 Experimental procedure

Superparamagnetic beads are trapped and manipulated over ring-shaped ferromagnetic conduits in order to make them interact with cells cultured on-chip, exerting a magnetic force ($\mathbf{F}_M$) to the cell membrane when an external magnetic field $\mathbf{H}_e$ is applied (see Fig.4.1a).
A sketch of the experimental setup is reported in Fig.4.6a. To monitor the particle manipulation during the experiments and carry out imaging of the effect of the mechanical stimuli on cells, a *Leica TCS SP5* confocal laser scanning microscopy is used, based on an upright *DM6000CFS* microscope and equipped with a *HCX Apo* L20x/1.0 NA W water immersion objective. At the beginning of the experiments, the chip on which cells are cultured is gently washed in 2 ml of PBS to remove the cellular medium sediments on the surface, which could negatively affect the particles manipulation. Then, the chip is placed on a Petri dish in 1 ml of PBS, located in a microscope chamber (see Fig.4.1b) with a controlled temperature (37 ^{o}C) and wet atmosphere.
The external magnetic field needed to manipulate the DWs is applied using a couple of Neodymium Iron Boron ($Nd_2Fe_{14}B$) permanent magnets underneath the microscope stage. The field direction is set by a stepper motor which allows fine control of the magnets' rotation, thus producing a uniform magnetic field mainly parallel to the chip surface, with a maximum absolute value of 50 mT. This field covers simultaneously all the magnetic conduits. The confocal microscopy images are elaborated by means of *ImageJ* software to analyze the cellular profiles, merge fluorescent images and obtain 3D cellular reconstructions from *z-series* images.

Commercial *MyOne*-Dynabeads superparamagnetic particles, functionalized with COOH are used (Invitrogen, 1 μm diameter, magnetization of saturation M_S = 35 x 10^3 A·m^{-1} and magnetic susceptibility in the linear range $\chi_0 = 1.46$). They are diluted in phosphate buffer solution (PBS), to reach a final concentration of 1 μg·ml^{-1}. The values of M_S and χ_0 are measured by using a Vibrating Sample Magnetometer (VSM) (see section 3.6).

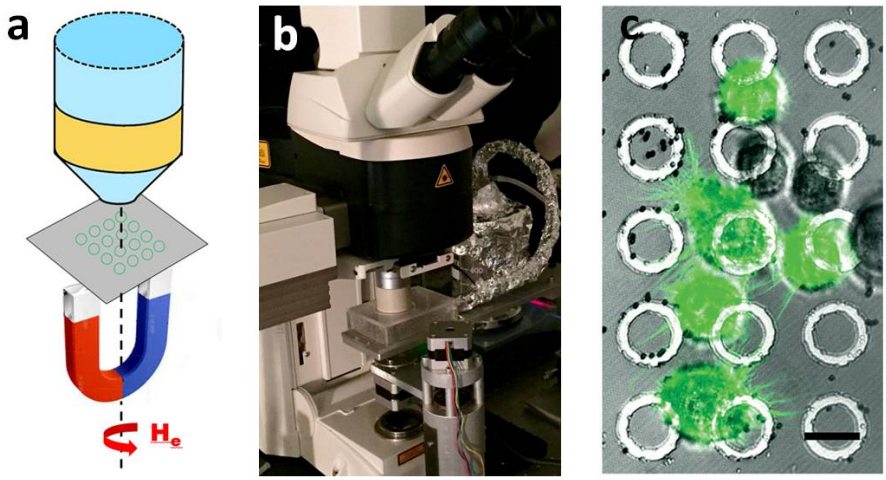

Figure 4.6: **a** Sketch and **b** picture of the experimental setup showing an optical microscope used to monitor the particles manipulation, a chamber for controlled temperature and wet atmosphere, permanent magnets for the application of the external field ($\mathbf{H}_e$). A stepper motor allows to control the $\mathbf{H}_e$ rotation. **c** Optical image showing the chip with the magnetic nanostructures and HeLa cells transfected with GFP-Lifeact (green fluorescence), after dispensation of 1 μm superparamagnetic beads (MyOne Dynabeads). Scale bar: 20 μm.

4.4.2 Cell culture

HeLa cells are grown in Eagle's minimum essential medium (MEM; Gibco-BRL), supplemented with non-essential amino acids, 10% (vol/vol) fetal bovine serum, 2 mM glutamine, 25 mM HEPES and 100 μg·ml^{-1} streptomycin in a humidified incubator (5% CO_2, 37 ^{o}C). 36 hours before the

experiment, cells are transfected with GFP-Lifeact[117] (F-actin marker for visualization of cytoplasm) using lipofectamine-2000 (Invitrogen). The day before the experiment, the microfabricated chips are placed in 6-well dishes, cleaned with ethanol once, washed in PBS three times and then allowed to dry in the hood. Then, cells are plated onto the chip in order to achieve a cell confluence of approximately 50% during the experiment.
An optical image showing the chip with the transfected cells cultured on top is reported in Fig.4.6c.

4.4.3 Manipulation of magnetic beads in a cell culture environment

The DWs nucleated in magnetic rings allow the trapping and manipulation of a 1 μm bead into the cellular membrane of single HeLa cells cultured on chip, applying a rotating external magnetic field $\mathbf{H}_e$ of 30 mT. The trapping is clearly visible, looking at panels i and ii of Fig.4.7, while the subsequent manipulation towards the cell membrane can be appreciated by comparing panels ii and iii.

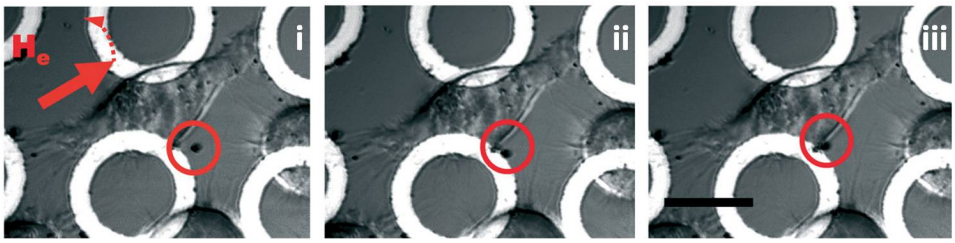

Figure 4.7: Frames from a video showing the attraction and manipulation of a 1 μm particle to the cellular membrane of a target HeLa cell when a rotating $\mathbf{H}_e$= 30 mT is applied. Scale bar: 20 μm.

Note that, the maximum bead velocity achievable in a fluid is of the order of tens of μm s^{-1} to ensure a synchronous motion of the bead and DW. Under these conditions, the particle momentum is quite low ($\approx$10-20 kg·m s^{-1}) and the force applied when a free bead hits the membrane is negligible. Even assuming an elastic scattering from the cell membrane in a typical interaction

time of ≈0.1 s, the average force does not exceed 1 aN. This value is much lower than typical forces applied in mechanobiology studies, which are in the pN-nN range. However, as discussed in the previous sections, higher values can be obtained by exploiting the in-plane attractive force exerted by the domain wall on magnetic beads continuously pushed against the cell membrane (see the next section).

4.4.4 Mechanical deformation of target cell membranes

In order to demonstrate the effectiveness of our technology, DWTs are used to produce a mechanical deformation on target HeLa cell membranes. Cells are cultured on microfabricated chips with the magnetic rings, as described in section 4.4.2. Then, beads are dispensed on the chip and, upon capture by a DW, manipulated to bring them in contact with the cell membrane (see Fig.4.7).
Here, due to the opposite zeta-potential of the HeLa membrane (negative)[118] and beads (positive), electrostatic interaction occurs. Hence, some particles tend to bind to the membrane. When the DW is displaced, bound particles initially apply a tensile strain to the cell membrane, until they detach when the attraction of the moving DW overcomes the electrostatic interaction. In this framework, the best configuration for applying sizable and durable forces is that corresponding to a compressive strain, or inward force with respect to the cell, which can be achieved by pushing the beads against the membrane. This can be achieved by slightly displacing the DW towards the inner part of the cell, if the conduit crosses the cell contour line, or simply by exploiting the attraction from a DW in a conduit which is within the cell contour line. The second case is reported in Fig.4.8.
Some frames from the video show a cluster of magnetic beads in contact with a green fluorescent HeLa membrane, manipulated by DWTs. When rotating the in-plane external field ($\mathbf{H}_e$ = 30 mT), the passage of the two opposite DWs (red and blue lines in Fig.4.8(i-vi)), provokes the attraction of the particles towards the ring edge, producing a local membrane deformation (Fig.4.8(i)). As previously discussed, the beads stay attached to the cell membrane when the DW is displaced away. The magnetic force is re-

leased and the cell membrane recovers its initial equilibrium configuration (Fig.4.8(ii)). When the DW is far away from the cluster, the particles are aligned along the external field direction (Fig.4.8(iii-iv)), but they are still bound to the cell membrane due to the electrostatic interaction. Meanwhile, when the DW approaches the particles again, they aggregate in a more compact configuration due to the localized attraction of the DW (see Fig.4.8(v)). The competition between electrostatic and magnetic forces is clearly seen, comparing frames 4.8(v) and 4.8(vi). In this case, due to a quasi-static displacement of the DW, three particles follow the DW along the cell contour, whereas two of them remain attached to the membrane at the position previously occupied by the DW.

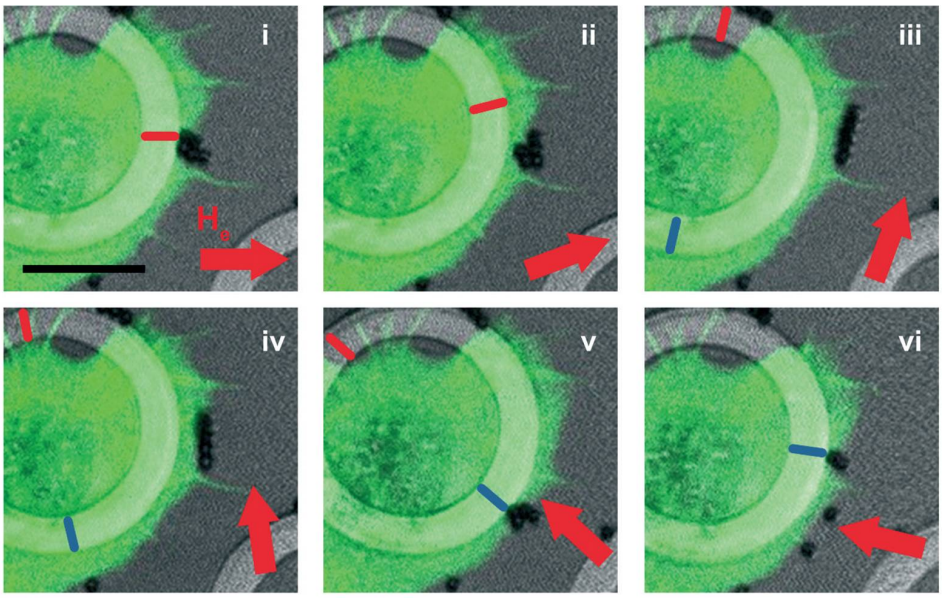

Figure 4.8: Frames from a video showing the manipulation of a cluster of 5 superparamagnetic beads (*MyOne*-Dynabeads, 1 μm) in contact with the cellular membrane of a green fluorescent HeLa cell (marked with GFP-Lifeact) when a rotating external field ($\mathbf{H}_e$) of 30 mT is applied. The DWs (red and blue lines) displaced along the magnetic ring by $\mathbf{H}_e$ exert an attractive force on the beads, producing a local deformation of the cellular membrane. Scale bar: 10 μm.

In order to quantify and properly study the deformation produced by DWTs, a 3D profile analysis of the HeLa cell is carried out. The confocal microscope allows 3D imaging of cells with a lateral resolution lower than 500 nm and a vertical resolution of about 1 μm.
Such analysis is illustrated in Fig.4.9 and it is related to the same cell shown in Fig.4.8. The case in which no mechanical stimuli are applied to the mem-

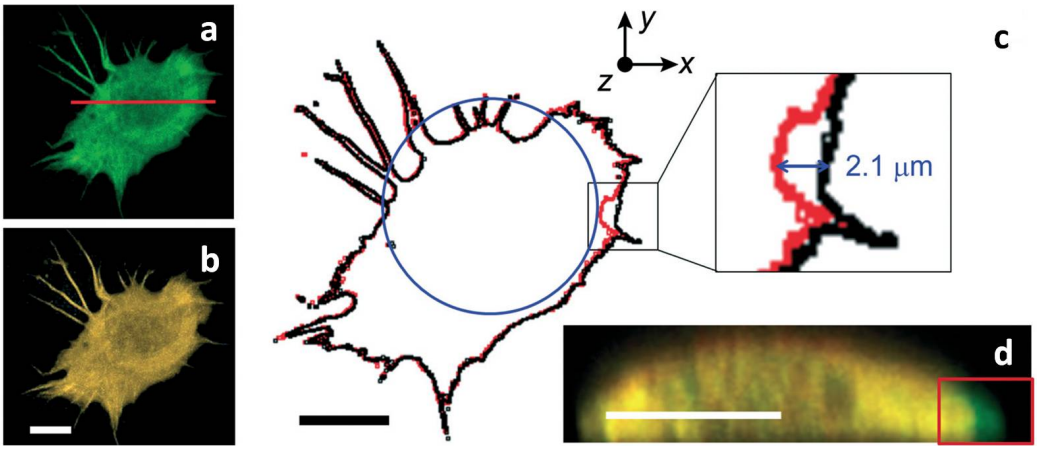

Figure 4.9: Confocal image of the HeLa cell basal membrane before **a** (green) and during **b** (orange) the local mechanical deformation. The data are acquired in about 60 s, after the application of the mechanical stimulus. Overlapped cellular profiles before (black) and during (red) the local membrane deformation are shown in panel **c**. A reconstruction of a HeLa cell slice in the plane perpendicular to the chip surface corresponding to the red line in panel **a** is reported in panel **d**, before (orange) and during (green) the mechanical deformation. Scale bars: 10 μm.

brane (see Fig.4.9a, green) is compared with the cell with a membrane invagination produced by magnetic beads (Fig.4.9b). Fig.4.9a-b reports the cell basal membrane, acquired before and during the application of the stimulus. This particular plane is selected as it identifies the position along z where the beads cluster (trapped by the DW on the chip surface) is located. Thanks to the high fluorescence signal intensity and to the low auto-fluorescence background, the cellular profiles are easily extracted from the fluorescence images

and overlapped, as shown in Fig.4.9c. In this way, the quantification of the membrane deformation is performed, leading to a maximum indentation of 2.1±0.5 μm in the selected cell plane. The error in the evaluation of the indentation depth is mainly due to some uncertainty in the profile elaboration due to microscope resolution. This result is confirmed by the cell section displayed in Fig.4.9d, obtained cutting it with a x-z plane whose projection is marked with a red line in Fig.4.9a, before (green) and during (orange) the mechanical stimulation. A clear membrane deformation is produced also along the z-axis, in agreement with the micrometric size of the beads employed. Note that the reported data correspond to the equilibrium deformation of the cell membrane under the application of a constant mechanical load.

4.4.5 Magnetic forces exerted on the cell

The magnetic force producing such a deformation is calculated according to the method described in section 4.3.1. In the particular case of the experiment described in the previous section, $\mathbf{F}_M$ is due to a cluster of five particles, as illustrated in Fig.4.10a.

The cluster geometry, shape and orientation are carefully extracted from the confocal optical images (see the zoomed-in view of Fig.4.10a). The map of the radial in-plane component ($\mathbf{F}_r$) of the force exerted on the whole cluster is displayed in Fig.4.10b. This force is calculated combining Eq.4.1, Eq.4.2 and Eq.4.3, as discussed in section 4.3.1.

Only the radial component is shown because the force causing the membrane deformation is perpendicular to the ring tangent in our experiment. The force is reported as a function of the position of the center of the bottom-left bead in the cluster, which is translated all over the x-y plane. In Fig.4.10c the radial force on the cluster along the direction identified by the black dashed line in Fig.4.10b is also plotted.

For the bead configuration illustrated in Fig.4.10a, the simulated applied magnetic force is 480±50 pN. The main source of the error is the uncertainty in the evaluation of the relative position between the cluster and the DW. In particular, the relative orientation of the external field with respect to the chip and therefore the position of the nucleated DW is set with an error of

±3 degrees, while the spatial position of the beads in the cluster is estimated with an accuracy of 200 nm in the x-y plane.

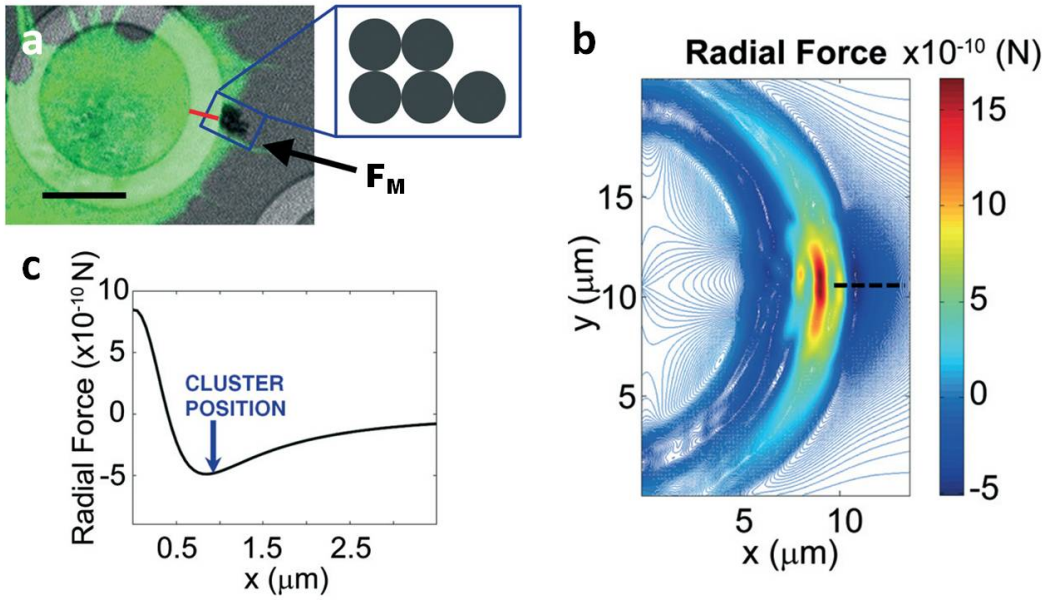

Figure 4.10: **a** Optical image showing the HeLa cell membrane deformed by a cluster of 5 magnetic beads. The sketch in the zoomed-in view represents the cluster geometry used for the evaluation of the magnetic force. Scale bar: 10 μm. **b** contour plot of the simulated radial magnetic force with respect to the ring, exerted on the bead cluster 100 nm above the nanostructure as a function of the position of the left-bottom bead in the cluster. **c** plot of the radial force, evaluated along the direction of the black dashed line. The arrow represents the centre of the left-bottom bead in the cluster, extracted from confocal images.

4.4.6 Elastic membrane model of lateral indentation

To check the consistency in the mechanical stimulus applied to the cells and the deformation observed during the experiments, an elastic model of the cellular membrane has been developed.
Since the observed overall membrane deformation is small compared to the

cell diameter, the external forces are mainly counterbalanced by the bending of the cell membrane, which is considered as an elastic shell[119] with a Young's modulus[120] E = 5 x 10^{-5} N·μm^{-2} and a Poisson ratio[121] $\nu = 0.5$. The membrane is locally modeled as an elliptical surface (see Fig.4.11) with positive Gaussian curvature everywhere.

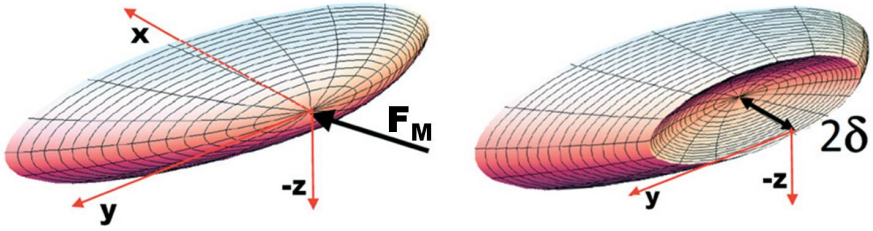

Figure 4.11: Sketch of the analytical surface used to model the cell membrane geometry, in proximity to the position where the mechanical load is applied, producing an indentation of 2δ.

Note that, from a biological point of view, the key assumption of this model is to neglect the role played by the underlying actin-cortex, modeling the cell as a large liposome, where the membrane is not linked to the actomyosine cortex. Although it is a simplified picture of the real cell behavior, we consider this assumption valid here, as the local deformation of the cell membrane is small and the lifeact-signal (acquired during the experiments) does not show significant alterations in the cytoskeleton structure, when the mechanical stimulus is applied.
Considering the beads as a distributed load acting on the membrane, the elastic force that counterbalances the magnetic one is expressed (see Appendix A for the derivation) by the following equation[122][123]:

$$F_{el} = \frac{3c\pi E}{12^{3/4}(1-\nu^2)} h^{5/2} \frac{(2\delta^{1/2})}{2\cdot(2-\beta)} \left(\frac{1}{R_y} + \frac{1}{R_z}\right) \tag{4.5}$$

The y-z plane is tangent to the cell membrane at the point representing the geometrical centre of the area where the force is applied. The surface is locally characterized by the principal curvature radii R_y and R_z, whilst 2δ is the indentation length produced by beads on the cell. It can be shown

that the deformed shape of the cell membrane can be obtained by reversing the shape of the paraboloid with respect to the plane at x = δ, producing mirror buckling. The dimensionless parameter c = 1.15 is a constant obtained by minimizing a certain displacement functional under a nonholonomic constraint[124] and β indicates the portion of the free boundaries where the force is applied. The local curvature radii, extrapolated from the confocal images before the application of the mechanical stimulus, are $R_y = 8\pm0.5$ μm and $R_z = 1.85\pm0.5$ μm for the same cell displayed in Fig4.9. The uncertainty depends on the microscope resolution and on the peculiar membrane profile smoothing required to average-away the small HeLa protrusions. The cluster of beads produces a mechanical distributed load on an area of 2 μm^2 and the maximum lateral indentation is $2\delta = 2.1$ μm, as previously measured.
With these numbers, the calculated mechanical stimulus applied to the cell membrane is 575±134 pN, as calculated from Eq.4.5. The error arises from the uncertainty in the evaluation of the cell geometry (R_y, R_z, 2δ) from the optical images and in the actual parameters used in numerical calculations. It is noteworthy that this result is in excellent agreement with the magnetic force calculated through micromagnetic simulations (480±50 pN), thus confirming the reliability of the force quantification via magnetic simulations.

4.5 Manipulation of nanoparticles inside the cell cytoplasm

Magnetic manipulation represents an unique, non-invasive method to handle small objects inside the cytoplasm or nucleus, allowing to apply mechanical stimuli[125] and to transport biomolecules at subcellular level[108]. Noteworthy, no other techniques can accomplish to this goal without provoking cell damage[12]. In this section, the possibility to use DWTs platform for manipulating magnetic particles inside the cytoplasm of HeLa cells is investigated. To this end, 500 nm magnetic beads are micro-injected (see Fig4.12a) inside the cytoplasm of HeLa cells cultured on DWTs chip and then manipulated using the same experimental setup described in section 4.4.1. DWTs devices described in section 4.2 are used (150 $Ni_{80}Fe_{20}$ thickness), fabricated on

SiO_2 substrates to monitor the microinjections performed under an inverted microscope. Particles are inoculated by means of micrometric needles, fabricated by a micro-extrusion process, using *P 1000* (Sutter Instrument) puller machine. The needle tip diameter (where particles flow-out) ranges between 0.8-1.1 μm according to a pre-calibration of the *P 1000* (Sutter Instrument) parameters, by Scanning Electron Microscopy. Note that the tip should be as small as possible to limit the damage provoked on cells during injections, but large enough to avoid occlusions.
Commercial *micromod* superparamagnetic beads (500 nm in diameter, functionalized with $COOH^-$), stained with a Cy5 (far-red) fluorescent marker, are injected and manipulated during the experiments. They are diluted to $10\mu g \cdot ml^{-1}$ and dispensed in a syringe connected to the needle.
The position of the needle during the injections is precisely regulated by a piezoelectric micro-manipulator, controlled by software; the entire process is monitored under an inverted microscope to select the cells to be injected. Around 50 cells are inoculated for each chip, using the optimized injection parameters illustrated in the following table:

$\mathbf{t}_{inj}$	$\mathbf{p}_{inj}$	$\mathbf{p}_0$
0.3 s	80-100 hPa	10 hPa

Table 4.1: Parameters used in the microinjection processes.

where t_{inj} is the time indicating the injection duration; p_{inj} is the fluid pressure inside the syringe during the injection, which allows the beads to flow-out overcoming the cytoplasm resistance. p_0 is the pressure of the solution before the injection. It has to be slightly higher then p_{atm}, to avoid the medium re-flux inside the needle.
After the injections, the chip is placed under confocal microscope (see section 4.4.1) to perform the experiment. In order to control that particles are efficiently injected inside the cytoplasm, cells are imaged in confocal mode acquiring z-stacks with z-depth of 500 nm to reconstruct the cell profile in the plane perpendicular to the chip. Fig.4.12 shows a cell in which a few particles are successfully injected.
The number of beads inside the cytoplasm of microinjected cells is affected

by a certain variability and, in around 30% of the cells, no beads are found. Moreover, in the microinjected cells the number of particles ranges between 2 and 5, depending on the bead size and on the exact position inside the cell where particles are inoculated.

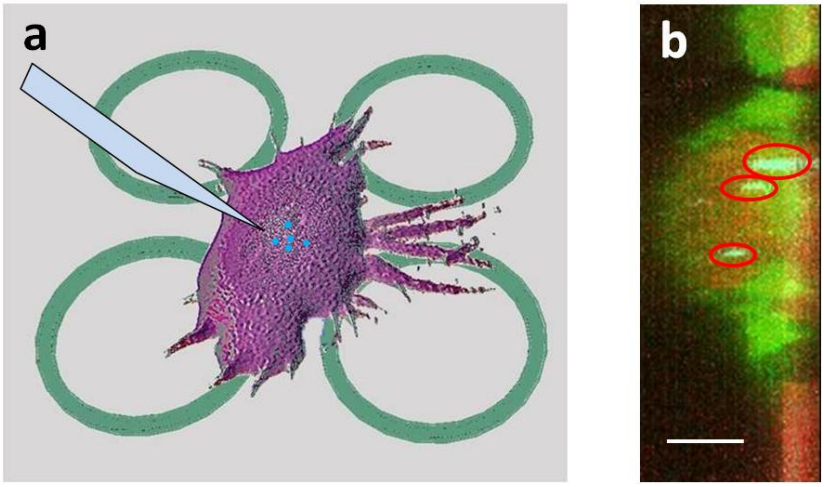

Figure 4.12: **a** Sketch of the microinjection procedure: magnetic beads are injected in the cytoplasm of HeLa cells cultured on chip by means of a micrometric needle. **b** HeLa cell lateral reconstruction from z-stack images projection along a plane perpendicular to the chip, showing few 500 nm nanoparticles inside the cell cytoplasm. Cells are transfected with GFP-Lifeact and particles are functionalized with Cy5 (far-red) fluorescent marker. Red circles indicate the position of magnetic beads (light-blue) inside the cell. Particles appear elongated due to the confocal microscopy resolution in z-direction (≈ 1 μm) and to artifacts arising from z-stacks reconstruction. Scale bar: 5 μm.

Even if this variability suggests that the injection procedure can be further optimized, it does not prevent to perform the experiments. In order to check the biocompatibility of this microinjection procedure, cells are monitored for 3 days. No evident alterations of cell viability are observed, although the rate of cell division slightly decreases.
Beads injected inside the cell are manipulated exploiting again the stray field

exerted by DWs in magnetic rings when a uniform $\mathbf{H}_e$ is applied. A DW is nucleated in proximity to a microinjected bead, in order to trap and manipulate it. The attracting force exerted by the DW moves the particle to the cell basal plane and the $\mathbf{H}_e$ rotation allows for manipulating it along the ring edge, coherently with the DW motion (see Fig.4.13).

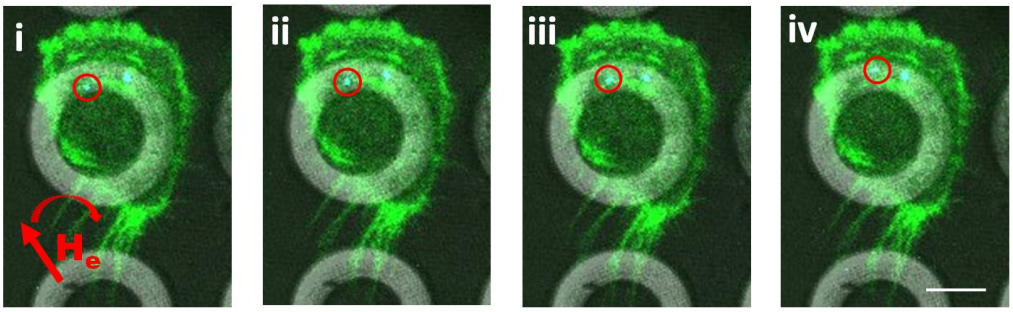

Figure 4.13: Frames from a video showing the manipulation of a 500 nm particle microinjected inside the cell cytoplasm, when a rotating external magnetic field is applied. Red circles highlight the particle position and the field is rotated with an angular speed of 1 deg/s.

Due to the high friction experimented by the particles inside the cell, $\mathbf{H}_e$ is rotated very slowly ($\approx$1 deg/s with steps of 2 deg each) to allow a synchronized motion between bead and DW. The particles follow the DW motion until larger forces arising from the interactions with the cytoskeleton or organelles occur, overcoming the magnetic force. However, around 30% of the microinjected particles can be manipulated adopting this strategy, travelling a distance larger than 5μm inside the cell. Even if this is a preliminary result, it clearly demonstrates the possibility to manipulate nanoparticles inside the cell cytoplasm using DWTs. Note that, higher forces can be applied using larger particles or favoring the formation of beads clusters, upon optimization of the injection procedure to increase the amount of inoculated beads (but preserving the cell viability).
This result paves the way to possible mechanobiological studies at subcellular level, manipulating particles to a specific cell compartment in order to exert there mechanical stimuli. Another strategy could exploit properly

functionalized particles to favor their interaction with target organelles (e.g. cell nucleus) where forces can be applied by DWTs in a similar way to the one described in section 4.4.

4.6 Conclusions

An on-chip platform based on magnetic domain wall tweezers, allowing for the application of finely controlled and localized forces on target cell membrane and the manipulation of particles inside cell cytoplasm has been presented in this chapter.

Magnetic structures patterned on-chip are exploited to implement a non-invasive method, fully biocompatible and integrated with conventional setups for cell investigation. No relevant limitations on the numerical aperture, working depth, magnification or imaging modality have emerged so far. With respect to previous works[69][67], the geometry of the magnetic rings has been optimized to maximize the magnetic force (Permalloy thickness of 150 nm). This leads to values of $\mathbf{F}_M$, approaching the nN range over an area of a few μm^2, which are suitable for mechanobiology studies where localized forces on specific cell compartments are required[126]. In addition, by modulating the external magnetic field, a fine tuning of the applied forces can be reached.

Finally, with this approach, precise quantification of the exerted forces can be performed via micromagnetic simulations, using as input parameters only the actual bead position with respect to the DW in the conduit. In perspective, the system can be integrated using dedicated software which calculates the mechanical stimuli strength in real time, thus providing biologists with a quantitative tool for the application of localized forces on or inside cells. As an example, this technique could be used to probe the plasma membrane tension on different phases of cell spreading and migration.

Chapter 5

Magnetically actuated micropillars

The mechanical properties of cells and nuclei are crucial to many biological processes, including migration[2], proliferation[3] and gene transcription[4]. In vivo, cells are frequently exposed to multiple mechanical stimuli arising from the extracellular matrix, on a variety of time and intensity scales. However, current techniques for mechanobiology studies do not allow to apply such inhomogeneous and prolonged forces (see section 1.1).
This chapter presents a novel device based on magnetically actuated micropillars, as a technique for studying the mechanical coupling between cell membrane and nucleus in living cells. This technology relies on Fe-coated PDMS micropillars which, under the action of a rotating magnetic field, produce mechanical pinching on different points of the cell membrane with a highly controllable intensity and time evolution.
In the first part, the device working principle and characterization are described together with a quantification of the forces exerted by magnetic pillars.
The second part demonstrates the potential of this technique by investigating the cell nucleus mechanical properties and dynamics in response to mechanical stimulation induced by magnetic pillars. In particular, we show how the application of forces (tens of nN) on the cell, at a pinching frequency of 0.1 Hz affects the cell nuclear morphology, deformability and H2B core

histone turnover on chromatin. The measurement of the typical nucleus response time to the mechanical stimuli indicates how, at the selected pinching frequency, nucleus-pillars coupling is not purely elastic but mediated by active cellular mechanisms. Indeed, an enhancement in actin dynamics during stimulation is observed, thus demonstrating that it plays an active role in forces transmission. Finally, the detection of MKL transcription-cofactor translocation from the nucleus to the cytoplasm during stimulation, reveals that mechanical pinching can affect genomic functions.
This novel method constitutes a new enabling technology for the development of a new route in mechanobiology: the quantitative investigation of the cell response dynamics to multiple and localized time-dependent mechanical stimuli.

5.1 Device Fabrication

Magnetic pillars are made of Polydimethylsiloxane (PDMS) with ferromagnetic heads of Fe. These magnetic pillars are fabricated in repeated groups of 4 (see Fig.5.1b).

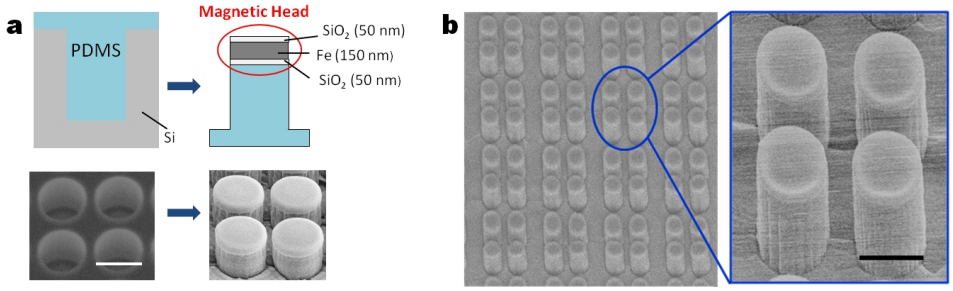

Figure 5.1: **a** Sketch of the magnetic pillars fabrication process: PDMS is cast on a Si mold and, after curing, it is peeled out, subsequently a trilayer of $SiO_2/Fe/SiO_2$ is deposited by e-beam evaporation. On the bottom, scanning electron microscopy (SEM) images showing the mold and the coated pillars. **b** SEM image of the device. Magnetic micropillars are 10 μm high, 5 μm in diameter and spaced 2 μm. On the right: zoom on a single group of 4-pillars. Scale bar: 5 μm.

Each pillar is 10 μm high, 5 μm in diameter with a minimum distance of 2 μm (when no external magnetic field is applied). They are prepared (see Fig.5.1a) by replica molding from a Si substrate, patterned by photolithography and reactive ion etching. PDMS is cast on top of the mold and thermally cured at 80 ^{o}C for 3 hours, before the peeling procedure.
On top of PDMS a tri-layer of SiO_2 (50 nm)/ Fe (150 nm) / SiO_2 (50 nm) is deposited by e-beam deposition. The first SiO_2 layer favors the adhesion of Fe on top of PDMS, while the second layer isolates the magnetic material from the biological environment. Fe is chosen as ferromagnetic material for pillars actuation due to its reduced toxicity together with a large saturation magnetization (M_S= 1.72×10^6 A·m^{-1}).

5.2 Working principle and Simulations

The basic idea of the device is illustrated in Fig.5.2 with reference to a single couple of pillars.

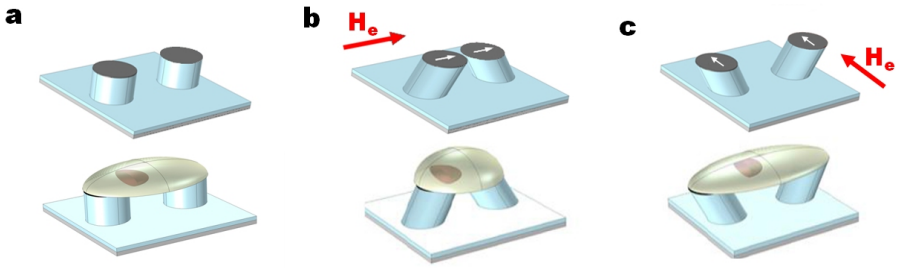

Figure 5.2: Sketch of the device working principle: the application of an uniform external magnetic field ($\mathbf{H}_e$) induces adjacent pillars interaction, producing pillars bending. In **a** the system is in the rest condition (when $\mathbf{H}_e$ is null). Attraction **b** and repulsion **c** of two adjacent pillars occur $\mathbf{H}_e$. Cell cultured on top are exposed to mechanical stimuli.

The application of uniform in-plane magnetic fields ($\mathbf{H}_e$) allows for the mechanical actuation, driving the interaction between pillars. When $\mathbf{H}_e$ is directed along the line connecting the pillars centers, they experiment an attractive force (Fig.5.2b). Instead, when a field perpendicular to the previous

one is applied, a repulsive force is exerted between them (Fig.5.2b). Therefore, cells cultured on top of a couple of magnetic pillars can be exposed to stretching and compressive mechanical stimuli.
Considering a group of 4 pillars, the force field becomes more complex. Here, each pillar simultaneously interact, both in the horizontal and vertical direction, with the neighbors pillars. Indeed, when the $\mathbf{H}_e$ is directed along the line connecting two pillars centers, they experiment an attractive force along that direction (as in Fig.5.2b), but a repulsion occurs in the perpendicular one (as in Fig.5.2c). In this way, if a rotating field is applied, a continuous pillars compression and stretching occurs, either in the vertical and horizontal direction, exerting a periodic and bidirectional mechanical stimulus on cells, as will be discussed in details in section 5.5.
The physical working principle is the following: considering again a couple of adjacent pillars, the application of $\mathbf{H}_e$ along a certain in-plane orientation aligns the magnetization ($\mathbf{M}$) of Fe-disks on top of the pillars in that direction. In this condition, two adjacent pillars reciprocally interact, as $\mathbf{M}$ in the first Fe-disk produces a magnetic stray field gradient on the second and vice-versa.
The micromagnetic configuration of these magnetic pillars is simulated with the software OOMMF[115], using the following parameters for Fe: saturation magnetization $M_s = 1.72{\times}10^6$ Am^{-1}, exchange stiffness $A = 2.1{\times}10^{-11}$ Jm^{-1}, damping coefficient $\tau = 0.01$ and null magneto-crystalline anisotropy (this is in agreement with the magnetic characterization of our device, showing no in-plane anisotropy and the polycrystalline nature of the Fe film grown on PDMS). A $20{\times}20{\times}20$ nm^3 unit cell has been used for simulating the micromagnetic configuration of Fe-disks. Although the exchange length of iron is 2.4 nm, this represents a reasonable compromise ensuring reduced computational times.
Micromagnetic configurations of a couple of adjacent pillars are reported in Fig.5.3, when $\mathbf{H}_e$= 50 mT is directed at 0, 45 and 90 degrees (Fig.5.3a-c) with respect to the x-axis.
In all the three cases, $\mathbf{M}$ is aligned to the external field, resulting in a mono-domain configuration of Fe-disks. Similar single-domain configurations are simulated for $\mathbf{H}_e$ ranging between 10-100 mT. Hence, Fe-disks acts as two

magnetic dipoles, experiencing a magnetic force ($\mathbf{F}_M$) which induces pillars bending.

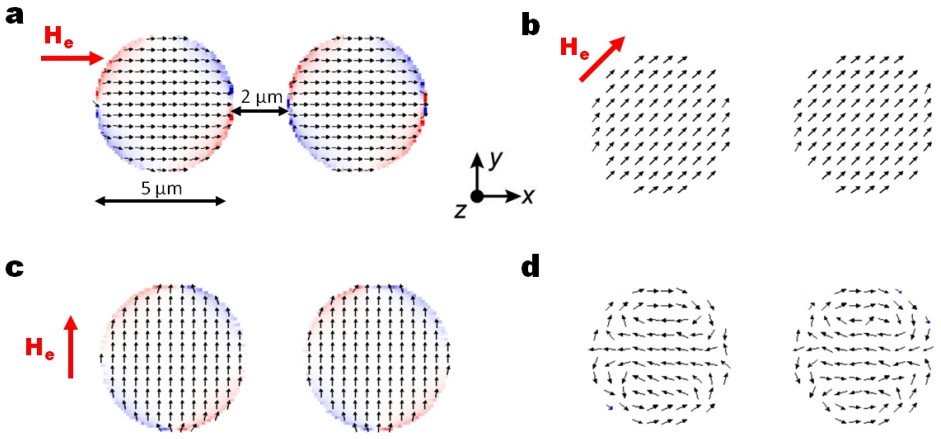

Figure 5.3: Micromagnetic configuration (simulated using OOMMF) of two adjacent Fe-disks on top of PDMS pillars, when an external magnetic field ($\mathbf{H}_e$) of 50 mT oriented at 0, 45, 90 degrees (**a**, **b**, **c**) with respect to the x-axis is applied. In **d**, micromagnetic configuration in remanence, after the application of a saturating $\mathbf{H}_e$ along the x-axis. The arrows represent the local magnetization direction, while the red-white-blue scale color in **a** (and **c**) refers to the y-component (and x-component) of the magnetization.

According to dipole-dipole interaction, $\mathbf{F}_M$ is attractive when $\mathbf{H}_e$ is directed along the line connecting the two pillars centers (see Fig.5.3a), while $\mathbf{F}_M$ is repulsive if $\mathbf{H}_e$ is perpendicular to the x-axis (see Fig.5.3c). The magnetic force becomes null for a certain angle between 0 and 90 degrees with respect to the x-axis.
Starting from the micromagnetic configurations, the magnetic stray field is simulated with OOMMF and the value of $\mathbf{F}_M$ is calculated, according to the following equation:

$$\mathbf{F}_M = \mu_0(\mathbf{m} \cdot \nabla \mathbf{H}) = \mu_0 \int_V (\mathbf{M} \cdot \nabla \mathbf{H}) dV \tag{5.1}$$

where $\mathbf{m}$ is the magnetic moment of Fe-disks and $\mathbf{M}$ the magnetization; according to the pillars micromagnetic configuration (see Fig.5.3), $\mathbf{M}$ is con-

sidered uniform all over the disk volume, obtaining a simplified formula of Eq.2.21 [84]. $\mathbf{H}$ is the total field ($\mathbf{H} = \mathbf{H}_d + \mathbf{H}_e$), also calculated using OOMMF. It is the sum of the stray field generated by the adjacent pillars ($\mathbf{H}_d$) and the external magnetic field ($\mathbf{H}_e$). The integration is performed numerically over the Fe-disk volume (V).

$\mathbf{F}_M$ is calculated for $\mathbf{H}_e$= 50 mT (which is the same value used during the biological experiments) directed at 0, 45 and 90 deg with respect to the x-axis (see Fig.5.3).

An attractive force $\mathbf{F}_M$= 47.8 nN is found when the field is oriented along the x-axis, while a repulsive one $\mathbf{F}_M$= -13.7 nN is calculated for $\mathbf{H}_e$ applied along the y-axis. When H_e is directed at 45 deg, a lower compressive $\mathbf{F}_M$= 11.3 nN occurs. Note that, hereafter, the attractive force is considered positive, while the repulsive one negative. According to a dipole-dipole interaction, the absolute values of attractive and repulsive forces are maximized when H_e is directed, respectively, along the x-axis and y-axis (see Fig.5.3).

Therefore, the attracting force is more than three times larger than the repulsive one, indicating that stimuli applied on cells are mainly compressive.

Furthermore, the magnetic configuration in remanence has been simulated, upon the application and removal of a saturating H_e along the positive direction of x-axis (see Fig.5.3d). It results in multi-domains configuration where $\mathbf{M}$ is no more uniformly aligned. The magnetic force exerted in this case is $\mathbf{F}_M$= 1.2 nN (compressive), much lower than the maximum value for $\mathbf{H}_e$= 50 mT, thus indicating that the hysteretic behavior of Fe-disks has a reduced effect on $\mathbf{F}_M$.

To highlight the dependence of $\mathbf{F}_M$ on the field direction, the x-component (F_x) is plotted (see Fig.5.4a, red line), as function of the angle between the field and the x-axis (ϕ).

It shows how, when a rotating $\mathbf{H}_e$ = 50 mT is applied, F_x is periodic in ϕ and the simulated values are well fitted by a sine function (see red-line in Fig.5.4a), as expected for the case of two well separated interacting dipoles, so that the dipolar approximation for the field can be used.

In the simplified case of two pillars, the x-component of $\mathbf{F}_M$ is the only relevant contribution to the force, as the pillars interact only in that direction and the y-component is $\approx$0.

However, for groups of 4-pillars (see Fig.5.1b), a force is exerted also along the y-axis, due to the proximity of the adjacent pillars in that direction. In first approximation, considering only the interactions between first neighbors pillars, F_y is equivalent to F_x but shifted by 90 degrees (see dashed blue-line in Fig.5.4a). In fact, when the field is directed along the x-axis, a compressive force is applied along that direction and repulsive one is exerted in the perpendicular one. The opposite situation occurs when ϕ= 90 deg, adjacent pillars are attracted in the vertical direction and stretched in the horizontal one.

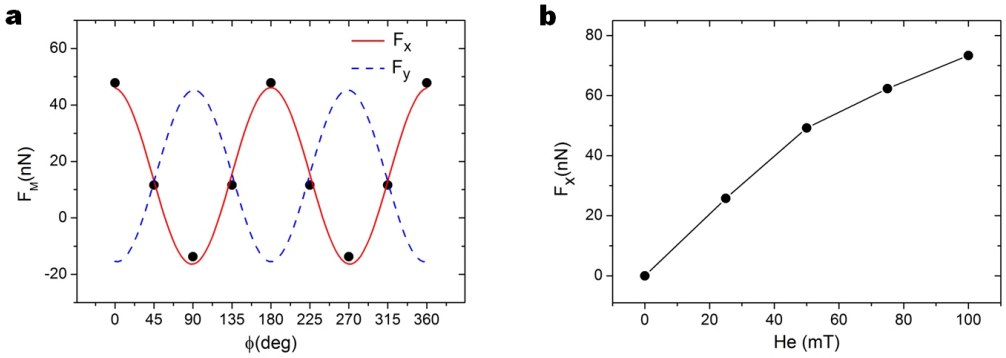

Figure 5.4: **a** Simulations of the magnetic force ($\mathbf{F}_M$) exerted on magnetic pillars, as function of the field direction (ϕ), when a rotating $\mathbf{H}_e$ = 50 mT is applied (black dots). The simulated data (black dots) are fitted with a sinusoidal curve for the x-component (F_x, red-line). The y-component (F_y, dashed blue-line) has the same behavior of F_y, by symmetry, but displays a phase shift of 90 degrees. These calculations neglect interactions along the diagonals of the square group of four pillars, which would introduce some distorsion on top of the biaxial tress field seen so far. **b** Calculation of the x-component of the magnetic force (F_x) between two adjacent magnetic pillars as function of $\mathbf{H}_e$, directed along the line connecting the Fe-disks centers.

As discussed before, the magnetization ($\mathbf{M}$) of Fe-disks is oriented along the field orientation. We expect that $\mathbf{F}_M$ increases with $\mathbf{H}_e$, because it favors the alignment of $\mathbf{M}$, resulting in larger magnetic moment of Fe-disks. This produces more intense stray field gradients and forces.

The x-component of $\mathbf{F}_M$ is simulated for a couple of pillars when $\mathbf{H}_e$ ranges between 0-100 mT, applied along the x-axis (see Fig.5.3a). As stated before, it corresponds to the orientation of $\mathbf{H}_e$ for which the attractive force is maximized. The result (see Fig.5.4b) displays how $\mathbf{F}_M$ increases with the external field, up to 73 nN for $\mathbf{H}_e$= 100 mT. Indeed, it demonstrates the possibility to tune the strength of the force with $\mathbf{H}_e$, thus controlling the entity of pillars bending and, consequently, the mechanical stimuli applied on cells.
In all the simulations, no magnetocrystalline anisotropy is considered. To demonstrate the coherency of this assumption, a magnetic characterization of the device is performed, as shown in the next subsection.

5.2.1 Magnetic characterization

The magnetic properties of the device have been measured by Vibrating Sample Magnetometry (see chapter 3). In order to understand if magnetic pillars exhibit a certain magnetocrystalline anisotropy, the magnetic response is evaluated at different directions of the external field ($\mathbf{H}_e$), applied in the device plane. The relative orientation (ϕ) between the sample and $\mathbf{H}_e$ is automatically regulated, rotating the first with steps of 10 degrees. For each position, a hysteresis loop is measured. Negligible differences have been found in the magnetic response at different ϕ, in terms of loops shape, saturation magnetization and coercive field (H_c). The typical hysteresis loop is illustrated in Fig.5.5a.
From this hysteresis loop, H_c = 5.3 mT is extrapolated and similar values are found at different angles. To further investigate the dependence of the coercive field on the sample orientation, H_c is plotted in a polar diagram, as function of ϕ (see Fig.5.5b).
The maximum variation in the value of H_e during the measurements is less than 3%, thus indicating that $\mathbf{M}$ does not lie along preferred crystallographic directions and, indeed, the device exhibits a negligible magnetocrystalline anisotropy.
Note that, due to the fabrication process, the deposited Fe is not located only on top of pillars but also on the PDMS basement. Therefore, the overall magnetic response is not only related to the Fe-disks on top of pillars, but also

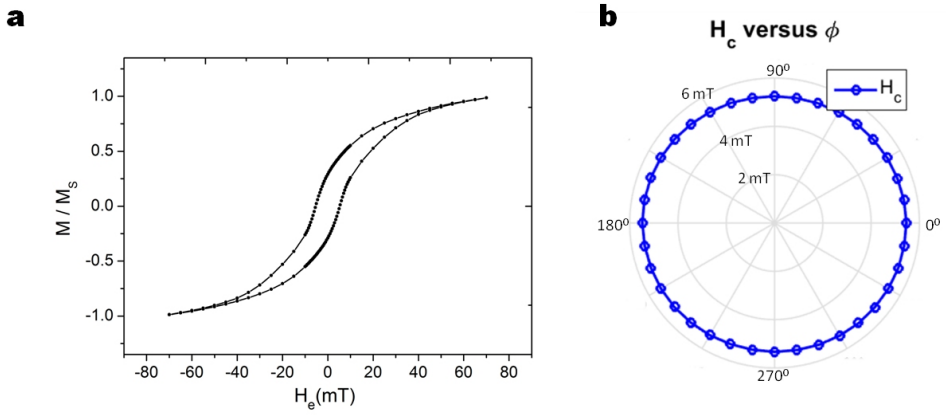

Figure 5.5: **a** Hysteresis loop of the device. **M** is divided by saturation magnetization M_S and calculated as function of the external magnetic field ($\mathbf{H}_e$) ranging between -75 and +75 mT. **b** Polar diagram showing the coercive field (H_c) as function of the the angle (ϕ) between the sample and $\mathbf{H}_e$.

this "extra-Fe" plays a role. However, the magnetocrystalline anisotropy, which depends on the atomic structure of the deposited metal, is not affected by this fact. Indeed, the Fe deposited on top of the device is magnetically isotropic and the assumption of considering null magnetocrystalline anisotropy during simulations, is coherent with this measurement.

5.3 Pillars deflection analysis

To evaluate the effect of $\mathbf{F}_M$ on the pillars deflection, a bending analysis of pillars displacement from the equilibrium position is performed, when $\mathbf{H}e$ is applied along the horizontal direction (see Fig.5.6a). In this case, an attractive force is exerted, as shown in section 5.2.
The deflection (Δx) is calculated as the difference between the Fe-disks centers distances with no field (x_0) and when an external field $\mathbf{H}_e$ ranging between 25-100 mT is applied (x_1). The center positions of pillars have been extracted from optical microscopy images, performing a circular 2D fitting of the Fe-disks edges.

The pillars bending $\Delta x = x_0 - x_1$, shown in Fig.5.6b, increases with $\mathbf{H}e$ as bigger magnetic charges induce larger pillars deflections. A maximum Δx of 620±130 nm is measured for $\mathbf{H}_e = 100$ mT.

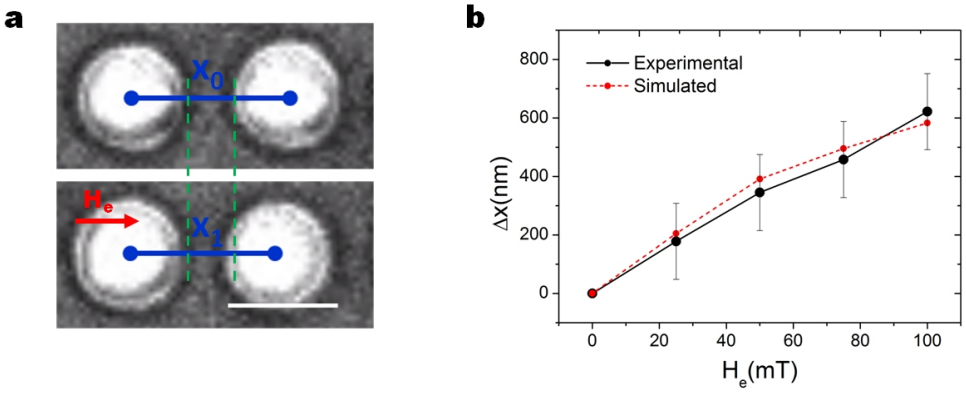

Figure 5.6: **a** Optical microscopy images of two adjacent pillars, comparing the distance between centers with (x_1) and without (x_0) the application of $\mathbf{H}_e = 50$ mT along the x-axis. **b** Experimental and simulated deflection ($\Delta x = x_0 - x_1$) of magnetic pillars as function of the external field ($\mathbf{H}_e$), directed along the x-axis. Scale bar: 5 μm.

The uncertainty in the evaluation of pillars deflection takes into account the microscope definition (pixel-size) and errors in the evaluation of pillars centers, due to 2D fitting procedure. Similar pillars bending are also found for negative values of H_e, coherently with the system symmetry. Moreover, according to the simulations shown in the previous section, the force exerted on Fe-disks in remanence is low, not significantly affecting x_0.
In order to prove that the experimental values of pillars deflections are consistent with the strength of the simulated forces (see Fig.5.4b), we applied an elastic model to our system. Each pillar is modeled as an elastic cylinder, with a Young modulus E. The elastic constant k is calculated according to the following equation[127]:

$$k = \left(\frac{3}{64}\pi \cdot E\frac{D^4}{H^3}\right) = \frac{2F}{\Delta x} \tag{5.2}$$

where D and H are pillars diameter and height, respectively. The simulated deflections are shown in Fig5.6b, as function of H_e. The value of E which allows the best fitting of the experimental data is equal to 2.56 MPa, slightly larger than the PDMS Young modulus (1.84 MPa)[127]. This is coherent with our system, as magnetic pillars are not simply made of PDMS, but some Fe on the side walls and a rigid tri-layer deposited on top confers a larger rigidity.
In the following sections, the way magnetic pillars are used for mechanobiology experiments is presented. First, the cell culture protocol and information on imaging procedures are provided. Then, before moving to the biological experiments, the mechanical forces experimented by cells, are described.

5.4 Cell culture and imaging

NIH3T3 fibroblasts stably expressing H2B-GFP are cultured in low-glucose Dulbecco's Modified Eagle Medium (Gibco; LifeTechnologies) supplemented with 10% (vol/vol) FBS and 1% penicillin-streptomycin (Gibco; Life Technologies) at 37^{o}C and 5% CO_2 in humid conditions.
Cells are transfected with RFP-Lifeact or mCherry-MKL by electroporation (Gibco; Life Technologies), the day before the experiment.
Then, cells are trypsinized (Gibco; Life Technologies) and seeded on micropillars coated with 20 μg/ml of Bovine Serum Albinum (BSA, Sigma Aldrich) and 100 μg/ml of Fibronectin (Gibco; Life Technologies) for at least 3 h. Before imaging, the chip is inverted in a petri dish, on two parafilm spacers (see section 3.7.2) to avoid contact between the cells and the bottom of the dish. A CO_2 free medium (Gibco; Life Technologies) is used during the experiments.
The dish containing the chip with the cells cultured on top is placed under a *Nikon A1R* Confocal microscope (see Chapter 3 for details on the setup). Acquisition is performed in bright-field and confocal modes with different acquisition rates according to the experiments: the fast dynamics is imaged with a rate of 0.5-1 fps, while the slow dynamics at 3 frames per minute. The z-depth for confocal imaging is $\approx$500 nm. Custom written codes in MATLAB are used for images thresholding, projected nuclear area calcula-

tion, geometrical parameters extrapolation and images correlation analysis. mCherry-MKL intensity and FRAP analysis are performed in $ImageJ$. Optical images are also generated in $ImageJ$. MKL-intensity images subtraction is performed in MATLAB.

5.5 Mechanical pinching on individual cells

To test our platform in a real mechanobiology case study, fibroblast are exposed to mechanical stimulation when a rotating $\mathbf{H}_e$ is applied. All the cells tested during the experiments spread on few (3-5) pillars groups (see Fig.5.7), thus experiencing a multiple stimulation in different points of the plasma membrane. Despite the pillars height (10 μm), the reduced pillars aspect ratio (see Fig.5.1b) makes the pillars tough enough, so that the cells do not significantly affect the pillars position during the experiments, at variance with what happens in case of passive pillars.

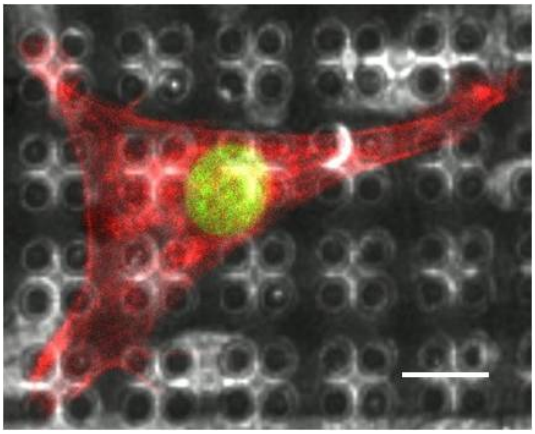

Figure 5.7: Optical image showing the device with the magnetic Fe-coated pillars and a single NIH3T3 cell transfected with RFP-Lifeact (red fluorescence) and H2B-GFP (green fluorescence). Scale bar: 20 μm.

The biocompatibility of magnetic pillars has been tested, monitoring the cells for three days. No evidences for alteration in cells viability is observed, as cell division seems not to be affected.

As mentioned before, the maximum attractive force which bends magnetic pillars at a certain field is more than 3 times larger than the repulsive one (see Fig.5.4a). Indeed, the mechanical stimuli arising from a group of pillars are mainly compressive. For this reason, such stimuli can be defined as a periodic and bidirectional mechanical pinching induced on the cell membrane. During all experiments an external field $\mathbf{H}_e$= 50 mT is applied, rotating at a fixed frequency f_F= 0.05 Hz. Due to the device symmetry, the pinching frequency is $f_P = 2f_F = 0.1$ Hz, as magnetic forces do not depend on the sign of $\mathbf{H}_e$.
In order to properly visualize the mechanical pinching when a cell is cultured on top, pillars are coated with fluorescent Cy5-fibronectin. Fig.5.8 shows the frames from a video, illustrating the different configurations of a group of 4-pillars, during the cell mechanical stimulation. Note that, the displacements obtained upon rotation of $\mathbf{H}_e$ by 180 degrees are the same, in agreement with a stimulation at $f_P = 2f_F$.

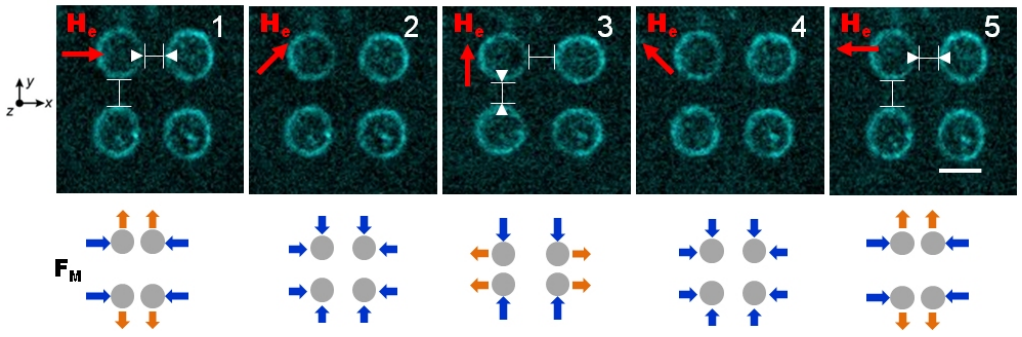

Figure 5.8: Frames from a video showing different magnetic pillars configurations when a rotating $\mathbf{H}_e$= 50 mT is applied. Pillars are sequentially attracted and relaxed in vertical and horizontal directions according to the orientation of $\mathbf{H}_e$. Pillars are coated with Cy5-fluorescent Fibronectin. The blue (and orange) arrows represent the direction of the attractive (and repulsive) force exerted on the cell by each pillar. Scale bar: 5 μm.

According to the working principle described in section 5.2 and shown in Fig.5.4a, when $\mathbf{H}_e$ is parallel to the line connecting two adjacent pillars centers (frames 1-3-5 in Fig.5.8), pillars are mainly attracted along those direc-

tions, while a lower repulsive force perpendicular to the external field is also applied. When $\mathbf{H}_e$ rotates depending on the field orientation, a time-varying stress field is exerted on the cell.
For example, rotating $\mathbf{H}_e$ from frame 1 in a counterclockwise direction, the absolute value of the two components (F_x and F_y) decrease (see Fig.5.4a) until F_y becomes equal to zero, while the force along x is still attractive. Then, either F_x and F_y become positive, resulting in a weak attraction in both the directions, as in frame 2 of Fig.5.8, when the field is directed along the diagonal. Subsequently, the x-component decreases to 0 and becomes repulsive, while F_y increases to its maximum (see frame 3), when the field is directed along the vertical direction. In this case, the force components are inverted with respect to frame 1, resulting in the maximum compression along y and extension along x.
The schematic map of the forces applied on cell by each pillar, for the different configurations, are illustrated in Fig.5.8 (blue arrows). Note that, for the symmetry of the system, when $\mathbf{H}_e$ is directed at 45 deg with respect to horizontal, the two components (F_x and F_y) have the same positive value (frames 2-4), resulting in a weak attraction either along x and y.

In the following sections, the biological experiments based on magnetic pillars are presented, showing how the mechanical stimuli described above affect cell and nucleus dynamics.

5.6 Magnetic pillars stimulation affects nuclear morphology

As discussed in section 1.1, the application of forces and the alteration of substrates stiffness can affect the cell nucleus shape[52],[4]. For this reason, we first investigate how the cell nuclear morphology is altered by the application of periodic mechanical pinching induced by magnetic pillars.
As quantitative indicator of the cell nuclear morphology, the eccentricity (ϵ) of nuclei projected area, extracted from fluorescence images, is used. The cells are first imaged for 3 minutes in static conditions, i.e. with a constant

field $\mathbf{H}_e$ at 45 degrees with respect to the side of the pillars square (as in frame 2 of Fig.5.8). Then, the periodic pinching is activated and cells are imaged for additional 9 minutes with an acquisition rate of 0.5 fps (see Fig.5.9).

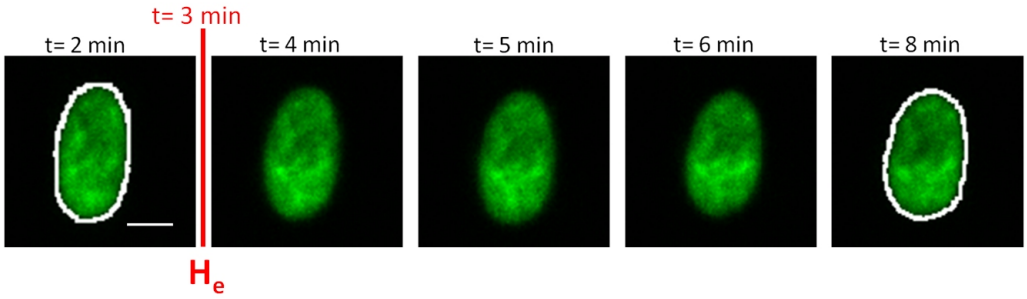

Figure 5.9: Frames from a video showing a NIH3T3 cell nucleus (H2B-GFP green fluorescence), during an experiment. The application of a rotating field ($\mathbf{H}_e$= 50 mT) at t= 3 min affects the morphology of nucleus which becomes less elongated. Cells are imaged for 3 minutes before pinching and for 9 minutes during pinching. The white lines identify the nucleus profile. Scale bar: 5 μm.

The eccentricity of a single nucleus as function of time is reported in Fig.5.10a, where we clearly see that ϵ decreases during pinching. The average eccentricity before pinching is $\epsilon_{BP} = 0.76 \pm 0.01$, while during pinching ϵ_{DP} decreases to 0.72 ± 0.01. ϵ_{DP} is calculated as the average eccentricity between 9 and 12 min from the beginning of the experiment, in order not to take into account the transitory behavior occurring when the magnetic field rotation is turned on. The decrease of the eccentricity indicates that the cell nucleus becomes less elongated when cells are mechanically stimulated.
This nucleus response can be directly evinced also from the optical images (see Fig.5.9) and the same behavior is observed in more than 10 different cells (see Fig.5.10b). Although the initial value of nucleus eccentricity of the cells cultured on magnetic pillars is affected by relevant variability, as also happens when cells are plated on conventional plastic or glass dishes, ϵ always decreases in response to mechanical stimulations.
The relative eccentricity variation $\Delta\epsilon_R = \frac{(\epsilon_{DP} - \epsilon_{BP})}{\epsilon_{BP}}$ is a more robust parameter to properly quantify the effect of mechanical pinching on the nuclear

morphology from a statistical average over data from 10 different cells. The average $\Delta\epsilon_R$ for 10 different cells (Fig.5.10c) is -4.5±1 %, indicating a sizeable decrease of nuclear eccentricity that suggests a reduction of nuclear tension in response to mechanical stimuli.

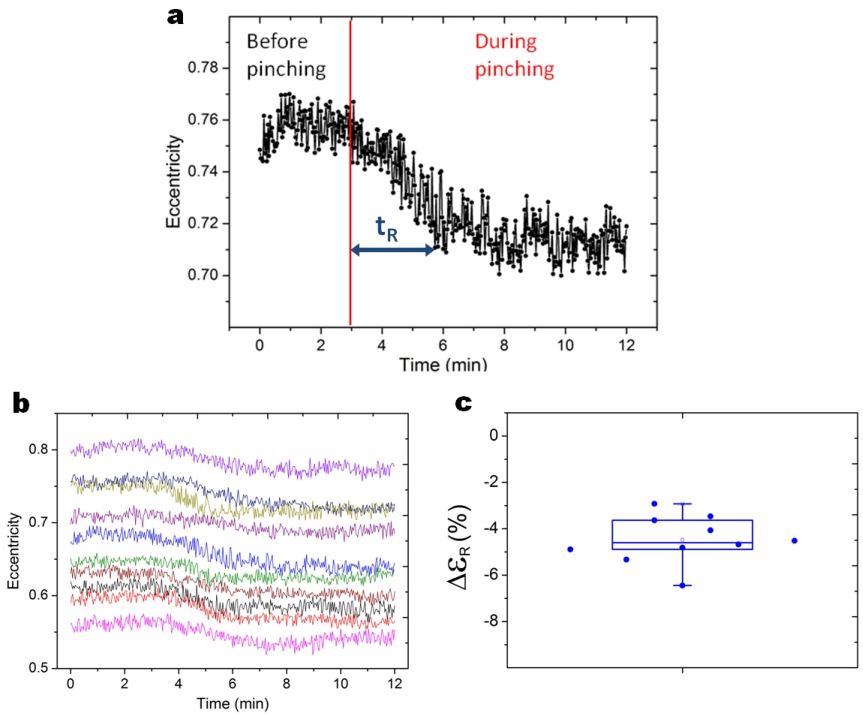

Figure 5.10: **a** Nucleus projected area eccentricity as function of time, before (t= 0-3 min) and during (t= 3-12 min) mechanical pinching. t_R is the response time of the nucleus to a less elongated state. **b** Nucleus eccentricity, as function of time (as in **a**) for a batch of 10 cells. **c** Box plot of the percentage nucleus projected area eccentricity variation $\Delta\epsilon_R = \frac{(\epsilon_{DP}-\epsilon_{BP})}{\epsilon_{BP}}$, where ϵ_{BP} and ϵ_{DP} are respectively the average eccentricity before pinching (t= 0-3 min, see Fig.5.9) and during pinching (t= 9-12 min). $\Delta\epsilon_R$ is calculated for a batch of n= 10 cells. The bottom and top of the box represent the first and third quartiles, whereas the line and small square inside the box represent the median and mean, respectively. The ends of the whiskers correspond to the lowest/highest data point of the distribution.

Moreover, the morphological transition to a less elongated state happens with a specific dynamics (see Fig.5.10a) that can be investigated. In particular, the transition time (t_R) required to the nucleus to adapt its shape upon pinching activation, is calculated.
This transition time can be better extrapolated from the first derivative of the eccentricity. This is shown in see Fig.5.11a, where data are smoothed to evaluate the negative peak width, which corresponds to t_R. In this way the transition time for each nucleus is calculated with an error of ±20 s.

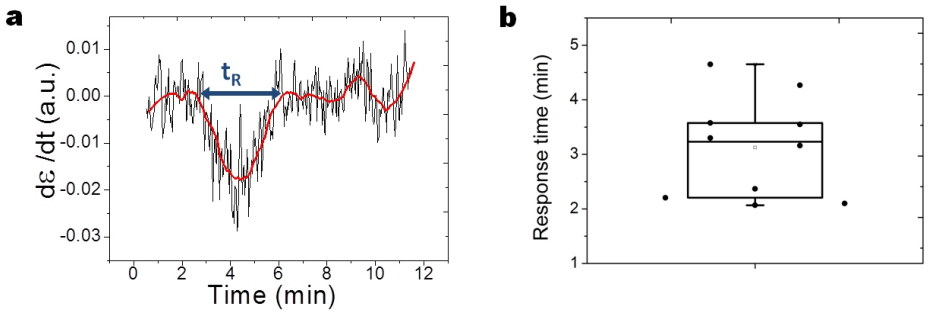

Figure 5.11: **a** Derivative of nucleus projected area eccentricity (dϵ/dt), smoothed with Savitzky-Golay (5 points) to evaluate t_R. **b** Box plot for the transition time (t_R) of the nucleus projected area to a lower eccentricity "quasi stationary state" (see Fig.5.10a), extrapolated by a batch of n= 10 cells. The bottom and top of the box represent the first and third quartiles, whereas the line and small square inside the box represent the median and mean, respectively. The ends of the whiskers correspond to the lowest/highest data point of the distribution.

The transition time for 10 cells is reported in Fig.5.11b, the average value of t_R is 3.1±1.2 min. t_R is much longer than the pinching period (T_P = 10 s), indicating a slow nuclear response to the application of the mechanical stimulus. This suggests that nuclear dynamics is not directly elastically coupled with the mechanical stimuli, while the coupling is mediated by active, slower cellular processes, as will be further investigated in the next sections.
Nevertheless, the results on nuclear morphology demonstrate that cells experience the mechanical stimulation induced by pillars, leading to reproducible

alterations of the nuclear shape. It is worth noting that the cell cytoskeleton could play an important role in the transmission of mechanical signals from the pillars to the nucleus, thus affecting the nuclear shape, as will be discussed in section 5.8.

5.7 Mechanical pinching affects nuclear deformability and histones dynamics

In this section, the effect of mechanical pinching on nucleus dynamics is investigated. First, the way mechanical stimuli induce a dynamic change in nucleus deformability, in terms of nuclear area fluctuations, is explored. Then, the dynamics of H2B core histone, in response to the forces exerted by magnetic pillars, is studied.

5.7.1 Mechanical stimuli alter nucleus deformability

The morphological analysis of the previous section indicates that nucleus adapts to mechanical stimuli. Alterations of nuclear shape are related to a modification in the nucleus-cytoskeleton coupling (see section 1.1)[3]. In particular, a less elongated nucleus denotes a decreased mechanical stress by the cytoskeleton. That could induce changes of nucleus motility and deformability when cells are pinched. In order to investigate this aspect, the effect of the stimulation on nucleus plasticity is evaluated. To this purpose, we study the nuclear area fluctuations, according to a procedure recently developed[21].
Cells are imaged for 30 min without mechanical pinching and for additional 30 min from the application of a rotating $\mathbf{H}_e$ with an acquisition rate of 3 frames per minute. The percentage nuclear area fluctuations (PNAF) are calculated, as the fluctuations from the mean value of nuclei projected area. These PNAF provide information about nucleus plasticity and deformability. The mechanical stimulation induces an enhancement of PNAF (see Fig.5.12a) with respect to the same nucleus before pinching.
To confirm that this is not due to direct effect on the nucleus of the rotating

magnetic field, but driven by pillars mechanical stimuli, we perform an analogous experiment on pillars which are not coated with Fe. No relevant variations of PNAF are observed in that case (see Fig.5.12b), in agreement with the well known insensitivity of cells to uniform quasi-static magnetic fields.

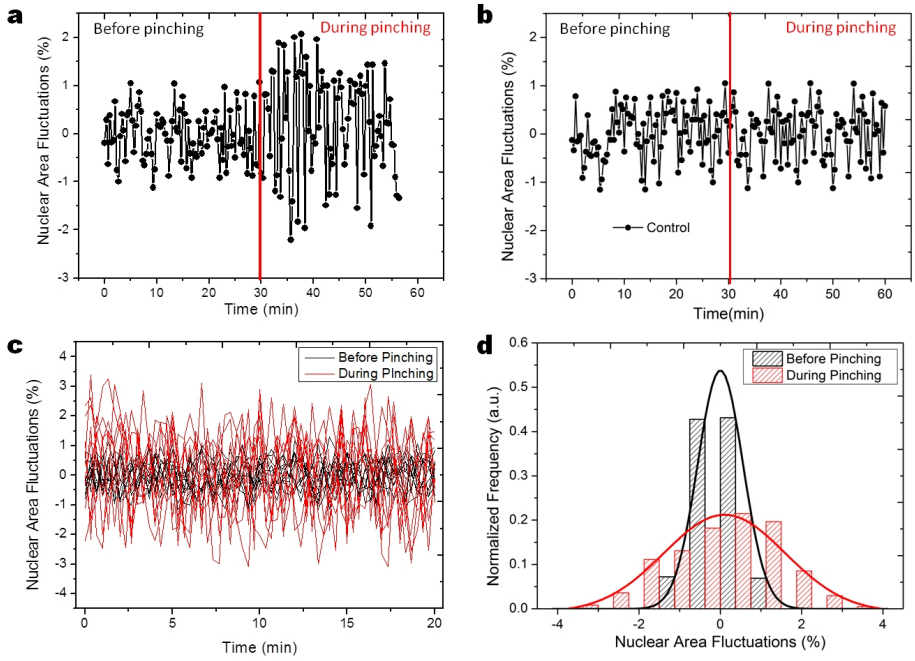

Figure 5.12: **a** Percentage nuclear area fluctuations (PNAF) vs time of a cell before and during pinching. The red line represents the time at which rotation of $\mathbf{H}_e$= 50 mT is turned on. **b** PNAF, as in **a**, but relative to a cell cultured on non-magnetic (without Fe-coating) PDMS micropillars (control measurement). **c** Percentage nuclear area fluctuations (PNAF) vs time of a batch of 10 cells before (black curves) and during pinching (red curves). **d** Black and red histograms represent combined PNAF for 10 cells and all the time points, before and during pinching respectively. The curves represent the Gaussian fittings.

PNAF are calculated for 10 different cells (see Fig.5.12c) and the histogram in Fig.5.12d shows the distribution of fluctuations from the mean, considering all the values at each time point, before (black) and during (red) mechanical pinching.

Data are fitted with a Gaussian curve and the standard deviations are calculated. They represent the average PNAF before (σ_{BP}) and during (σ_{DP}) the stimulation. σ_{BP}= 0.51 % while σ_{DP}= 1.31 %, showing that PNAF becomes more than two time larger when cells are stimulated. Note that, in order to get rid of any transitory effect that can occur when pinching begins, the statistics is related to data acquired 10 min after the field rotation is turned on.

The PNAF analysis demonstrates how cell deformability and nuclear prestress decrease during pinching. As discussed in the previous section, the shape evolution displays a slow dynamics of the nuclear response, over a time scale much longer than the period of the periodic stress applied to the cell, thus suggesting that the effect of mechanical stimulation on the membrane is transferred to the nucleus by active cellular processes, mediated by the cytoskeleton, and not via a direct elastic coupling between pillars and nucleus. To confirm this assumption, the correlation coefficient between normalized nuclear area fluctuations (acquired at 1 fps to precisely capture their oscillations in time) and the mechanical stress arising from pinching (at f_p= 0.1 Hz) are compared. The two curves are plotted in Fig.5.13.

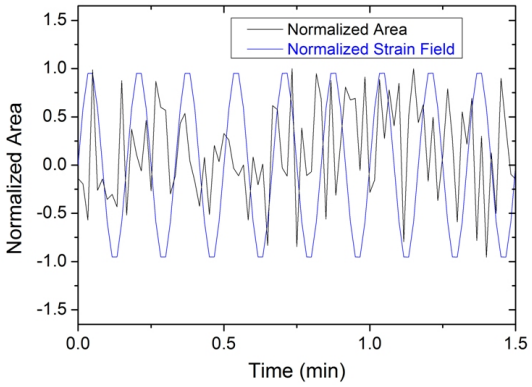

Figure 5.13: Nuclear area fluctuations (normalized to 1) and x-component of the strain field (rescaled between ±1) as function of time. The strain field oscillates at the pinching frequency (f_P= 0.1 Hz).

To understand if a certain correlation occurs between the two curves, the *Pearson* coefficient[128] is calculated and it turns out to be ≈0.05. This

clearly indicates that the two curves are uncorrelated, demonstrating how the nucleus fluctuations are not affected by the strain field oscillating at the pinching frequency, in agreement with a weak elastic coupling between pillars and nucleus.

5.7.2 Mechanically induced changes in H2B histone dynamics

To better understand the impact of periodic pinching on nuclear dynamics, the behavior of H2B core histone is investigated. H2B has been chosen because is one of the most abundant protein binding chromatin and altered H2B dynamics affect nuclear functions (see section 1.1.)
To this scope, H2B images correlation analysis is performed; it is based on a pixel-by-pixel correlation of cell nucleus images. Starting from a reference frame, we acquired images for the following 20 minutes, at 3 frames per minute, and a 2D correlation coefficient (c) between each frame and the reference one is calculated, according to the following equation:

$$c = \frac{\sum_m \sum_n (A_{mn} - \overline{A})(B_{mn} - \overline{B})}{\sqrt{\left(\sum_m \sum_n (A_{mn} - \overline{A})^2\right) \cdot \left(\sum_m \sum_n (B_{mn} - \overline{B})^2\right)}} \tag{5.3}$$

A and B are the two images; they are matrices containing all the pixels (m,n) intensities. $\overline{A}$ and $\overline{B}$ are the average intensity of the two images. The subtraction of the average values ($\overline{A}$ and $\overline{B}$), partially avoid that images correlation is affected by photobleaching occuring during the acquisition.
A is the image of the reference frame and it does not change during the analysis, while B represents the other images at different times. In this way, for each nucleus, the correlation curve (c vs time) is calculated as function of time.

According to this procedure, we evaluate how images are correlated to a reference frame at t = 0 min. Images correlation of nuclei not mechanically pinched (black curve in Fig.5.14a) and pinched (red curve) are compared.

The reference frame (t = 0 min) during pinching is the time point at which rotating $\mathbf{H}_e$ is turned on.
Fig.5.14a shows the correlation coefficient calculated for 10 different nuclei as function of time, while the average value of c is reported in Fig.5.14b.

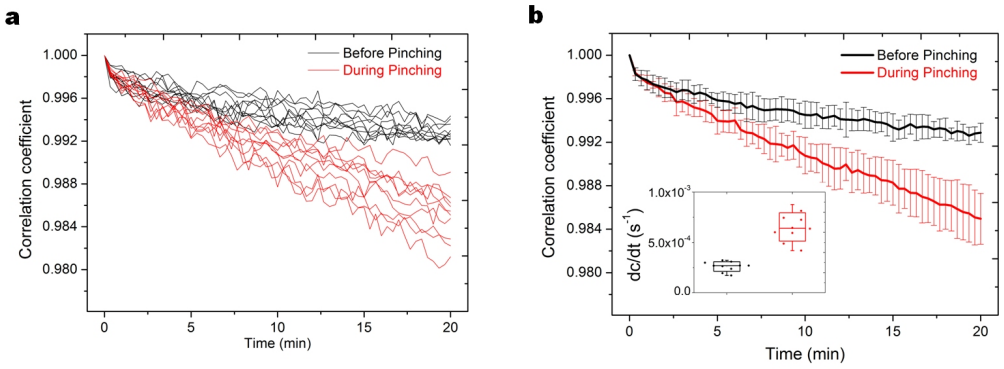

Figure 5.14: **a** Images correlation vs time of H2B-GFP green fluorescent nuclei from the reference frame (at t=0 min), before (black) and during (red) pinching, calculated for 10 cells. The correlation coefficient is calculated according to Equation 5.3, performing a pixel-by-pixel analysis. The reference frames (t=0 min) during pinching corresponds to the time point at which the field rotation ($\mathbf{H}_e$= 50 mT) is turned on. **b** Mean value on 10 cells of the correlation coefficient calculated in **a**, as function of time. Error bars represent the standar deviations from the mean. The inset shows box plots for the linear fitting of images correlation coefficient slopes $|dc/dt|$, calculated for 10 cells, before (black) and during (red) pinching.

An enhancement in H2B images de-correlation is observed during pinching. The absolute value of the slope of the de-correlation coefficient, $|dc/dt|$ (see the inset in Fig.5.14b) is around 2.6 times larger during pinching, indicating a relevant increase in H2B images de-correlation. Noteworthy, the de-correlation curve during pinching is still decreasing in a linear way after 20 min, with a larger slope compared to non-pinched case. This suggests a persisting more dynamic behavior of nucleus during stimulation.

Note also that a higher variability of $|dc/dt|$ with respect to the mean values is seen during pinching (see inset in Fig.5.14b), in agreement with the overall enhancement of nuclear dynamics induced by pinching.
To correctly interpret H2B images correlation analysis, we have to take into account two different de-correlation sources: (i) changes in the nuclear morphology and (ii) variation of the H2B intensity distribution inside the nucleus. This analysis does not allow to distinguish the two contributions. However, it would be crucial to proper investigate the H2B dynamics inside the nucleus, as alterations in H2B turnover on chromatin affect cell genomic functions.
To this scope, we performed FRAP (Fluorescence recovery after photobleaching) analysis. The procedure consists in studying the fluorescence recovery in a certain area of the nucleus (a circle with a diameter of 4 μm), after photobleaching of that region with high laser intensity (see Fig.5.15).

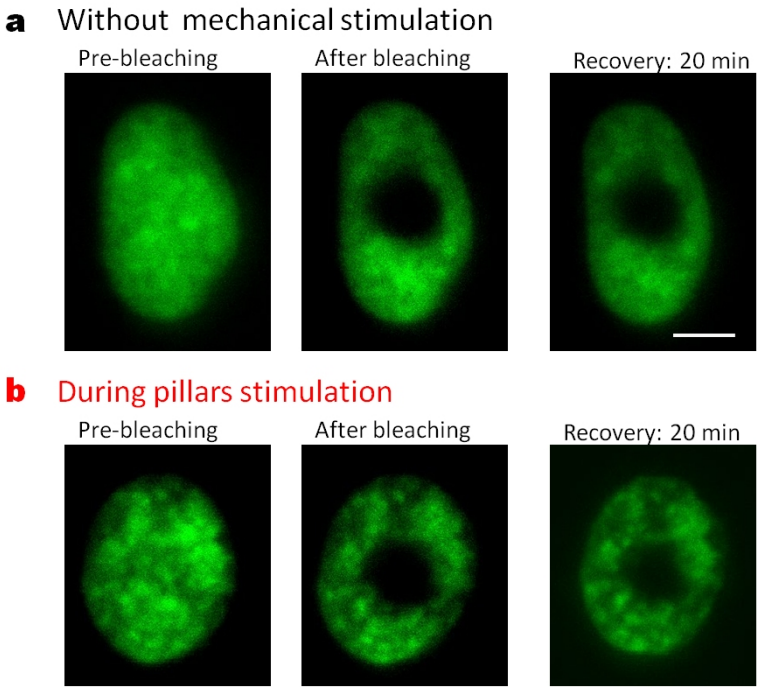

Figure 5.15: Frames showing H2B-GFP fluorescence intensity upon photobleaching and recovery, without and with mechanical pinching of cells. The bleached ROI is a circle with a diameter of 4 μm. Scale bar: 5 μm.

Images are acquired at 12 frames per minute during the first 5 minutes to capture the fast dynamics of the fluorescence recovery and then for 20 minutes at 3 frames per minute.
Fluorescence intensity in the photobleached region is computed at each time frame, before and after photobleaching. The obtained intensity is normalized according to:

$$I_{norm}(t) = \frac{I(t) - I_B}{I_{pre-bleach} - I_B} \cdot \frac{T_{pre-bleach} - I_B}{T(t) - T_B} \tag{5.4}$$

where $I_{norm}(t)$ is the normalized intensity, $I(t)$ is the effective intensity in the bleached area and I_B is the background. $I_{pre-bleach}$ is the average intensity before photobleaching in the bleached region. The first factor in the equation allows to calculate the recovery fraction, normalizing $I(t)$ to the initial value and rescaling it between 0 and 1. The extent of fluorescence recovery in FRAP experiments is generally underestimated due the overall bleaching of the cell. To correct for this (see the second factor in the equation), we evaluate the total intensities of the whole nucleus as function of time $T(t)$, and the intensity of the whole nucleus before bleaching $T_{pre-bleach}$. The intensity of the bleached region is normalized by the one of the entire nucleus to obtain the actual recovery fraction.

We extrapolated the normalized intensity in the bleached nuclear area, both in cells stimulated by pinching and in control cells without stimulation (see Fig.5.15).
The recovery fraction, reported in Fig.5.16, is the average calculated on 10 different nuclei which are imaged for 25 minutes after bleaching. It clearly indicates an increase in the fluorescence recovery during pinching. This fact demonstrates that an enhancement of H2B dynamics occurs, when cells are mechanically stimulated. In particular, the fluorescence recovery is faster (during pinching) in the first 2 min after bleaching, indicating a higher diffusivity of H2B inside the nucleus and thus suggesting that mechanical stimulation leads to a reduction of nucleus viscosity.
This result is relevant because an enhancement of H2B dynamics clearly indicates that cells actively respond to the stimuli exerted by magnetic pillars, thus inducing an alteration of genomic functions. In the next section, we

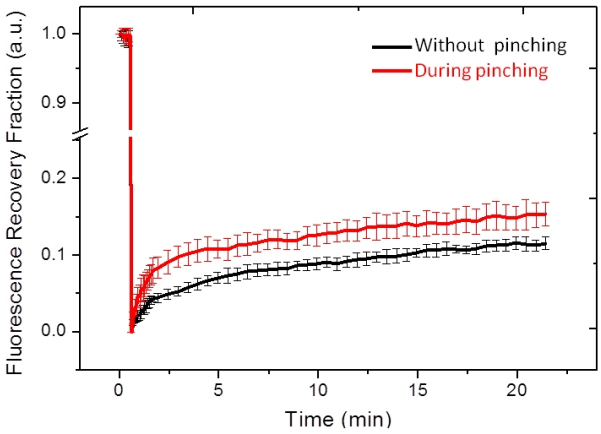

Figure 5.16: Fluorescence recovery curves for nuclear H2B-GFP signal, without (black) and with (red) the application of mechanical stimuli, activated by a rotating $\mathbf{H}_e$= 50 mT

focus on the mechanisms which allow the transmission of the forces from pillars to the nucleus, studying how cytoskeleton responds to mechanical stimuli induced by magnetic pillars.

5.8 Magnetic pillars induce actin reorganization

So far, it is shown that the periodic mechanical stimulation exerted by magnetic pillars affects both nuclear morphology and H2B dynamics. In this section, the effect of such stimuli on the cell cytoskeleton, which is responsible of forces transmission from pillars to the nucleus, is investigated. In particular the dynamics of actin, one of the most abundant proteins in the cytoskeleton, are studied.

Fig.5.17 shows a cell transfected with RFP-Lifeact and imaged for 20 minutes before pinching and for additional 20 minutes after turning on $\mathbf{H}_e$ rotation. The images show that the cell geometry changes more significantly

during pinching (t= 20-40 min), while it is less dynamic before pinching (t= 0-20 min).

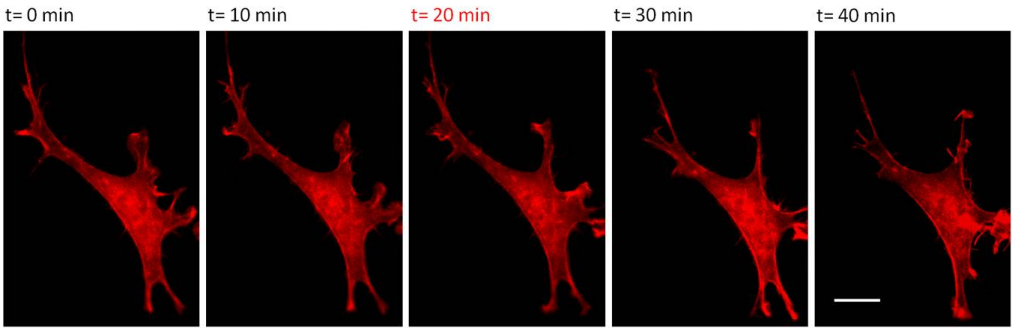

Figure 5.17: Frames from a video showing a NIH3T3 cell (RFP-Lifeact red fluorescence) cultured on magnetic pillars, during an experiment. Cell is imaged for 40 minutes, before (0-20 min) and during (20-40 min) mechanical pinching. Scale bar: 20 μm.

To demonstrate that cell cytoskeleton is affected by the mechanical stimuli, actin images correlation before and during pinching are evaluated.
With a similar procedure to that used for H2B images correlation, a pixel-by-pixel analysis is performed, calculating the correlation coefficient (see the previous section) as function of time. The reference frames are the one at t= 0 min (see Fig.5.17) for non-stimulated cells, and the one at t=20 min when pinching begins.
The correlation coefficient is calculated for 10 different cells (see Fig.5.18a) and the average value is plotted in Fig.5.18b. To quantify the changes in the correlation before and during pinching, a linear fit for the correlation coefficients of each cell is performed. The absolute value of fitting lines slope, $|dc/dt|$ (see the inset in Fig.5.18b) is around two times higher during pinching, indicating a relevant increase in actin images de-correlation. This enhancement demonstrates that the mechanical stimuli exerted by pillars induce faster actin dynamics, confirming that cell cytoskeleton is affected by such a stimulation, thus acting as a mediator of the mechanical stimulus transmission toward the nucleus.

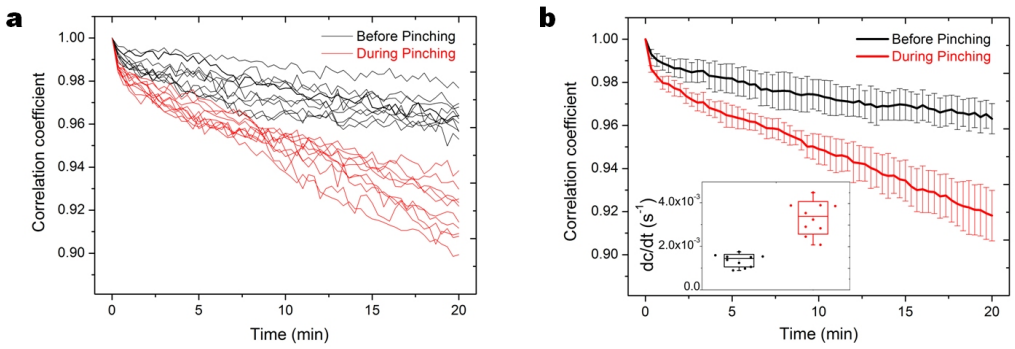

Figure 5.18: **a** Images correlation vs time of RFP-Lifeact red fluorescent cells, before (black) and during (red) pinching, calculated for 10 cells. The correlation coefficient is calculated according to Equation 5.3, performing a pixel-by-pixel analysis. The reference frame during pinching corresponds to the time point at which the field rotation ($\mathbf{H}_e$= 50 mT) is turned on. **b** Mean value on 10 cells of the correlation coefficient calculated in **a**, as function of time. Error bars represent the standard deviations from the mean. The inset shows box plots for the linear fitting of images correlation coefficient slopes $|dc/dt|$, calculated for 10 cells, before (black) and during (red) pinching.

In the next section, to conclude the biological validation of magnetic pillars, the MKL transcription factor translocation in response to mechanical stimuli is investigated.

5.9 MKL transcription cofactor translocation

The more convincing proof of the link between the mechanical stimulation, induced by magnetic pillars, and alterations of cellular and nuclear dynamics, is provided by the investigation of MKL transcription cofactor translocation. MKL is located both in the nucleus and the cytoplasm and can shuttle between the two in response to mechanical stimuli, thus bringing about alterations in gene transcription.
Moreover, recent studies have demonstrated how the actin configuration is also related to MKL translocation[25][26]. In particular, when MKL shuttles to the nucleus, actin polymerizes in long fibers, while a translocation to the

cytoskeleton is associated with actin de-polymerization.
Cells transfected with mCherry MKL are imaged before the mechanical stimulation and after 30 min from the application of the mechanical pinching. The images in Fig.5.19a are the result of an average intensity projection of z-series, before and during pinching. They show how MKL cofactor moves outside the nucleus in response to the mechanical stimuli, as the intensity decreases in the nucleus and increases in the cytoplasm.

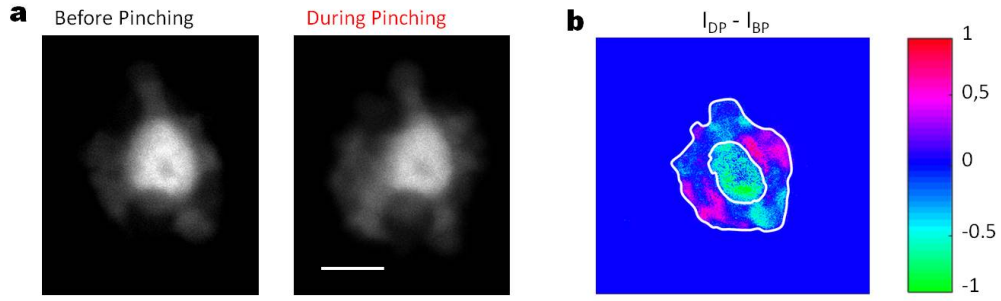

Figure 5.19: **a** Optical images showing mCherry-MKL signal in the cell nucleus and cytoskeleton, before and during the mechanical stimulation. The rotating field ($\mathbf{H}_e$= 50 mT) is applied for 30 min before the acquisition of the second frame. **b** Color map of MKL signal, obtaining by the subtraction of the intensity during (I_{DP}) and before (I_{BP}) pinching. Scale bar: 20 μm.

For a better visualization of such translocation, a subtraction of the intensity during and before pinching ($I_{DP} - I_{BP}$) is performed (see Fig.5.19b). It results in a clear negative value inside the nucleus (MKL signal decreases), while an average increase inside cytoplasm is observed.
To properly quantify the MKL signal the intensity is calculated for each cell, as the average of 5 different circular regions of interest with a diameter of 2 μm, both in the nucleus and cytoplasm. In this way, the average MKL intensity before and during the mechanical pinching is extrapolated. Finally, the relative intensity I_{DP}/I_{BP} for 10 different cells is calculated and it is shown in Fig.5.20.
The results indicate an enhancement of the relative intensity in the cytoplasm (mean I_{DP}/I_{BP}= 1.19) and a decrease in the nucleus (mean I_{DP}/I_{BP}= 0.83)

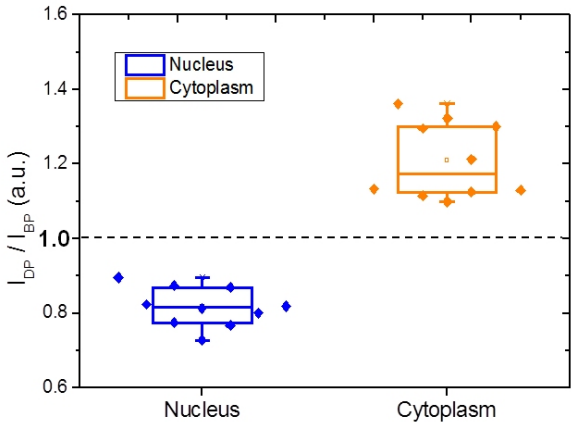

Figure 5.20: Box plots for the MKL relative intensity, calculated as the ratio between the intensity during and before pinching (I_{DP}/I_{BP}) for 10 cells, respectively in the nucleus (blue) and cytoplasm (orange).

when cells are pinched, demonstrating MKL translocation outside the nucleus.
This result further confirms that forces arising from magnetic pillars have an effect on nuclear dynamics that can lead to changes in the gene expression pattern. Moreover, it suggests that actin de-polymerization occurs in response to mechanical stimuli. It is worth noting that this analysis does not directly allow to understand if actin de-polymerization is a consequence of changes in nuclear dynamics or vice-versa. However, the results on MKL translocation are in agreement with the observations on nuclear morphology and deformability, as a less elongated an more dynamic nucleus is associated to a reduction of the stress induced by the cytoskeleton.

5.10 Conclusions

In this chapter, a novel device based on Fe-coated PDMS micropillars has been presented. It allows to exert controlled mechanical stimuli on single cells cultured on top of them. These magnetic pillars, actuated by a uniform external magnetic field, exert a combination of attractive and repulsive forces. These forces induce pillars bending, thus producing mechanical stim-

uli localized in different points of the cell membrane.
The simulated magnetic forces are in the order of tens nN, tunable in intensity with the external magnetic field.
Moreover, pillars bending is measured, as the variation between pillars centers distances upon the application of $\mathbf{H}_e$; deflections up to ≈600 nm from the rest position are found. These deflections are compared with values calculated from an elastic model of pillars, according to the forces previously simulated; a good agreement between experiments and simulations is obtained.
For the peculiar geometry of repeated groups of 4 pillars, a rotating external field allows to simultaneously actuate all the groups, both in the horizontal and vertical direction, producing a periodic biaxial strain field, resulting in continuous local cell pinching. The time behavior of such stimuli is controlled by the rotation of $\mathbf{H}_e$, allowing for a tunable pinching frequency.
The potential of this technique has been demonstrated, showing how the stimuli arising by magnetic pillars at a fixed pinching frequency of 0.1 Hz induce changes in nuclear morphology, deformability and H2B dynamics. In addition, it is shown how (at the pinching frequency) the nucleus response is not elastically coupled with pillars induced stimuli, but active cellular processes play a role in the transmission of forces from cell membrane to the nucleus.
To this purpose, the demonstration that pillars induce actin reorganization is provided and finally the MKL transcription cofactor translocation from the nucleus to the cytoskeleton is shown, thus suggesting that pillars affect actin dynamics and induce changes in genomic functions. As a future perspective, the perturbation of cells by altering the cytoskeletal-link or the physical properties of the nucleus (e.g. lamin perturbation), will allow for a deeper comprehension of the connections between the aforementioned cellular and nuclear responses.
To our knowledge, this is the first example of a biocompatible and properly microengineered technique for cell investigation which allows the application of mechanical stimuli in different points of the plasma membrane with tunable mechanical stress intensity and frequency, to mimic the forces exerted by the cellular matrix. This method constitutes a new enabling technology for

the development of a new route in mechanobiology: the quantitative investigation of the dynamical cell response to time-dependent mechanicals stimuli applied to sub-cell compartments.

Chapter 6

Conclusions

In this thesis work, two novel devices for mechanobiology studies on single cells have been presented: magnetic Domain Wall Tweezers (DWTs) and magnetically actuated micropillars. Currently used methods for investigating the single cell response to mechanical stimuli are still at their infancy (see section 1.2).
In particular, there is a growing need of techniques, both biocompatible and that can be easily integrated with conventional setups for cell investigation, allowing for the application of highly localized and precisely controlled forces at cellular and subcellular level.
Moreover, currently used techniques for mechanobiology studies do not allow to apply inhomogeneous and prolonged forces on several points of the cell membrane, thus mimicking those arising from the extracellular matrix.
The devices presented in this thesis aim to overcome the aforementioned limitations.
To this scope, an on-chip platform based on magnetic domain wall tweezers (DWTs), allowing the application of finely localized forces on target cells, has been developed. The potential of this technique has been demonstrated manipulating 1 μm superparamagnetic beads in a cell culture environment. Particles are brought in contact with the HeLa cell membrane, where can exert a magnetic force in the order of hundreds of pN. Such a mechanical stimulus produces a local deformation of the cellular membrane, which has been precisely quantified. This is a fundamental step towards the exploitation

of DWTs as integrated and fully biocompatible tool suitable for the application of localized mechanical stimuli. It is noteworthy that the manipulation is actuated via quasi-static and non-invasive magnetic fields. Moreover, it allows an easy integration with systems using confocal microscopy, suitable for sophisticated real-time investigation of the cell functionality, in response to applied mechanical stimuli.

With this approach, precise quantification of forces applied to the cell can be performed via micromagnetic simulations, using as input parameters only the actual bead position with respect to the DW in the conduit. In perspective, the system can be integrated using dedicated software which calculates the mechanical stimuli strength in real time, thus providing biologists with a quantitative tool for the application of localized forces. Furthermore, we also demonstrated the possibility to manipulate microinjected magnetic nanoparticles inside the cell cytoplasm, paving the way to the direct mechanical stimulation of cell sub-compartments and organelles (e.g. nucleus).

The second device, based on magnetic micropillars, provides a new and exciting opportunity to apply multiple forces on different points of the cell membrane, thus mimicking the mechanical stimulation from extra-cellular matrix. In this thesis, we have shown that this technology allows to investigate cell and nuclear dynamics, thanks to the possibility to apply localized and prolonged cell pinching that can be tuned, both in frequency and intensity. The cell response at a fixed pinching frequency of 0.1 Hz has been investigated, demonstrating how this pinching induces changes in nuclear morphology, deformability and H2B dynamics. These studies revealed that the nuclear mechanical response to small external forces does not result from a purely elastic coupling between the cell membrane and the nucleus, but involves active cellular processes.

Indeed, we have observed an enhancement in actin dynamics during stimulation, demonstrating that it plays a role in the transmission of forces from the pillars to the nucleus. Finally, translocation of MKL transcription cofactor from the nucleus to the cytoplasm is observed in response to mechanical stimuli, showing that local pinching can influence gene expression.

To summarize we have demonstrated the potential of magnetic micro-pillars, as a novel approach to the study of cellular mechano-transduction in diverse

functional contexts. Noteworthy, the controlled modulation of extracellular microenvironment achievable with our platform could open new routes in mechanobiology, enabling a better understanding of the coupling between local external forces and intracellular biochemical pathways regulating cellular functions.

Appendix A: Mathematical model of lateral indentation of the cell membrane

The mathematical problem of determining the cell deformation under the action of a distributed load imposed by the beads' cluster is considered[101][1]. Since the observed overall displacement in experiments is small compared to the cell diameter, the external forces are mainly counterbalanced by the bending of the cell membrane, which is considered as a linear elastic shell of thickness h, with Young modulus E and Poisson ration ν.
Accordingly, the cell membrane has a bending stiffness $K_b = \frac{Eh^3}{12(1-\nu^2)}$ and a stretching stiffness $K_s = E \cdot h$. This assumption is valid if we consider a range of applied forces much bigger that the rupture load of a focal adhesion with the substrate, which is in the order of 30 pN[129].
Considering a Cartesian coordinate system (x, y) for describing the material position of the doubly-curved cell membrane, its local principal radii of curvature are indicated by $\rho_\alpha = \rho_\alpha(x, y)$ with $\alpha = (x, y)$. Applying an indentation distributed pressure $p = p(x, y)$ in the z-direction, the linearised equilibrium equations using the theory of thin shallow shells read[123]:

$$K_b \nabla^4 \omega + \nabla_g \phi = p \tag{6.1}$$

$$K_s^{-1} \nabla^4 \phi - \nabla_g^2 \omega = 0 \tag{6.2}$$

[1]This appendix includes text previously published in the supporting information of the following article: *M. Monticelli et al.* "Magnetic domain wall tweezers: a new tool for mechanobiology studies on individual target cells", *Lab on a chip*, 2016, 7, 16, pp 2882-90. Reproduced with permission.

where ∇^2 is the Laplacian operator, $\nabla_g^2(.) = \frac{(.),xx}{\rho_x} + \frac{(.),yy}{\rho_y}$ is the Vlasov operator, comma denotes partial derivative, $\omega = \omega(x, y)$ is the vertical shell displacement, and $\phi = \phi(x, y)$ is the Airy stress function, whose derivatives yield the planar stresses. Eqs.(1,2) are valid within the limit $\epsilon = h/R << 1$, with $R = min[\rho_x, \rho_y]$, and represent a system of partial differential equations whose solution is strongly affected by the shell geometry. Such a geometric dependence can be highlighted by considering the dimensionless variables $\bar{\omega} = (\omega\ K_b)/(P\ R^2), \bar{\phi} = (\phi\ h^2)/(P\ R^3)$ where P is the characteristic intensity of the force exerted by the beads. Accordingly, combing the two Eq.1-2, we get:

$$\epsilon^2 \nabla^8 \omega + \nabla_g^4 \omega = \epsilon^2 \nabla^4 p \tag{6.3}$$

where we considered dimensionless operators over the coordinates $\bar{x} = x/R$ and $\bar{y} = y/R$, dropping the bars for the sake of simplicity. Eq.(3) is a singularly perturbed linear partial differential equation which is valid far enough from the indenting region. Since ϵ is a very small parameter, the leading order solutions for the far-field displacements depends primarily on the Gaussian curvature of the cell surface[119].

The complete solution could be derived by imposing the matching between this far-field solution and the one found with asymptotic expansion around the indentation area. Nonetheless, since the cell membrane is a doubly curved surface with positive Gaussian curvature everywhere, Eq.(3) is governed by the elliptic operator ∇_g^2 at the leading order, meaning that the corresponding solution is concentrated around the indentation area and decays quickly away from it. In such a case, the shell easily buckles, eventually reaching a partly inverted shape around the indentation area, as well known from classical studies on spherical caps[122].

Therefore, the large deflections (i.e. with respect to h, being of the order R) of the cell membrane under the indentation pressure exerted by the beads' cluster will be calculated by searching for an elastic solution within the constraint of isometric transformations. The shape of the cell membrane in proximity of the first contact point C with the cluster can be approximated by the osculating ellipsoidal paraboloid, having the expression :

$$z = \frac{x^2}{2R_x} + \frac{y^2}{2R_y} \tag{6.4}$$

where the (x,y) plane is tangent to C having directions coinciding with the principal direction of the surface, locally characterized by curvature radii R_x and R_y. If 2δ is the large indentation provoked by the cluster, we assume that the deformed shape of the cell membrane will be given be reversing the shape of the paraboloid with respect to the plane at $z = \delta$, producing a mirror-buckling with a boundary ellipse having semi-axes $s_x = \sqrt{2\delta R_x}$ and $s_y = \sqrt{2\delta R_y}$. Let us now consider calculate the resulting indentation value using a variational approach. After lengthy manipulations, the total deformation energy U of the shell in such a buckled configuration reads:

$$U = \frac{c\pi E}{12^{3/4}(1-\nu^2)} h^{5/2} (2\delta)^{3/2} \left(\frac{1}{R_x} + \frac{1}{R_y} \right) \tag{6.5}$$

where $c = 1{:}15$ is a constant obtained by minimizing a certain displacement functional under a nonholonomic constraint[124].
The work L of external forces is instead given by:

$$L = 2\delta F_c \tag{6.6}$$

for a concentrated force F, or:

$$L = 2\pi \sqrt{R_x R_y} P(\delta_p^2 + 2(h - \delta_p)\delta_p) \tag{6.7}$$

for a pressure P distributed over $z <= h_p$, with an elliptic boundary having semi-axes $a = \sqrt{2R_x\delta_p}$ and $b = \sqrt{2R_y h_p}$, corresponding to a distributed indentation force $F_d = 2P\delta_p\sqrt{R_x R_y}$.
Accordingly, the analytic relation between load and indentation can be found by minimizing the elastic functional $W = U - L$, being:

$$F_c = \frac{3c\pi E}{12^{3/4}2(1-\nu^2)} h^{5/2} (2\delta)^{1/2} \left(\frac{1}{R_x} + \frac{1}{R_y} \right) \tag{6.8}$$

$$F_d = \frac{3c\pi E}{12^{3/4}(1-\nu^2)} h^{5/2} \frac{(2\delta)^{1/2}}{2(2-\beta)} \left(\frac{1}{R_x} + \frac{1}{R_y} \right) \tag{6.9}$$

where $\beta = \delta_p/\delta < 1$ indicates the portion of the free boundary where the pressure is applied.

Bibliography

[1] J. S. Lee, C. M. Hale, P. Panorchan, S. B. Khatau, J. P. George, Y. Tseng, C. L. Stewart, D. Hodzic, and D. Wirtz, "Nuclear Lamin A/C Deficiency Induces Defects in Cell Mechanics, Polarization, and Migration," *Biophysical Journal*, vol. 93, no. 7, pp. 2542–2552, 2007.

[2] S. B. Khatau, R. J. Bloom, S. Bajpai, D. Razafsky, S. Zang, A. Giri, P. H. Wu, J. Marchand, A. Celedon, C. M. Hale, S. X. Sun, D. Hodzic, and D. Wirtz, "The distinct roles of the nucleus and nucleus-cytoskeleton connections in three-dimensional cell migration," *Scientific Reports*, vol. 2, 2012.

[3] P. Roca-Cusachs, J. Alcaraz, R. Sunyer, J. Samitier, R. Farré, and D. Navajas, "Micropatterning of Single Endothelial Cell Shape Reveals a Tight Coupling between Nuclear Volume in G1 and Proliferation," *Biophysical Journal*, vol. 94, no. 12, pp. 4984–4995, 2008.

[4] N. Jain, K. V. Iyer, A. Kumar, and G. V. Shivashankar, "Cell geometric constraints induce modular gene-expression patterns via redistribution of HDAC3 regulated by actomyosin contractility," *Proceedings of the National Academy of Sciences*, vol. 110, no. 28, pp. 11349–11354, 2013.

[5] J. Wolff, *Das Gesetz der Transformation der Knochen.* Pro Business, 2010.

[6] T. Iskratsch, H. Wolfenson, and M. P. Sheetz, "Appreciating force and shape: the rise of mechanotransduction in cell biology," *Nature Reviews Molecular Cell Biology*, vol. 15, no. 12, pp. 825–833, 2014.

[7] B. N. Kholodenko, "Cell-signalling dynamics in time and space," *Nature Reviews Molecular Cell Biology*, vol. 7, no. 3, pp. 165–176, 2006.

[8] G. P. Chrousos, "Organization and Integration of the Endocrine System: The Arousal and Sleep Perspective," *Sleep Medicine Clinics*, vol. 2, no. 2, pp. 125–145, 2007.

[9] H. F. Lodish, *Molecular cell biology*. W.H. Freeman, 2000.

[10] C.-M. Lo, H.-B. Wang, M. Dembo, and Y.-l. Wang, "Cell Movement Is Guided by the Rigidity of the Substrate," *Biophysical Journal*, vol. 79, no. 1, pp. 144–152, 2000.

[11] N. Wang, J. Butler, and D. Ingber, "Mechanotransduction across the cell surface and through the cytoskeleton," *Science*, vol. 260, no. 5111, pp. 1124–1127, 1993.

[12] Y. Shao and J. Fu, "Integrated micro/nanoengineered functional biomaterials for cell mechanics and mechanobiology: A materials perspective," *Advanced Materials*, vol. 26, no. 10, pp. 1494–1533, 2014.

[13] P. S. Dittrich and A. Manz, "Lab-on-a-chip: microfluidics in drug discovery," *Nature Reviews Drug Discovery*, vol. 5, no. 3, pp. 210–218, 2006.

[14] G. Y. H. Lee and C. T. Lim, "Biomechanics approaches to studying human diseases," *Trends in Biotechnology*, vol. 25, no. 3, pp. 111–118, 2007.

[15] Y. Park, M. Diez-Silva, G. Popescu, G. Lykotrafitis, W. Choi, M. S. Feld, and S. Suresh, "Refractive index maps and membrane dynamics of human red blood cells parasitized by Plasmodium falciparum.," *Proceedings of the National Academy of Sciences of the United States of America*, vol. 105, no. 37, pp. 13730–13735, 2008.

[16] D. A. Fedosov, B. Caswell, S. Suresh, and G. E. Karniadakis, "Quantifying the biophysical characteristics of Plasmodium-falciparum-parasitized red blood cells in microcirculation," *Proceedings of the National Academy of Sciences*, vol. 108, no. 1, pp. 35–39, 2011.

[17] S. E. Cross, Y.-S. Jin, J. Rao, and J. K. Gimzewski, "Nanomechanical analysis of cells from cancer patients," *Nature Nanotechnology*, vol. 2, no. 12, pp. 780–783, 2007.

[18] A. J. Engler, S. Sen, H. L. Sweeney, and D. E. Discher, "Matrix Elasticity Directs Stem Cell Lineage Specification," *Cell*, vol. 126, no. 4, pp. 677–689, 2006.

[19] K. A. Kilian, B. Bugarija, B. T. Lahn, and M. Mrksich, "Geometric cues for directing the differentiation of mesenchymal stem cells," *Proceedings of the National Academy of Sciences*, vol. 107, no. 11, pp. 4872–4877, 2010.

[20] S. M. Mccormick, J. J. Mao, and G. C. Reilly, "Shear stress induces osteogenic differentiation of human mesenchymal stem cells," *Regenerative Medicine*, vol. 5, no. 5, pp. 713–724, 2010.

[21] E. Makhija, D. S. Jokhun, and G. V. Shivashankar, "Nuclear deformability and telomere dynamics are regulated by cell geometric constraints," *Proceedings of the National Academy of Sciences*, vol. 113, no. 1, pp. E32–E40, 2016.

[22] M. Gupta, B. R. Sarangi, J. Deschamps, Y. Nematbakhsh, A. Callan-Jones, F. Margadant, R.-M. Mège, C. T. Lim, R. Voituriez, and B. Ladoux, "Adaptive rheology and ordering of cell cytoskeleton govern matrix rigidity sensing," *Nature Communications*, vol. 6, no. May, p. 7525, 2015.

[23] A. Zemel, F. Rehfeldt, A. E. X. Brown, D. E. Discher, and S. A. Safran, "Optimal matrix rigidity for stress-fibre polarization in stem cells," *Nature Physics*, vol. 6, no. 6, pp. 468–473, 2010.

[24] M. Piast, I. Kustrzeba-Wójcicka, M. Matusiewicz, and T. Banaś, "Molecular evolution of enolase," *Acta Biochimica Polonica*, vol. 52, no. 2, pp. 507–513, 2005.

[25] K. V. Iyer, S. Pulford, A. Mogilner, and G. V. Shivashankar, "Mechanical activation of cells induces chromatin remodeling preceding MKL

nuclear transport," *Biophysical Journal*, vol. 103, no. 7, pp. 1416–1428, 2012.

[26] F. Miralles, G. Posern, A. I. Zaromytidou, and R. Treisman, "Actin dynamics control SRF activity by regulation of its coactivator MAL," *Cell*, vol. 113, no. 3, pp. 329–342, 2003.

[27] S. Dupont, L. Morsut, M. Aragona, E. Enzo, S. Giulitti, M. Cordenonsi, F. Zanconato, J. Le Digabel, M. Forcato, S. Bicciato, N. Elvassore, and S. Piccolo, "Role of YAP/TAZ in mechanotransduction," *Nature*, vol. 474, no. 7350, pp. 179–183, 2011.

[28] S. Piccolo, S. Dupont, and M. Cordenonsi, "The Biology of YAP/TAZ: Hippo Signaling and Beyond," *Physiological Reviews*, vol. 94, no. 4, pp. 1287–1312, 2014.

[29] B. C. Low, C. Q. Pan, G. V. Shivashankar, A. Bershadsky, M. Sudol, and M. Sheetz, "YAP/TAZ as mechanosensors and mechanotransducers in regulating organ size and tumor growth," *FEBS Letters*, vol. 588, no. 16, pp. 2663–2670, 2014.

[30] D. A. Fletcher and R. D. Mullins, "Cell mechanics and the cytoskeleton," *Nature*, vol. 463, no. 7280, pp. 485–492, 2010.

[31] C. P. Brangwynne, F. C. MacKintosh, S. Kumar, N. A. Geisse, J. Talbot, L. Mahadevan, K. K. Parker, D. E. Ingber, and D. A. Weitz, "Microtubules can bear enhanced compressive loads in living cells because of lateral reinforcement," *Journal of Cell Biology*, vol. 173, no. 5, pp. 733–741, 2006.

[32] H. Herrmann, H. Bär, L. Kreplak, S. V. Strelkov, and U. Aebi, "Intermediate filaments: from cell architecture to nanomechanics," *Nature Reviews Molecular Cell Biology*, vol. 8, no. 7, pp. 562–573, 2007.

[33] Y. B. Tzur, K. L. Wilson, and Y. Gruenbaum, "SUN-domain proteins: 'Velcro' that links the nucleoskeleton to the cytoskeleton," *Nature Reviews Molecular Cell Biology*, vol. 7, no. 10, pp. 782–788, 2006.

[34] D. Rajgor and C. M. Shanahan, "Nesprins: from the nuclear envelope and beyond," *Expert Reviews in Molecular Medicine*, vol. 15, no. July, p. e5, 2013.

[35] N. Wang, J. D. Tytell, and D. E. Ingber, "Mechanotransduction at a distance: mechanically coupling the extracellular matrix with the nucleus," *Nature Reviews Molecular Cell Biology*, vol. 10, no. 1, pp. 75–82, 2009.

[36] J. T. Morgan, E. R. Pfeiffer, T. L. Thirkill, P. Kumar, G. Peng, H. N. Fridolfsson, G. C. Douglas, D. A. Starr, and A. I. Barakat, "Nesprin-3 regulates endothelial cell morphology, perinuclear cytoskeletal architecture, and flow-induced polarization," *Molecular Biology of the Cell*, vol. 22, no. 22, pp. 4324–4334, 2011.

[37] Q. Zhang, "Nesprin-2 is a multi-isomeric protein that binds lamin and emerin at the nuclear envelope and forms a subcellular network in skeletal muscle," *Journal of Cell Science*, vol. 118, no. 4, pp. 673–687, 2005.

[38] I. Solovei, A. S. Wang, K. Thanisch, C. S. Schmidt, S. Krebs, M. Zwerger, T. V. Cohen, D. Devys, R. Foisner, L. Peichl, H. Herrmann, H. Blum, D. Engelkamp, C. L. Stewart, H. Leonhardt, and B. Joffe, "LBR and lamin A/C sequentially tether peripheral heterochromatin and inversely regulate differentiation," *Cell*, vol. 152, no. 3, pp. 584–598, 2013.

[39] E. A. Booth-Gauthier, T. A. Alcoser, G. Yang, and K. N. Dahl, "Force-induced changes in subnuclear movement and rheology," *Biophysical Journal*, vol. 103, no. 12, pp. 2423–2431, 2012.

[40] "https://www.mechanobio.info/what-is-mechanobiology."

[41] E. Meshorer, D. Yellajoshula, E. George, P. J. Scambler, D. T. Brown, and T. Misteli, "Hyperdynamic plasticity of chromatin proteins in pluripotent embryonic stem cells," *Developmental Cell*, vol. 10, no. 1, pp. 105–116, 2006.

[42] Y. Cui, F. M. Hameed, B. Yang, K. Lee, C. Q. Pan, S. Park, and M. Sheetz, "Cyclic stretching of soft substrates induces spreading and growth," *Nature Communications*, vol. 6, p. 6333, 2015.

[43] K. H. Wong, J. M. Chan, R. D. Kamm, and J. Tien, "Microfluidic Models of Vascular Functions," *Annual Review of Biomedical Engineering*, vol. 14, no. 1, pp. 205–230, 2012.

[44] P. M. Davidson, H. Özçelik, V. Hasirci, G. Reiter, and K. Anselme, "Microstructured surfaces cause severe but non-detrimental deformation of the cell nucleus," *Advanced Materials*, vol. 21, no. 35, pp. 3586–3590, 2009.

[45] Z. Pan, C. Yan, R. Peng, Y. Zhao, Y. He, and J. Ding, "Control of cell nucleus shapes via micropillar patterns," *Biomaterials*, vol. 33, no. 6, pp. 1730–1735, 2012.

[46] M. Versaevel, T. Grevesse, and S. Gabriele, "Spatial coordination between cell and nuclear shape within micropatterned endothelial cells," *Nature Communications*, vol. 3, p. 671, 2012.

[47] Y. Fu, L. K. Chin, T. Bourouina, A. Q. Liu, and A. M. J. VanDongen, "Nuclear deformation during breast cancer cell transmigration," *Lab on a Chip*, vol. 12, no. 19, p. 3774, 2012.

[48] L. I. Friedman, "Shear Forces Upon Cultured," vol. 108, 1986.

[49] A. S. LaCroix, K. E. Rothenberg, and B. D. Hoffman, "Molecular-Scale Tools for Studying Mechanotransduction," *Annual Review of Biomedical Engineering*, vol. 17, no. 1, pp. 287–316, 2015.

[50] D.-H. Kim, P. K. Wong, J. Park, A. Levchenko, and Y. Sun, "Microengineered Platforms for Cell Mechanobiology," *Annual Review of Biomedical Engineering*, vol. 11, no. 1, pp. 203–233, 2009.

[51] T. Puntheeranurak, I. Neundlinger, R. K. H. Kinne, and P. Hinterdorfer, "Single-molecule recognition force spectroscopy of transmembrane transporters on living cells," *Nature Protocols*, vol. 6, no. 9, pp. 1443–1452, 2011.

[52] K. N. Dahl, A. J. Engler, J. D. Pajerowski, and D. E. Discher, "Power-Law Rheology of Isolated Nuclei with Deformation Mapping of Nuclear Substructures," *Biophysical Journal*, vol. 89, no. 4, pp. 2855–2864, 2005.

[53] A. Kumar, M. Mazzanti, M. Mistrik, M. Kosar, G. V. Beznoussenko, A. A. Mironov, M. Garrè, D. Parazzoli, G. V. Shivashankar, G. Scita, J. Bartek, and M. Foiani, "ATR mediates a checkpoint at the nuclear envelope in response to mechanical stress," *Cell*, vol. 158, no. 3, pp. 633–646, 2014.

[54] M. L. Rodriguez, P. J. McGarry, and N. J. Sniadecki, "Review on Cell Mechanics: Experimental and Modeling Approaches," *Applied Mechanics Reviews*, vol. 65, no. 6, p. 060801, 2013.

[55] Y.-C. Poh, S. P. Shevtsov, F. Chowdhury, D. C. Wu, S. Na, M. Dundr, and N. Wang, "Dynamic force-induced direct dissociation of protein complexes in a nuclear body in living cells," *Nature Communications*, vol. 3, no. May, p. 866, 2012.

[56] A. Ashkin, J. M. Dziedzic, and T. Yamane, "Optical trapping and manipulation of single cells using infrared laser beams," *Nature*, vol. 330, no. 6150, pp. 769–771, 1987.

[57] L. Trichet, J. Le Digabel, R. J. Hawkins, S. R. K. Vedula, M. Gupta, C. Ribrault, P. Hersen, R. Voituriez, and B. Ladoux, "Evidence of a large-scale mechanosensing mechanism for cellular adaptation to substrate stiffness," *Proceedings of the National Academy of Sciences*, vol. 109, no. 18, pp. 6933–6938, 2012.

[58] H. Zhang and K.-K. Liu, "Optical tweezers for single cells," *Journal of The Royal Society Interface*, vol. 5, no. 24, pp. 671–690, 2008.

[59] M. B. Rasmussen, L. B. Oddershede, and H. Siegumfeldt, "Optical tweezers cause physiological damage to Escherichia coli and Listeria bacteria," *Applied and Environmental Microbiology*, vol. 74, no. 8, pp. 2441–2446, 2008.

[60] L. Kremser, D. Blaas, and E. Kenndler, "Virus analysis using electromigration techniques," *Electrophoresis*, vol. 30, no. 1, pp. 133–140, 2009.

[61] M. P. Hughes, "Strategies for dielectrophoretic separation in laboratory-on-a-chip systems," *Electrophoresis*, vol. 23, no. 16, pp. 2569–2582, 2002.

[62] T. Wang, M. Ke, S. Xu, J. Feng, C. Qiu, and Z. Liu, "Dexterous acoustic trapping and patterning of particles assisted by phononic crystal plate," *Applied Physics Letters*, vol. 106, no. 16, pp. 1–5, 2015.

[63] J. Dobson, "Remote control of cellular behaviour with magnetic nanoparticles," *Nat. Nanotechnol.*, vol. 3, no. 3, pp. 139–143, 2008.

[64] A. H. de Vries, B. E. Krenn, R. van Driel, and J. S. Kanger, "Micro Magnetic Tweezers for Nanomanipulation Inside Live Cells," *Biophysical Journal*, vol. 88, no. 3, pp. 2137–2144, 2005.

[65] K. Gunnarsson, P. E. Roy, S. Felton, J. Pihl, P. Svedlindh, S. Berner, H. Lidbaum, and S. Oscarsson, "Programmable motion and separation of single magnetic particles on patterned magnetic surfaces," *Advanced Materials*, vol. 17, no. 14, pp. 1730–1734, 2005.

[66] M. Donolato, P. Vavassori, M. Gobbi, M. Deryabina, M. F. Hansen, V. Metlushko, B. Ilic, M. Cantoni, D. Petti, S. Brivio, and R. Bertacco, "On-chip manipulation of protein-coated magnetic beads via domain-wall conduits," *Advanced Materials*, vol. 22, no. 24, pp. 2706–2710, 2010.

[67] M. Donolato, A. Torti, N. Kostesha, M. Deryabina, E. Sogne, P. Vavassori, M. F. Hansen, and R. Bertacco, "Magnetic domain wall conduits for single cell applications," *Lab on a Chip*, vol. 11, no. 17, p. 2976, 2011.

[68] E. Rapoport and G. S. D. Beach, "Dynamics of superparamagnetic microbead transport along magnetic nanotracks by magnetic domain walls," *Applied Physics Letters*, vol. 100, no. 8, 2012.

[69] M. Donolato, P. Vavassori, M. Gobbi, M. Deryabina, M. F. Hansen, V. Metlushko, B. Ilic, M. Cantoni, D. Petti, S. Brivio, and R. Bertacco, "On-chip manipulation of protein-coated magnetic beads via domain-wall conduits," *Advanced Materials*, vol. 22, no. 24, pp. 2706–2710, 2010.

[70] Y. Li, G. Huang, B. Gao, M. Li, G. M. Genin, T. J. Lu, and F. Xu, "Magnetically actuated cell-laden microscale hydrogels for probing strain-induced cell responses in three dimensions," *NPG Asia Materials*, vol. 8, no. 1, p. e238, 2016.

[71] N. J. Sniadecki, A. Anguelouch, M. T. Yang, C. M. Lamb, Z. Liu, S. B. Kirschner, Y. Liu, D. H. Reich, and C. S. Chen, "Magnetic microposts as an approach to apply forces to living cells," *Proceedings of the National Academy of Sciences*, vol. 104, no. 37, pp. 14553–14558, 2007.

[72] J. le Digabel, N. Biais, J. Fresnais, J.-F. Berret, P. Hersen, and B. Ladoux, "Magnetic micropillars as a tool to govern substrate deformations," *Lab on a Chip*, vol. 11, no. 15, p. 2630, 2011.

[73] F. Khademolhosseini and M. Chiao, "Fabrication and patterning of magnetic polymer micropillar structures using a dry-nanoparticle embedding technique," *Journal of Microelectromechanical Systems*, vol. 22, no. 1, pp. 131–139, 2013.

[74] S. Blundell, *Magnetism in condensed matter*. Oxford University Press, 2001.

[75] A. Fox, "Magnetism and Magnetic Materials, by J.M.D. Coey," *Contemporary Physics*, vol. 52, pp. 83–84, jan 2011.

[76] L. Landau and E. Lifshits, "on the Theory of the Dispersion of Magnetic Permeability in Ferromagnetic Bodies," *Phys. Zeitsch. der Sow.*, vol. 169, no. 14, pp. 14–22, 1935.

[77] R. McMichael and M. Donahue, "Head to head domain wall structures in thin magnetic strips," *IEEE Transactions on Magnetics*, vol. 33, no. 5, pp. 4167–4169, 1997.

[78] N. L. Schryer and L. R. Walker, "The motion of domain walls in uniform dc magnetic fields," *Journal of Applied Physics*, vol. 45, no. 12, pp. 5406–5421, 1974.

[79] J. Y. Lee, K. S. Lee, S. Choi, K. Y. Guslienko, and S. K. Kim, "Dynamic transformations of the internal structure of a moving domain wall in magnetic nanostripes," *Physical Review B - Condensed Matter and Materials Physics*, vol. 76, no. 18, pp. 1–8, 2007.

[80] A. H. Lu, E. L. Salabas, and F. Schüth, "Magnetic nanoparticles: Synthesis, protection, functionalization, and application," *Angewandte Chemie - International Edition*, vol. 46, no. 8, pp. 1222–1244, 2007.

[81] T. Lund-olesen, "On-Chip Biological Analysis using Magnetic Beads," 2008.

[82] M. A. M. Gijs, "Magnetic bead handling on-chip: new opportunities for analytical applications," *Microfluidics and Nanofluidics*, vol. 1, pp. 22–40, oct 2004.

[83] A. G. Roca, R. Costo, A. F. Rebolledo, S. Veintemillas-Verdaguer, P. Tartaj, T. González-Carreño, M. P. Morales, and C. J. Serna, "Progress in the preparation of magnetic nanoparticles for applications in biomedicine," *Journal of Physics D: Applied Physics*, vol. 42, no. 22, p. 224002, 2009.

[84] L. D. Landau, E. M. Lifshitz, and A. L. King, "Electrodynamics of Continuous Media," 1961.

[85] L. D. Landau and E. M. Lifshitz, *Theory of Elasticity*. Pergamon Press, 1959.

[86] J. Lipfert, X. Hao, and N. H. Dekker, "Quantitative modeling and optimization of magnetic tweezers," *Biophysical Journal*, vol. 96, no. 12, pp. 5040–5049, 2009.

[87] Q. Cao, X. Han, and L. Li, "Configurations and control of magnetic fields for manipulating magnetic particles in microfluidic applications: magnet systems and manipulation mechanisms," *Lab on a Chip*, vol. 14, no. 15, p. 2762, 2014.

[88] R. Bertacco, M. Donolato, M. Gobbi, M. Cantoni, S. Brivio, D. Petti, and P. Vavassori, "PCT/EP2010/000879, nanoGune Consolider.," 2009.

[89] A. Torti, V. Mondiali, A. Cattoni, M. Donolato, E. Albisetti, A. M. Haghiri-Gosnet, P. Vavassori, and R. Bertacco, "Single particle demultiplexer based on domain wall conduits," *Applied Physics Letters*, vol. 101, no. 14, 2012.

[90] P. Nelson, "Biological Physics : Energy , Information , Life," 2002.

[91] H. NoTitBruus, *Theoretical Microfluidics*. 2007.

[92] P. Holmqvist, J. K. G. Dhont, and P. R. Lang, "Colloidal dynamics near a wall studied by evanescent wave light scattering: Experimental and theoretical improvements and methodological limitations," *Journal of Chemical Physics*, vol. 126, no. 4, 2007.

[93] A. Einstein, "Über die von der molekularkinetischen Theorie der Wärme geforderte Bewegung von in ruhenden Flüssigkeiten suspendierten Teilchen," *Annalen der Physik*, vol. 322, no. 8, pp. 549–560., 1915.

[94] U. Uthor, S. Bates, P. Thamban, J. Matthew, L. Overzet, and P. . Box, "Silicon Etch Using SF6 / C4F8 / Ar Gas Mixtures," pp. 0–11, 2014.

[95] D. B. Lee, "Anisotropic Etching of Silicon Anisotropic Etching of Silicon," vol. 4569, 1969.

[96] F. Marty, L. Rousseau, B. Saadany, B. Mercier, and O. Franc, "Advanced etching of silicon based on deep reactive ion etching for silicon high aspect ratio microstructures and three-dimensional micro- and nanostructures," vol. 36, pp. 673–677, 2005.

[97] W. P. Wolf, "Versatile and Sensitive Vibrating-Sample Magnetometer*," vol. 30, no. 7, pp. 548–557, 1959.

[98] T. Deng, M. Prentiss, and G. M. Whitesides, "Fabrication of magnetic microfiltration systems using soft lithography," *Applied Physics Letters*, vol. 80, no. 3, pp. 461–463, 2002.

[99] H. Ebrahimian, M. Giesguth, K. Dietz, G. Reiss, and S. Herth, "Magnetic tweezers for manipulation of magnetic particles in single cells," vol. 063701, pp. 1–6, 2014.

[100] B. B. Yellen and G. Friedman, "Programmable assembly of heterogeneous colloidal particle arrays," *Advanced Materials*, vol. 16, no. 2, pp. 111–115, 2004.

[101] M. Monticelli, D. V. Conca, E. Albisetti, A. Torti, P. P. Sharma, G. Kidiyoor, S. Barozzi, D. Parazzoli, P. Ciarletta, M. Lupi, D. Petti, and R. Bertacco, "Magnetic domain wall tweezers: a new tool for mechanobiology studies on individual target cells," *Lab Chip*, vol. 16, no. 15, pp. 2882–2890, 2016.

[102] M. Monticelli, E. Albisetti, D. Petti, D. V. Conca, M. Falcone, P. P. Sharma, and R. Bertacco, "Towards an on-chip platform for the controlled application of forces via magnetic particles: A novel device for mechanobiology," *Journal of Applied Physics*, vol. 117, no. 17, pp. 8–12, 2015.

[103] M. A. M. Gijs and U. Lehmann, "Microfluidic Applications of Magnetic Particles for Biological Analysis and Catalysis," pp. 1518–1563, 2010.

[104] V. A. Spencer, R. Xu, and M. J. Bissell, "NIH Public Access," *Journal of Mammary Gland Biology and Neoplasia*, pp. 1–11, 2011.

[105] D. Wirtz, "Particle-Tracking Microrheology of Living Cells: Principles and Applications," *Annual Review of Biophysics*, vol. 38, no. 1, pp. 301–326, 2009.

[106] C. Gosse and V. Croquette, "Magnetic Tweezers: Micromanipulation and Force Measurement at the Molecular Level," *Biophysical Journal*, vol. 82, no. 6, pp. 3314–3329, 2002.

[107] H. Markides, M. Rotherham, and A. J. E. Haj, "Biocompatibility and Toxicity of Magnetic Nanoparticles in Regenerative Medicine," vol. 2012, pp. 13–15, 2012.

[108] F. M. Hameed, M. Rao, and G. V. Shivashankar, "Dynamics of Passive and Active Particles in the Cell Nucleus," *PLoS ONE*, vol. 7, no. 10, pp. 1–11, 2012.

[109] Y. Zheng, J. Nguyen, Y. Wei, and Y. Sun, "Recent advances in microfluidic techniques for single-cell biophysical characterization," *Lab on a Chip*, vol. 13, no. 13, p. 2464, 2013.

[110] C. P. Gooneratne, R. Kodzius, F. Li, I. G. Foulds, and J. Kosel, "On-chip magnetic bead manipulation and detection using a magnetoresistive sensor-based micro-chip: Design considerations and experimental characterization," *Sensors (Switzerland)*, vol. 16, no. 9, 2016.

[111] H. Ebrahimian, M. Giesguth, K.-J. Dietz, G. Reiss, and S. Herth, "Magnetic tweezers for manipulation of magnetic particles in single cells," *Applied Physics Letters*, vol. 104, no. 6, p. 063701, 2014.

[112] R. S. Conroy, G. Zabow, J. Moreland, A. P. Koretsky, R. S. Conroy, G. Zabow, J. Moreland, and A. P. Koretsky, "Controlled transport of magnetic particles using soft magnetic patterns," vol. 203901, no. 2008, pp. 6–9, 2014.

[113] M. Monticelli, A. Torti, M. Cantoni, D. Petti, E. Albisetti, A. Manzin, E. Guerriero, R. Sordan, G. Gervasoni, M. Carminati, G. Ferrari, M. Sampietro, and R. Bertacco, "On-Chip Magnetic Platform for Single-Particle Manipulation with Integrated Electrical Feedback," *Small*, vol. 12, no. 7, pp. 921–929, 2016.

[114] A. Sarella, A. Torti, M. Donolato, M. Pancaldi, and P. Vavassori, "Two-Dimensional Programmable Manipulation of Magnetic Nanoparticles on-Chip," pp. 2384–2390, 2014.

[115] D. Donahue, "1999 OOMMF User's Guide, Version 1.0. Interagency Report NISTIR," vol. 6376, p. 3, 2004.

[116] J. T. Padding and W. J. Briels, "Translational and rotational friction on a colloidal rod near a wall," no. January, pp. 1–9, 2010.

[117] J. Riedl, A. H. Crevenna, K. Kessenbrock, J. H. Yu, D. Neukirchen, M. Bista, F. Bradke, D. Jenne, T. A. Holak, Z. Werb, M. Sixt, and R. Wedlich-Soldner, "Lifeact: a versatile marker to visualize F-actin," *Nature Methods*, vol. 5, no. 7, pp. 605–607, 2008.

[118] Y. Zhang, M. Yang, and N. G. Portney, "Zeta potential: a surface electrical characteristic to probe the interaction of nanoparticles with normal and cancer human breast epithelial cells," pp. 321–328, 2008.

[119] A. Vaziri and L. Mahadevan, "Localized and extended deformations of elastic shells," *Proceedings of the National Academy of Sciences*, vol. 105, no. 23, pp. 7913–7918, 2008.

[120] K. S. Kim, C. H. Cho, E. K. Park, M. H. Jung, K. S. Yoon, and H. K. Park, "AFM-Detected apoptotic changes in morphology and biophysical property caused by paclitaxel in Ishikawa and HeLa cells," *PLoS ONE*, vol. 7, no. 1, 2012.

[121] T. Jadidi, H. Seyyed-Allaei, M. R. R. Tabar, and A. Mashaghi, "Poisson Ratio and Youngs Modulus of Lipid Bilayers in Different Phases," *Frontiers in Bioengineering and Biotechnology*, vol. 2, no. April, pp. 1–6, 2014.

[122] D. Vella, A. Ajdari, A. Vaziri, and A. Boudaoud, "Indentation of ellipsoidal and cylindrical elastic shells," *Physical Review Letters*, vol. 109, no. 14, pp. 1–5, 2012.

[123] E. Ventsel and T. Krauthammer, *Thin plates and shells: theory, analysis, and applications*. Marcel Dekker, 2001.

[124] A. V. Pogorelov, *Bendings of surfaces and stability of shells*. Providence R.I.: American Mathematical Society, 1988.

[125] A. Celedon, C. M. Hale, and D. Wirtz, "Magnetic manipulation of nanorods in the nucleus of living cells," *Biophysical Journal*, vol. 101, no. 8, pp. 1880–1886, 2011.

[126] R. L. Juliano and S. Haskill, "Signal transduction from the extracellular matrix," *The Journal of cell biology*, vol. 120, no. 3, pp. 577–585, 1993.

[127] M. Ghibaudo, A. Saez, L. Trichet, A. Xayaphoummine, J. Browaeys, P. Silberzan, A. Buguin, and B. Ladoux, "Traction forces and rigidity sensing regulate cell functions," *Soft Matter*, vol. 4, no. 9, p. 1836, 2008.

[128] M. M. Mukaka, "Statistics corner: A guide to appropriate use of correlation coefficient in medical research," *Malawi Medical Journal*, vol. 24, no. 3, pp. 69–71, 2012.

[129] M. Sun, J. S. Graham, B. Hegedüs, F. Marga, Y. Zhang, G. Forgacs, and M. Grandbois, "Multiple Membrane Tethers Probed by Atomic Force Microscopy," *Biophysical Journal*, vol. 89, no. 6, pp. 4320–4329, 2005.